Leveraging Operando Characterization Methods to Reveal Failure and Optimization Mechanisms of Group IV Semiconductor Battery Anodes

Jarred Olson

A dissertation

submitted in partial fulfillment of the

requirements for the degree of

Doctor of Philosophy

University of Washington

2019

Reading Committee:

Cody Schlenker, Chair

Bo Zhang

Vincent Holmberg

Program Authorized to Offer Degree:

Chemistry

University of Washington

Abstract

Leveraging Operando Characterization Methods to Reveal Failure and Optimization Mechanisms of Group IV Semiconductor Battery Anodes

Jarred Olson

Chair of the Supervisory Committee:
Professor Cody Schlenker
Department of Chemistry

Expanding the application space of lithium battery technology will require electrode materials that exhibit performance metrics which outperform their modern counterparts. The availability of prospective next-generation electrode materials to meet this demand is promising, as the group IV semiconductors Si and Ge exhibit an order of magnitude higher capacity for lithium storage than traditional electrode materials. However, there exist several issues related to the compatibility between these candidate electrode materials and components that presently make up a battery, problems that can be mitigated by the impractical use of expensive and toxic fluorinated compounds. This thesis focuses on the molecular nature of stability and instability mechanisms between group IV semiconductor composite electrodes and their surrounding solid and liquid matrices, with specific attention on the electrode interface. First, we distinguish cycling behavior of Si anodes by the interfacial chemistries that develop as a function of the Si lithiation state and fluorine content using vibrational spectroscopy. Next, we probe the cycling

performance of germanium nanowire anodes in the solid-state and learn that electrochemical accessibility to crystalline $Li_{15}Ge_4$ and amorphous Li_xGe_y phases determine their cycle life. We further observe that surface functionalization of Ge nanowires eliminates the need for fluorinated compounds in the battery, highlighting a strategy to circumvent the barriers described earlier. Because the dynamics of electrochemical phenomena are strongly affected by the high local fields at the electrode interface, we end with a novel quantitative analysis of the electric fields present at the electrode/electrolyte junction with the use of a systematic calibration of electrolyte solvents to electric fields. We expect these results to lend guidelines that better inform the design rules for batteries utilizing next-generation, high capacity active materials.

Acknowledgements

This thesis would not be possible without the mentorship of Cody Schlenker, support from the University of Washington department of Chemistry and the Clean Energy Institute. Also, thank you to my committee members Bo Zhang, Vince Holmberg and Guozhong Cao. During the final phase of my PhD I felt very fortunate knowing how much you all wanted me to succeed in my career goals; thanks for making the transition out of graduate school a smooth one.

Along with Cody and my committee members, there are others to whom I owe a lot of gratitude. Thank you to Patrik Johansson, who spent countless hours with me discussing science and philosophy. Thank you also to Samuel Schneider and Elena Pandres, two excellent collaborators who taught me a tremendous amount about electrostatics and differential capacity. I'm happy we all got along so well.

I also want to thank my friends from graduate school for exploring the city with me, going to concerts and comedy shows, hiking, hosting cookouts, watching/playing sports and experiencing life in general. Thanks also to the people I would see in the department for the smiles and talks whenever we had time.

Finally, a loving thanks to my family and friends outside of Seattle: Mom & Dad, Adam, Sandy and Mark- you all are such a stabilizing force in my life and I'm happy to see the family growing so beautifully. John, Josh, Anthony and Chris- you have no idea how grateful I am that our friendships have only strengthened with time and distance, something I didn't know would be possible considering how close we were as kids living near each other. Whether it's seeing any of you in person or talking on the phone, I realize through this experience that whatever happens, you all have consistently supported me throughout these years. No matter how much time passes, we never skip a beat; thanks so much for the positivity you send my way.

Dedication

To Seattle, a city that served as a wonderful setting for the intensely rewarding personal and intellectual experiences over these last five years. Thank you for juxtaposing so much nature, art, music and culture with my scientific endeavors; what an experience to remember!

Table of Contents

List of Tables

List of Figures

Chapter 1: Introduction

1.1 Motivation and Context

The concept of converting potential energy to electricity can be made possible through a variety of mechanisms: hydroelectricity, compressed air and flywheels are a few examples that provide energy on demand, but exhibit drawbacks in terms of geographical constraints, poor precision control and size restrictions.[1-4] Alternatively, storing energy in the form of chemical bonds is attractive due to the portability of liquid fuels, capacitors and batteries. Combustion of liquid fuels results in the release of greenhouse gases,[5] while capacitors are limited in their storage of charge by the surface area of electrodes. In comparison, batteries offer a zero-emission energy source whose charge storage mechanism manifests from surface *and* bulk contributions.

Among different battery chemistries, lithium benefits from a low ionization energy and light atomic weight, enabling the largest amount of available energy (519 kJ/mol)[6] when compared to other alkali-metals. Additionally, lithium ion (Li-ion) batteries are more economically competitive than other battery formats (nickel-cadmium, lead-acid) for the reason they provide the highest energy stored on investment.[7]

Briefly described, a battery contains two electrodes: an anode and cathode. Because this thesis focuses on anodes, we will highlight the comparison of next-generation anode materials against graphite, as it is the archetypal active material in use as an anode in modern batteries. The solid matrix of an electrode contained within a battery, herein referred to as a composite electrode, is composed of a homogeneous combination of an active material (the material that electrochemically stores Li^+) with electrically-conductive additive and polymeric binder, all of which are attached to a current collector. The liquid matrix, herein referred to as the electrolyte, shuttles Li^+ between electrodes within the battery. Since the first Li-ion batteries were demonstrated in the 1970's,[8-9] advances in the scientific understanding of the synergy between the active material and its surrounding composite and electrolyte matrices[10-16] culminated in their market availability in the 1990's by Sony corporation.[17] Additional feats in the purification of active materials and enhanced fabrication processes of composite electrodes[18-20] have further expanded the technological applications of Li-ion batteries, most recently highlighted by their adoption within the automotive industry.[21-23]

While future applications of Li-ion batteries are projected to include residential microgrids[24-25] and aerospace applications,[26] modern electrode materials are incapable of supporting such high energy applications.[27-28] Advances described in the previous paragraph have been on active materials that are the same basic chemical composition as they were decades ago,[29-30] which are now operating at their limits of

available energy and power. Therefore, continuing the expansion of Li-ion battery technology into new industries requires modern active materials be replaced with next-generation, high energy counterparts.

The electrochemical storage of Li with group IV semiconductor anodes (Si and Ge) was first demonstrated as a proof of concept near the beginning of the 21st century.[31-32] Perhaps the biggest difference between these active materials and conventional graphite anodes is the mechanism of Li storage through a process that involves alloying, rather than intercalation in the case of graphite.[33] As the interatomic distance between adjacent Si/Ge atoms is too small to accommodate Li within their crystalline lattice, the solid-state characteristics of these active materials undergo substantial changes before and after a lithiation cycle; individual Si/Ge atoms coordinate approximately 4 Li atoms per unit cell,[34-36] resulting in a volume expansion of ~300% and an irreversible conversion of their crystalline phase to an amorphous phase.[37] In bulk Si/Ge active materials, this volume expansion occurs a biaxial direction, generating a strain energy at the boundary between the lithiated and non-lithiated solid phases that fractures it to an extent the local bonding network is lost.[38-41] Scientific breakthroughs on the study of nano/micro-structured Si and Ge revealed the critical dimensions at which the abovementioned material fracture does not occur (diameters of <150 nm for Si and ~1.2 μm for Ge),[42-46] due to volume expansion in a circumferential direction to mitigate mechanical fracture and strain energy. Furthermore, it has been observed that different nanostructured geometries can produce different lithiation and de-lithiation rates.[47-50]

Despite enabling greater retention of Li redox activity within Si/Ge active materials by their confinement to the nanoscale, there exist several barriers to their practical use in working batteries that mirror previous difficulties experienced in the development of graphite anodes. Integrating Si/Ge active materials into a composite electrode format using materials and methods adopted for graphite has been largely unsuccessful due to incompatibilities between the binder component and active material,[51-54] while electrolytes that enabled robust cycling performance for graphite anodes do not impart stable cycling behavior to group IV nanostructured counterparts.[55-57] Improvements to the cycling performance of Si/Ge active materials have been most frequently achieved using fluorinated electrolyte additives,[58-68] but concerns with the high expense of fluorinated compounds[69-70] and their potential toxicity[71] make them impractical solutions to produce cost-effective and safe batteries.

1.2 Scope and objective

The scope of this thesis is to bring into focus the analysis of battery electrode interfaces and the effect of chemically functionalizing them, with the objective to link such findings to bulk operability of Si and Ge-containing electrodes in devices. Interface science provides a powerful probe to study electrochemical

phenomena. Recent advances to analytical instrumentation and computational capabilities have resolved concentration profiles of electrolyte solvents at the electrode/electrolyte junction to deviate from their bulk ratios,[72-74] electrolyte energy levels renormalize on an electrode surface,[75-77] and high interfacial electric fields on the order of MV/cm appear to be present.[78-79] In the context of group IV semiconductor battery materials, if the material interface can be studied and tailored to better understand operating mechanisms of next-generation batteries at a molecular level, then such findings can be used to better guide the development of next-generation battery materials.

We use the remaining sections of chapter 1 to outline the operating physics of batteries, as well as the electrochemical methods used to interpret their performance. Chapter 2 describes vibrational spectroscopy and highlights the interface-selectivity of measurements used throughout chapter 3, where we leverage vibrational spectroscopy to investigate the chemical dynamics of fluorinated and non-fluorinated electrolyte solvents at the surface of nano-Si active material. Based on our results, we distinguish the stability and instability mechanism between each electrolyte solvent at nano-Si interfaces in chapter 3 and demonstrate their chemistries at the surface of nano-Si are significantly different at specific degrees of Si lithiation. Furthermore, we discover the existence of new compounds on the electrode surface after the first electrochemical cycle. Results from this study are the first to validate specific theoretical descriptions of electrolyte instability on electrode surfaces.

In chapter 4, we extend the scientific trajectory from the electrode interface into the lattice of *interface-functionalized* Ge nanowire (NW) composite electrodes, highlighting the degree to which solid-state behavior of lithiation and de-lithiation processes are affected by the electrolyte composition. We showed for the first time that the cycle life of Ge NW composites can be improved without the need for fluorinated electrolyte components with alkane passivation included as part of the active material synthesis. Furthermore, our results demonstrate a dependence of battery cycle life on the processing technique of the electrode composite, an important consideration as industries become involved with mass-production of electrode composites containing these materials.

As the processes described in the above two projects rely upon the application of macroscopic potentials to cycle the battery, this dissertation ends with a systematic calibration of electrolyte solvents to electric fields in chapter 5; further background related to this project is included in section 2.4. Using results from the calibration dataset, we produce a novel model to calculate fields at archetypal electrode/electrolyte junctions.

1.3: Operating principles and mechanisms in batteries

Batteries contain two electrodes, a cathode and anode, each of which contain different active materials as part of their composite electrodes and are marked with a positive and negative terminal. The total energy of a battery is partly a manifestation of the difference between the chemical potential of Li in the cathode (positive terminal) and anode (negative terminal),[80-82] providing a *spontaneous* driving force to power an external load when a battery is in its fully charged, ready-to-use state. Figure 1 formalizes these processes visually, where the spontaneity of this driving force (and thus, extractable energy) can be registered with a voltmeter connected to the two terminals of a battery, a concept formally quantified by:

$$\Delta G^{o} = \frac{\mu_c - \mu_a}{-nF} = \Delta V_{cell} \qquad (1.1)$$

Where (ΔG^{o}) is the Gibbs free energy, n the number of electrons involved in the reaction $Li^{+} + e^{-} \rightarrow Li$ (n=1), F is Faradays constant (96485 $\frac{coulombs}{mol\ electrons}$), V_{cell} is the cell voltage and $\mu_{c/a}$ represent the chemical potential of Li in the cathode and anode, respectively.

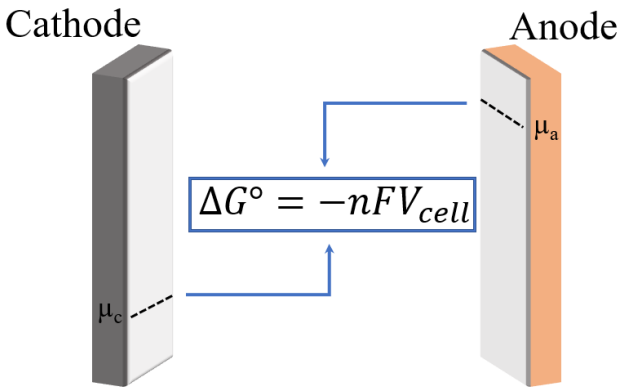

Figure 1: Macroscopic representation of the spontaneous driving force for a charged battery and its relationship to the cell voltage, signified by the difference in chemical potentials of Li in the solid phases of each electrode.

Electrochemically, redox activity of Li^{+} between each electrode occurs in equal and opposite reactions to maintain charge balance as the battery operates. While electrolytically charging a battery to its highest state of energy for later use (corresponding to a large potential difference), the lithiation reaction $Li^{+} \rightarrow Li$ occurs at the anode and the opposite reaction (de-lithiation, $Li \rightarrow Li^{+}$) occurs at the cathode; Figure 1 represents the result of a de-lithiated cathode and a lithiated anode after electrolytic charging. While the battery powers a device, the cathode is lithiated and anode de-lithiated spontaneously due to the difference in potential between both electrodes. Oftentimes, this process is referred to as discharging the battery. Both charging and discharging processes are only possible when both electrodes are in contact with an electrolyte, an ion-conducting matrix comprised of a lithium-containing salt and medium that solvates lithium ions during charging and discharging of the battery. As the battery powers an external

load, $\mu_{c/a}$ changes as a function of the lithium concentration in the solid phases of both the cathode and anode active materials:

$$\mu_{c/a} = E_0 - kT \cdot ln\left[\frac{x}{1-x}\right] \qquad (1.2)$$

Where E_0 is the standard potential of the Li/Li^+ redox couple, k is the Boltzmann constant, T is the temperature and x the ratio of active sites populated with lithium to the available sites to populate with lithium.[83] Therefore, changing this ratio by electrolytic charging or spontaneous discharging of the battery will change the voltage of the cell and affect the amount of energy that can be delivered to an electrical load by the following expression:

$$\Delta V_{cell} = \frac{\Delta G}{\Delta[Li]} \qquad (1.3)$$

The concentration of Li within the solid phase of an active material is the other determinant of the total energy contained within a battery, and represents the amount of charge that can be extracted from the lithiated electrode. Referencing a unit cell containing the maximum amount of Li atoms coordinated to the active material produces an accurate estimate of its gravimetric energy (in units of mAh/g). For example, the theoretical capacity of graphite is calculated based on the LiC_6 phase,[84] when graphite is at its most highly lithiated state:

$$\left(\frac{1\ mol\ Li}{6\ mol\ C}\right)\left(\frac{6\ mol\ C}{72g}\right)\left(\frac{96485\ Coulombs}{mol\ e-}\right)\left(\frac{1mol\ e-}{mol\ Li}\right)\left(\frac{Ampere \cdot second}{Coulomb}\right)\left(\frac{1\ hour}{3600\ seconds}\right)\left(\frac{1000\ milliAmperes}{Ampere}\right) = \frac{372\ mAh}{g} \qquad (1.4)$$

Formation of the LiC_6 phase follows different stages that are dominated by enthalpic and entropic components embedded in the expression of ΔG:

$$\Delta G = \Delta H - T\Delta S \qquad (1.5)$$

Where the enthalpic component ΔH expresses the site energy within the active material lattice for inserting Li^+,[85-86] expressed in units of eV/atom (equivalent to 100 kJ/mol); ΔS represents the entropy of mixing within the active material lattice.[87] Continuing with the example of graphite, the pathway involved in the lithiation of carbon to the LiC_6 phase will begin with the formation of phases associated with lower site energies (and thus, different potentials) where lithium can be inserted or extracted. For instance, the LiC_{12} phase requires less electrical potential energy to form than the LiC_6 phase.[88] This information is important to consider because it demonstrates that the number of charges stored in an active material (and thus, the concentration of Li in its lattice) is voltage-dependent. Due to the previously mentioned amorphization of the Si/Ge crystalline network, identifying the different stages and phases of lithiation/de-lithiation in the group IV semiconducting active material series remains a complex

endeavor.[89-90] However, it is agreed upon that the highest state of lithiation for both active materials are likely to be the crystalline $Li_{15}Si_4$ and $Li_{15}Ge_4$ phases that form at approximately 10 mV (vs. Li/Li^+).[91-97] Nevertheless, identifying the intermediate stages is a useful and active area of research for guiding the geometric optimization of nanostructures.[98-103]

Equipped with an understanding that the voltage and number of vacancy sites within the active material lattice determine the energy of the battery, a final solution for expressing the total energy of a battery is formalized:

$$E = P \bullet t \quad (1.5)$$

Where E is energy (units of Joules), P is power (units of Watts, embedding the voltage and amount of charge stored by the active material) and t is time (units of hours).

Similar to the above principles describing the energetics of active materials in the solid-state, corollaries can be drawn to energetics at the electrode/electrolyte junction. From thermodynamic considerations, electrolyte stability is implicated in the expression of free energy and the high local electric fields at the electrode interface.[104-105] Additionally, the energetics of Li^+ transfer at the electrode/electrolyte junction and the coordination environment of Li by its solvating medium is expressed in enthalpic terms.[106-109]

1.4: Battery Cycling and Data Analysis

When a battery is operating, electrons are transferred between the cathode and anode at a constant current (referred to as galvanostatic mode, blue trace of Figure 2), and current is used to satisfy the electrical load requirements imposed by the application. The current load is determined based on the known amounts of active material in the composite electrode. For example, the full theoretical capacity of a composite electrode containing 1.3 micrograms of graphite active material could be utilized in five hours under a constant current expressed below:

$$\left(\frac{372\ mAh}{g}\right)\left(\frac{1\ cycle}{5\ hours}\right)\left(\frac{0.0013\ g\ active\ material}{battery}\right) = 500\ \mu A \quad (1.6)$$

Consequently, the voltage of the electrode will change in response to maintain the desired current (black trace of Figure 2) by using the available work as described by Eq. 1.1 The voltage profile over time indicates whether the active material is undergoing lithiation or de-lithiation; lithiation of the material occurs as the voltage moves toward potentials close to 0 V vs. Li/Li^+ (corresponding to LiC_6 from cycling data displayed in Figure 2) while de-lithiation occurs when the voltage moves away from 0 V vs. Li/Li^+. When the voltage plateaus over a given period of time (between hours 3-5, for example), the site energy for a lithiation/de-lithiation event is achieved and the voltage remains constant until all sites are

populated/de-populated. In the case where an active material experiences a current load that is expected to deplete its theoretical energy in an hour, the expression to use is the charge rate (c-rate). For example, in Figure 2 (black trace), the graphite anode is fully lithiated in 5 hours and fully de-lithiated in 5 hours for its first cycle as previously calculated in Eq. 1.6. In its second cycle, the time increases to 10 hours each for the lithiation and de-lithiation processes to occur; Figure 2 (blue trace) shows how the galvanostatic current changes to adjust for the different c-rates (C/5 and C/10, respectively).

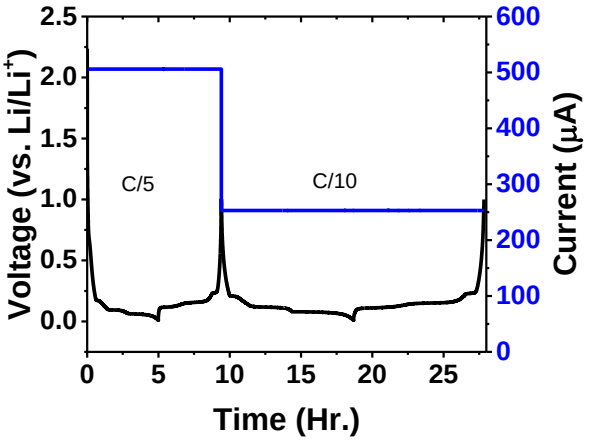

Figure 2: Galvanostatic cycling of a graphite anode at a c-rate of C/5 and C/10. The denominator of each c-rate expresses the time required to fully lithiate or de-lithiate the active material.

Because the responding variables of a battery cycling in galvanostatic mode are voltage, time and charge, several methods of data analysis are possible. Frequently, the total charge per cycle is divided by the mass of active material within the composite to extract specific capacity (mAh/g); it's value and retention over each cycle often serve as a robust descriptor for the success an electrode/electrolyte system can have in the long term. Both capacity and capacity retention are plotted below in Figure 3.

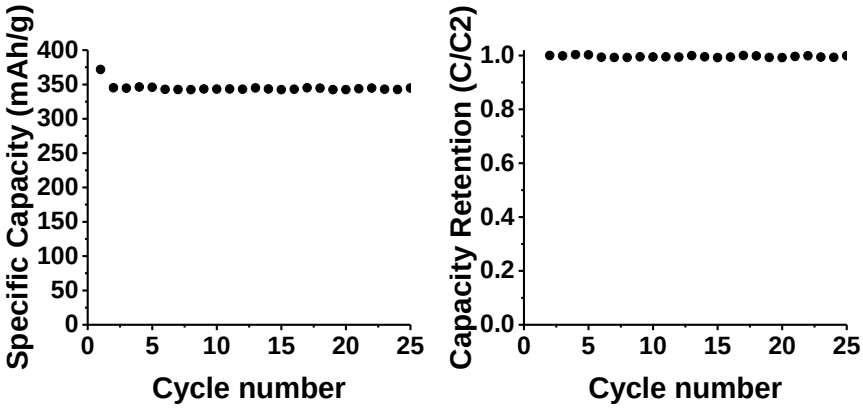

Figure 3: Gravimetric (specific) lithiation capacity of a graphite anode and capacity retention (lithiation capacity normalized to the second cycle, C/C2) for 25 cycles.

At a mechanistic level, the change in voltage as a function of time and/or current as displayed in Fig. 2 is often translated to a plot known as a differential capacity (dQ/dV) plot,[110-112] where the first derivative of charge per unit voltage (dQ/dV) is plotted against the operating voltage window. This analytical method relates points in a typical voltage profile with the accessibility of solid-state phases within the active material that can electrochemically store lithium. As an example, Figure 4a reveals the points where derivatives are taken to create the differential capacity plot in Figure 4b for the graphite anode presented in this section. In graphite, these points are related to the activation of different phases (i.e. LiC_{12}, LiC_6),[84, 113] and the areas within each peak correspond to the amount of charge that contributes to the overall capacity of the lithiation and delithiation processes.

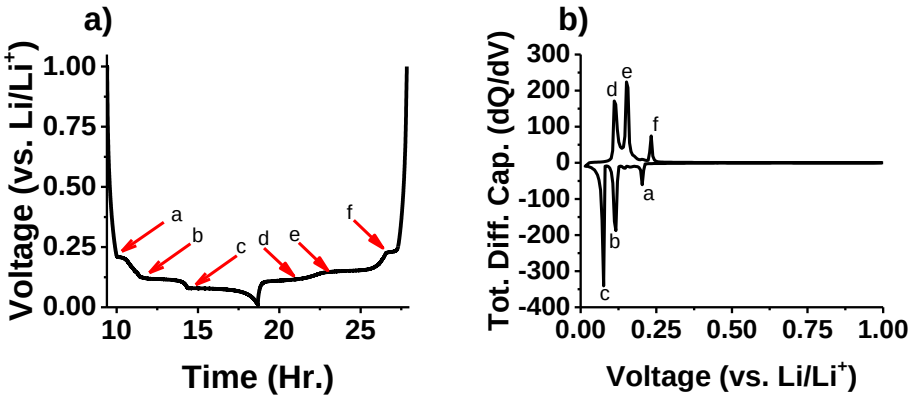

Figure 4: a) Polarization of a graphite anode towards 0 V vs. Li/Li^+, promoting the lithiation of graphite along points a-c; points d-f indicate de-lithiation. Each point precedes a plateau indicating the applied voltage matches the lattice site energy required for lithiation/de-lithiation. The amount of charge contained within solid phases are recognized with Figure 4b.

1.5 References:

1. Peña-Alzola, R.; Sebastián, R.; Quesada, J.; Colmenar, A. In *Review of flywheel based energy storage systems*, 2011 International Conference on Power Engineering, Energy and Electrical Drives, 11-13 May 2011; 2011; pp 1-6.
2. Kim, Y.-M.; Lee, J.-H.; Kim, S.-J.; Favrat, D., Potential and Evolution of Compressed Air Energy Storage: Energy and Exergy Analyses. *Entropy* **2012,** *14* (8).
3. Yang, C.-J.; Jackson, R. B., Opportunities and barriers to pumped-hydro energy storage in the United States. *Renewable Sustainable Energy Rev.* **2011,** *15* (1), 839-844.
4. Rehman, S.; Al-Hadhrami, L. M.; Alam, M. M., Pumped hydro energy storage system: A technological review. *Renewable Sustainable Energy Rev.* **2015,** *44*, 586-598.
5. Agency, U. S. E. P. Sources of Greenhouse Gas Emissions. https://www.epa.gov/ghgemissions/sources-greenhouse-gas-emissions.
6. Rumble, J. R., Ionization Energies of Atoms and Atomic Ions. CRC Press/Taylor & Francis: CRC Handbook of Chemistry and Physics, 99th edition, 2018.
7. Barnhart, C. J.; Benson, S. M., On the importance of reducing the energetic and material demands of electrical energy storage. *Energy Environ. Sci.* **2013,** *6* (4), 1083-1092.

8. Whittingham, M. S., Electrical Energy Storage and Intercalation Chemistry. *Science* **1976,** *192* (4244), 1126.
9. Besenhard, J. O.; Fritz, H. P., Cathodic reduction of graphite in organic solutions of alkali and NR_4^+ salts. *Journal of Electroanalytical Chemistry and Interfacial Electrochemistry* **1974,** *53* (2), 329-333.
10. Aurbach, D.; Gofer, Y.; Ben-Zion, M.; Aped, P., The behaviour of lithium electrodes in propylene and ethylene carbonate: Te major factors that influence Li cycling efficiency. *J. Electroanal. Chem.* **1992,** *339* (1), 451-471.
11. Dahn, J. R.; Zheng, T.; Liu, Y.; Xue, J. S., Mechanisms for Lithium Insertion in Carbonaceous Materials. *Science* **1995,** *270* (5236), 590.
12. Richard, M. N.; Dahn, J. R., Accelerating rate calorimetry studies of the effect of binder type on the thermal stability of a lithiated mesocarbon microbead material in electrolyte. *J. Power Sources* **1999,** *83* (1), 71-74.
13. Fong, R.; von Sacken, U.; Dahn, J. R., Studies of Lithium Intercalation into Carbons Using Nonaqueous Electrochemical Cells. *J. Electrochem. Soc.* **1990,** *137* (7), 2009-2013.
14. Aurbach, D.; Levi, M. D.; Levi, E.; Schechter, A., Failure and Stabilization Mechanisms of Graphite Electrodes. *The J. Phys. Chem. B* **1997,** *101* (12), 2195-2206.
15. Zheng, H.; Yang, R.; Liu, G.; Song, X.; Battaglia, V. S., Cooperation between Active Material, Polymeric Binder and Conductive Carbon Additive in Lithium Ion Battery Cathode. *The J. Phys. Chem. C* **2012,** *116* (7), 4875-4882.
16. Chusid, O.; Ein Ely, E.; Aurbach, D.; Babai, M.; Carmeli, Y., Electrochemical and spectroscopic studies of carbon electrodes in lithium battery electrolyte systems. *J. Power Sources* **1993,** *43* (1), 47-64.
17. Ozawa, K., Lithium-ion rechargeable batteries with $LiCoO_2$ and carbon electrodes: the $LiCoO_2$/C system. *Solid State Ionics* **1994,** *69* (3), 212-221.
18. Shim, J.; Striebel, K. A., Effect of electrode density on cycle performance and irreversible capacity loss for natural graphite anode in lithium-ion batteries. *J. Power Sources* **2003,** *119-121*, 934-937.
19. Peled, E.; Golodnitsky, D.; Ulus, A.; Yufit, V., Effect of carbon substrate on SEI composition and morphology. *Electrochim. Acta* **2004,** *50* (2–3), 391-395.
20. Mao, C.; Wood, M.; David, L.; An, S. J.; Sheng, Y.; Du, Z.; Meyer, H. M.; Ruther, R. E.; Wood, D. L., Selecting the Best Graphite for Long-Life, High-Energy Li-Ion Batteries. *J. Electrochem. Soc.* **2018,** *165* (9), A1837-A1845.
21. Iclodean, C.; Varga, B.; Burnete, N.; Cimerdean, D.; Jurchiş, B., Comparison of Different Battery Types for Electric Vehicles. *IOP Conference Series: Mater. Sci. Eng.* **2017,** *252* (1), 012058.
22. Young, K.; Wang, C.; Wang, L. Y.; Strunz, K., *Electric Vehicle Integration into Modern Power Networks (Chapter: Electric Vehicle Battery Technologies)*. Springer, New York, NY: 2013.
23. Lowe, M.; Tokuoka, S.; Trigg, T.; Gereffi, G., *Lithium-ion Batteries for Electric Vehicles: the U.S. Value Chain*. 2010.
24. Astaneh, M.; Roshandel, R.; Dufo-López, R.; Bernal-Agustín, J. L., A novel framework for optimization of size and control strategy of lithium-ion battery based off-grid renewable energy systems. *Energy Convers. Manage.* **2018,** *175*, 99-111.
25. Paul Ayeng'o, S.; Schirmer, T.; Kairies, K.-P.; Axelsen, H.; Uwe Sauer, D., Comparison of off-grid power supply systems using lead-acid and lithium-ion batteries. *Solar Energy* **2018,** *162*, 140-152.
26. Office, S. M. a. A. C. *Energy Storage Technologies for Future Planetary Science Missions*; JPL D-101146; Jet Propulsion Laboratory: 2017.
27. Dunn, B.; Kamath, H.; Tarascon, J.-M., Electrical Energy Storage for the Grid: A Battery of Choices. *Science* **2011,** *334* (6058), 928.

28. Thackeray, M. M.; Wolverton, C.; Isaacs, E. D., Electrical energy storage for transportation—approaching the limits of, and going beyond, lithium-ion batteries. *Energy Environ. Sci.* **2012,** *5* (7), 7854-7863.
29. Basu, S.; Zeller, C.; Flanders, P. J.; Fuerst, C. D.; Johnson, W. D.; Fischer, J. E., Synthesis and properties of lithium-graphite intercalation compounds. *Mater. Sci. Eng.* **1979,** *38* (3), 275-283.
30. Yazami, R.; Touzain, P., *A reversible graphite-lithium negative electrode for electrochemical generators*. 1983; Vol. 9, p 365-371.
31. Graetz, J.; Ahn, C. C.; Yazami, R.; Fultz, B., Nanocrystalline and Thin Film Germanium Electrodes with High Lithium Capacity and High Rate Capabilities. *J. Electrochem. Soc.* **2004,** *151* (5), A698-A702.
32. Bourderau, S.; Brousse, T.; Schleich, D. M., Amorphous silicon as a possible anode material for Li-ion batteries. *J. Power Sources* **1999,** *81-82*, 233-236.
33. Guerard, D.; Herold, A., Intercalation of lithium into graphite and other carbons. *Carbon* **1975,** *13* (4), 337-345.
34. Zeilinger, M.; Fässler, T. F., Structural and thermodynamic similarities of phases in the Li–Tt (Tt = Si, Ge) systems: redetermination of the lithium-rich side of the Li–Ge phase diagram and crystal structures of $Li17Si_{4.0-x}Ge_x$ for x = 2.3, 3.1, 3.5, and 4 as well as $Li_{4.1}Ge$. *Dalton Trans.* **2014,** *43* (40), 14959-14970.
35. Zeilinger, M.; Kurylyshyn, I. M.; Häussermann, U.; Fässler, T. F., Revision of the Li–Si Phase Diagram: Discovery and Single-Crystal X-ray Structure Determination of the High-Temperature Phase $Li_{4.11}Si$. *Chem. Mater.* **2013,** *25* (22), 4623-4632.
36. Pell, E. M., Solubility of Lithium in germanium. *J. Phys. Chem. Solids* **1957,** *3* (1), 74-76.
37. Liu, X. H.; Liu, Y.; Kushima, A.; Zhang, S.; Zhu, T.; Li, J.; Huang, J. Y., In Situ TEM Experiments of Electrochemical Lithiation and Delithiation of Individual Nanostructures. *Adv. Energy Mater.* **2012,** *2* (7), 722-741.
38. Zhao, K.; Pharr, M.; Wan, Q.; L. Wang, W.; Kaxiras, E.; Vlassak, J.; Suo, Z., *Concurrent Reaction and Plasticity during Initial Lithiation of Crystalline Silicon in Lithium-Ion Batteries*. 2012; Vol. 159, p 238-243.
39. Weker, J. N.; Liu, N.; Misra, S.; Andrews, J. C.; Cui, Y.; Toney, M. F., In situ nanotomography and operando transmission X-ray microscopy of micron-sized Ge particles. *Energy Environ. Sci.* **2014,** *7* (8), 2771-2777.
40. Pharr, M.; Suo, Z.; Vlassak, J. J., Measurements of the Fracture Energy of Lithiated Silicon Electrodes of Li-Ion Batteries. *Nano Lett.* **2013,** *13* (11), 5570-5577.
41. Pharr, M.; Choi, Y. S.; Lee, D.; Oh, K. H.; Vlassak, J. J., Measurements of stress and fracture in germanium electrodes of lithium-ion batteries during electrochemical lithiation and delithiation. *J. Power Sources* **2016,** *304*, 164-169.
42. Lee, S. W.; Ryu, I.; Nix, W. D.; Cui, Y., Fracture of crystalline germanium during electrochemical lithium insertion. *Extreme Mechanics Letters* **2015,** *2*, 15-19.
43. Cortes, F. J. Q.; Boebinger, M. G.; Xu, M.; Ulvestad, A.; McDowell, M. T., Operando Synchrotron Measurement of Strain Evolution in Individual Alloying Anode Particles within Lithium Batteries. *ACS Energy Letters* **2018,** *3* (2), 349-355.
44. Kim, H.; Seo, M.; Park, M.-H.; Cho, J., A Critical Size of Silicon Nano-Anodes for Lithium Rechargeable Batteries. *Angew. Chem. Int. Ed.* **2010,** *49* (12), 2146-2149.
45. Liu, X. H.; Zhong, L.; Huang, S.; Mao, S. X.; Zhu, T.; Huang, J. Y., Size-Dependent Fracture of Silicon Nanoparticles During Lithiation. *ACS Nano* **2012,** *6* (2), 1522-1531.
46. McDowell, M. T.; Lee, S. W.; Harris, J. T.; Korgel, B. A.; Wang, C.; Nix, W. D.; Cui, Y., In Situ TEM of Two-Phase Lithiation of Amorphous Silicon Nanospheres. *Nano Lett.* **2013,** *13* (2), 758-764.

47. Lee, G.-H.; Kwon, S. J.; Park, K.-S.; Kang, J.-G.; Park, J.-G.; Lee, S.; Kim, J.-C.; Shim, H.-W.; Kim, D.-W., Germanium microflower-on-nanostem as a high-performance lithium ion battery electrode. *Sci. Rep.* **2014,** *4*, 6883.
48. Kumar, S. K.; Ghosh, S.; Malladi, S. K.; Nanda, J.; Martha, S. K., Nanostructured Silicon–Carbon 3D Electrode Architectures for High-Performance Lithium-Ion Batteries. *ACS Omega* **2018,** *3* (8), 9598-9606.
49. Rahman, M. A.; Song, G.; Bhatt, A. I.; Wong, Y. C.; Wen, C., Nanostructured Silicon Anodes for High-Performance Lithium-Ion Batteries. *Adv. Funct. Mater.* **2016,** *26* (5), 647-678.
50. Wu, H.; Cui, Y., Designing nanostructured Si anodes for high energy lithium ion batteries. *Nano Today* **2012,** *7* (5), 414-429.
51. Zhao, X.; Niketic, S.; Yim, C.-H.; Zhou, J.; Wang, J.; Abu-Lebdeh, Y., Revealing the Role of Poly(vinylidene fluoride) Binder in Si/Graphite Composite Anode for Li-Ion Batteries. *ACS Omega* **2018,** *3* (9), 11684-11690.
52. Son, S.-B.; Cao, L.; Yoon, T.; Cresce, A.; Hafner, S. E.; Liu, J.; Groner, M.; Xu, K.; Ban, C., Interfacially Induced Cascading Failure in Graphite-Silicon Composite Anodes. *Advanced Science* **2019,** *6* (3), 1801007.
53. Erk, C.; Brezesinski, T.; Sommer, H.; Schneider, R.; Janek, J., Toward Silicon Anodes for Next-Generation Lithium Ion Batteries: A Comparative Performance Study of Various Polymer Binders and Silicon Nanopowders. *ACS Appl. Mater. Interfaces* **2013,** *5* (15), 7299-7307.
54. Nguyen, C. C.; Yoon, T.; Seo, D. M.; Guduru, P.; Lucht, B. L., Systematic Investigation of Binders for Silicon Anodes: Interactions of Binder with Silicon Particles and Electrolytes and Effects of Binders on Solid Electrolyte Interphase Formation. *ACS Appl. Mater. Interfaces* **2016,** *8* (19), 12211-12220.
55. Michan, A. L.; Divitini, G.; Pell, A. J.; Leskes, M.; Ducati, C.; Grey, C. P., Solid Electrolyte Interphase Growth and Capacity Loss in Silicon Electrodes. *J. Am. Chem. Soc.* **2016,** *138* (25), 7918-7931.
56. Shi, F.; Zhao, H.; Liu, G.; Ross, P. N.; Somorjai, G. A.; Komvopoulos, K., Identification of Diethyl 2,5-Dioxahexane Dicarboxylate and Polyethylene Carbonate as Decomposition Products of Ethylene Carbonate Based Electrolytes by Fourier Transform Infrared Spectroscopy. *The J. Phys. Chem. C* **2014,** *118* (27), 14732-14738.
57. Shi, F.; Ross, P. N.; Somorjai, G. A.; Komvopoulos, K., The Chemistry of Electrolyte Reduction on Silicon Electrodes Revealed by in Situ ATR-FTIR Spectroscopy. *The J. Phys. Chem. C* **2017,** *121* (27), 14476-14483.
58. Wu, M.; Xiao, X.; Vukmirovic, N.; Xun, S.; Das, P. K.; Song, X.; Olalde-Velasco, P.; Wang, D.; Weber, A. Z.; Wang, L.-W.; Battaglia, V. S.; Yang, W.; Liu, G., Toward an Ideal Polymer Binder Design for High-Capacity Battery Anodes. *J. Am. Chem. Soc.* **2013,** *135* (32), 12048-12056.
59. Jo, H.; Kim, J.; Nguyen, D.-T.; Kang, K. K.; Jeon, D.-M.; Yang, A. R.; Song, S.-W., Stabilizing the Solid Electrolyte Interphase Layer and Cycling Performance of Silicon–Graphite Battery Anode by Using a Binary Additive of Fluorinated Carbonates. *The J. Phys. Chem. C* **2016,** *120* (39), 22466-22475.
60. Lin, Y.-M.; Klavetter, K. C.; Abel, P. R.; Davy, N. C.; Snider, J. L.; Heller, A.; Mullins, C. B., High performance silicon nanoparticle anode in fluoroethylene carbonate-based electrolyte for Li-ion batteries. *Chem. Commun.* **2012,** *48* (58), 7268-7270.
61. Ngo, D. T.; Kalubarme, R. S.; Le, H. T. T.; Fisher, J. G.; Park, C.-N.; Kim, I.-D.; Park, C.-J., Carbon-Interconnected Ge Nanocrystals as an Anode with Ultra-Long-Term Cyclability for Lithium Ion Batteries. *Adv. Funct. Mater.* **2014,** *24* (33), 5291-5298.
62. Forney, M. W.; Dzara, M. J.; Doucett, A. L.; Ganter, M. J.; Staub, J. W.; Ridgley, R. D.; Landi, B. J., Advanced germanium nanoparticle composite anodes using single wall carbon nanotube conductive additives. *J. Mater. Chem. A* **2014,** *2* (35), 14528-14535.

63. Piper, D. M.; Evans, T.; Leung, K.; Watkins, T.; Olson, J.; Kim, S. C.; Han, S. S.; Bhat, V.; Oh, K. H.; Buttry, D. A.; Lee, S.-H., Stable silicon-ionic liquid interface for next-generation lithium-ion batteries. *Nat. Commun.* **2015,** *6*.
64. Gao, X.; Luo, W.; Zhong, C.; Wexler, D.; Chou, S.-L.; Liu, H.-K.; Shi, Z.; Chen, G.; Ozawa, K.; Wang, J.-Z., Novel Germanium/Polypyrrole Composite for High Power Lithium-ion Batteries. *Sci. Rep.* **2014,** *4*, 6095.
65. Wu, M.; Song, X.; Liu, X.; Battaglia, V.; Yang, W.; Liu, G., Manipulating the polarity of conductive polymer binders for Si-based anodes in lithium-ion batteries. *J. Mater. Chem. A* **2015,** *3* (7), 3651-3658.
66. Jones, E. M. C.; Çapraz, Ö. Ö.; White, S. R.; Sottos, N. R., Reversible and Irreversible Deformation Mechanisms of Composite Graphite Electrodes in Lithium-Ion Batteries. *J. Electrochem. Soc.* **2016,** *163* (9), A1965-A1974.
67. Higgins, T. M.; Park, S.-H.; King, P. J.; Zhang, C.; McEvoy, N.; Berner, N. C.; Daly, D.; Shmeliov, A.; Khan, U.; Duesberg, G.; Nicolosi, V.; Coleman, J. N., A Commercial Conducting Polymer as Both Binder and Conductive Additive for Silicon Nanoparticle-Based Lithium-Ion Battery Negative Electrodes. *ACS Nano* **2016,** *10* (3), 3702-3713.
68. Zhao, H.; Wei, Y.; Wang, C.; Qiao, R.; Yang, W.; Messersmith, P. B.; Liu, G., Mussel-Inspired Conductive Polymer Binder for Si-Alloy Anode in Lithium-Ion Batteries. *ACS Appl. Mater. Interfaces* **2018,** *10* (6), 5440-5446.
69. Haregewoin, A. M.; Wotango, A. S.; Hwang, B.-J., Electrolyte additives for lithium ion battery electrodes: progress and perspectives. *Energy Environ. Sci.* **2016,** *9* (6), 1955-1988.
70. Henriksen, G. L.; Amine, K.; Liu, J.; Nelson, P. A. *Materials Cost Evaluation Report For High-Power Li-ion HEV Batteries*; Argonne National Laboratory: U.S. Department of Energy, 2002.
71. Lux, S. F.; Lucas, I. T.; Pollak, E.; Passerini, S.; Winter, M.; Kostecki, R., The mechanism of HF formation in $LiPF_6$ based organic carbonate electrolytes. *Electrochem. Commun.* **2012,** *14* (1), 47-50.
72. Yu, L.; Liu, H.; Wang, Y.; Kuwata, N.; Osawa, M.; Kawamura, J.; Ye, S., Preferential Adsorption of Solvents on the Cathode Surface of Lithium Ion Batteries. *Angew. Chem. Int. Ed.* **2013,** *52* (22), 5753-5756.
73. Horowitz, Y.; Han, H.-L.; Soto, F. A.; Ralston, W.; Balbuena, P. B.; Somorjai, G. A., Fluoroethylene Carbonate as a Directing Agent in Amorphous Silicon Anodes - Electrolyte Interface Structure Probed by Sum Frequency Vibrational Spectroscopy and Ab-initio Molecular Dynamics. *Nano Lett.* **2017**.
74. Horowitz, Y.; Steinrück, H.-G.; Han, H.-L.; Cao, C.; Abate, I. I.; Tsao, Y.; Toney, M. F.; Somorjai, G. A., Fluoroethylene Carbonate Induces Ordered Electrolyte Interface on Silicon and Sapphire Surfaces as Revealed by Sum Frequency Generation Vibrational Spectroscopy and X-ray Reflectivity. *Nano Lett.* **2018,** *18* (3), 2105-2111.
75. Neaton, J. B.; Hybertsen, M. S.; Louie, S. G., Renormalization of Molecular Electronic Levels at Metal-Molecule Interfaces. *Phys. Rev. Lett.* **2006,** *97* (21), 216405.
76. Garcia-Lastra, J. M.; Rostgaard, C.; Rubio, A.; Thygesen, K. S., Polarization-induced renormalization of molecular levels at metallic and semiconducting surfaces. *Physical Review B* **2009,** *80* (24), 245427.
77. Kumar, N.; Siegel, D. J., Interface-Induced Renormalization of Electrolyte Energy Levels in Magnesium Batteries. *J Phys Chem Lett* **2016,** *7* (5), 874-81.
78. Horowitz, Y.; Han, H.-L.; Somorjai, G. A., Identifying the Decomposition of Diethyl Carbonate in Binary Electrolyte Solution in Contact with Silicon Anodes - A Sum Frequency Generation Vibrational Spectroscopy Study. *Industrial & Engineering Chemistry Research* **2018**.
79. Márquez, A.; Balbuena, P. B., Molecular Dynamics Study of Graphite/Electrolyte Interfaces. *J. Electrochem. Soc.* **2001,** *148* (6), A624-A635.
80. Bruce, P. G., Solid-state chemistry of lithium power sources. *Chem. Commun.* **1997**, 1817-1824.

81. Saubanère, M.; Yahia, M. B.; Lebègue, S.; Doublet, M. L., An intuitive and efficient method for cell voltage prediction of lithium and sodium-ion batteries. *Nat. Commun.* **2014,** *5*, 5559.
82. Gerischer, H., Decker, F., Scrosati, B., The Electronic and the Ionic Contribution to the Free Energy of Alkali Metals in Intercalation Compounds. *J. Electrochem. Soc.* **1994,** *141* (9), 2273-2578.
83. Birkl, C. R.; McTurk, E.; Roberts, M. R.; Bruce, P. G.; Howey, D. A., A Parametric Open Circuit Voltage Model for Lithium Ion Batteries. *J. Electrochem. Soc.* **2015,** *162* (12), A2271-A2280.
84. Schweidler, S.; de Biasi, L.; Schiele, A.; Hartmann, P.; Brezesinski, T.; Janek, J., Volume Changes of Graphite Anodes Revisited: A Combined Operando X-ray Diffraction and In Situ Pressure Analysis Study. *The J. Phys. Chem. C* **2018,** *122* (16), 8829-8835.
85. Reynier, Y.; Yazami, R.; Fultz, B., The entropy and enthalpy of lithium intercalation into graphite. *J. Power Sources* **2003,** *119–121*, 850-855.
86. Liu, C.; Neale, Z. G.; Cao, G., Understanding electrochemical potentials of cathode materials in rechargeable batteries. *Mater. Today* **2016,** *19* (2), 109-123.
87. Reynier, Y. F.; Yazami, R.; Fultz, B., Thermodynamics of Lithium Intercalation into Graphites and Disordered Carbons. *J. Electrochem. Soc.* **2004,** *151* (3), A422.
88. Liu, Q.; Li, S.; Wang, S.; Zhang, X.; Zhou, S.; Bai, Y.; Zheng, J.; Lu, X., Kinetically Determined Phase Transition from Stage II (LiC_{12}) to Stage I (LiC_6) in a Graphite Anode for Li-Ion Batteries. *The J. Phys. Chem. Lett.* **2018,** *9* (18), 5567-5573.
89. Morris, A. J.; Grey, C. P.; Pickard, C. J., Thermodynamically stable lithium silicides and germanides from density functional theory calculations. *Physical Review B* **2014,** *90* (5), 054111.
90. Zhang, Q.; Cui, Y.; Wang, E., First-principles approaches to simulate lithiation in silicon electrodes. *Modell. Simul. Mater. Sci. Eng.* **2013,** *21* (7), 074001.
91. Loaiza, L. C.; Louvain, N.; Fraisse, B.; Boulaoued, A.; Iadecola, A.; Johansson, P.; Stievano, L.; Seznec, V.; Monconduit, L., Electrochemical Lithiation of Ge: New Insights by Operando Spectroscopy and Diffraction. *The J. Phys. Chem. C* **2018,** *122* (7), 3709-3718.
92. Obrovac, M. N.; Christensen, L., Structural Changes in Silicon Anodes during Lithium Insertion/Extraction. *Electrochem. Solid-State Lett.* **2004,** *7* (5), A93-A96.
93. Ruffo, R.; Hong, S. S.; Chan, C. K.; Huggins, R. A.; Cui, Y., Impedance Analysis of Silicon Nanowire Lithium Ion Battery Anodes. *The J. Phys. Chem. C* **2009,** *113* (26), 11390-11398.
94. Tang, W.; Liu, Y.; Peng, C.; Hu, M. Y.; Deng, X.; Lin, M.; Hu, J. Z.; Loh, K. P., Probing Lithium Germanide Phase Evolution and Structural Change in a Germanium-in-Carbon Nanotube Energy Storage System. *J. Am. Chem. Soc.* **2015,** *137* (7), 2600-2607.
95. Schott, T.; Robert, R.; Ulmann, P. A.; Lanz, P.; Zürcher, S.; Spahr, M. E.; Novák, P.; Trabesinger, S., Cycling Behavior of Silicon-Containing Graphite Electrodes, Part A: Effect of the Lithiation Protocol. *The J. Phys. Chem. C* **2017,** *121* (34), 18423-18429.
96. Key, B.; Morcrette, M.; Tarascon, J.-M.; Grey, C. P., Pair Distribution Function Analysis and Solid State NMR Studies of Silicon Electrodes for Lithium Ion Batteries: Understanding the (De)lithiation Mechanisms. *J. Am. Chem. Soc.* **2011,** *133* (3), 503-512.
97. Ogata, K.; Salager, E.; Kerr, C. J.; Fraser, A. E.; Ducati, C.; Morris, A. J.; Hofmann, S.; Grey, C. P., Revealing lithium–silicide phase transformations in nano-structured silicon-based lithium ion batteries via in situ NMR spectroscopy. **2014,** *5*, 3217.
98. Ke, F.-S.; Mishra, K.; Jamison, L.; Peng, X.-X.; Ma, S.-G.; Huang, L.; Sun, S.-G.; Zhou, X.-D., Tailoring nanostructures in micrometer size germanium particles to improve their performance as an anode for lithium ion batteries. *Chem. Commun.* **2014,** *50* (28), 3713-3715.
99. Molina Piper, D.; Evans, T.; Xu, S.; Kim, S. C.; Han, S. S.; Liu, K. L.; Oh, K. H.; Yang, R.; Lee, S.-H., Optimized Silicon Electrode Architecture, Interface, and Microgeometry for Next-Generation Lithium-Ion Batteries. *Adv. Mater.* **2016,** *28* (1), 188-193.

100. Kim, H.; Son, Y.; Lee, J.; Lee, M.; Park, S.; Cho, J.; Choi, H. C., Nanocomb Architecture Design Using Germanium Selenide as High-Performance Lithium Storage Material. *Chem. Mater.* **2016,** *28* (17), 6146-6151.
101. Xiao, X.; Li, X.; Zheng, S.; Shao, J.; Xue, H.; Pang, H., Nanostructured Germanium Anode Materials for Advanced Rechargeable Batteries. *Adv. Mater. Interfaces* **2017,** *4* (6), 1600798.
102. Sakabe, J.; Ohta, N.; Ohnishi, T.; Mitsuishi, K.; Takada, K., Porous amorphous silicon film anodes for high-capacity and stable all-solid-state lithium batteries. *Communications Chemistry* **2018,** *1* (1), 24.
103. Sandu, G.; Coulombier, M.; Kumar, V.; Kassa, H. G.; Avram, I.; Ye, R.; Stopin, A.; Bonifazi, D.; Gohy, J.-F.; Leclère, P.; Gonze, X.; Pardoen, T.; Vlad, A.; Melinte, S., Kinked silicon nanowires-enabled interweaving electrode configuration for lithium-ion batteries. *Sci. Rep.* **2018,** *8* (1), 9794.
104. Bazant, M. Z., Theory of Chemical Kinetics and Charge Transfer based on Nonequilibrium Thermodynamics. *Acc. Chem. Res.* **2013,** *46* (5), 1144-1160.
105. Luck, J.; Latz, A., Theory of reactions at electrified interfaces. *PCCP* **2016,** *18* (27), 17799-17804.
106. Xu, K., "Charge-Transfer" Process at Graphite/Electrolyte Interface and the Solvation Sheath Structure of Li^+ in Nonaqueous Electrolytes. *J. Electrochem. Soc.* **2007,** *154* (3), A162-A167.
107. Xu, K.; Lam, Y.; Zhang, S. S.; Jow, T. R.; Curtis, T. B., Solvation Sheath of Li^+ in Nonaqueous Electrolytes and Its Implication of Graphite/Electrolyte Interface Chemistry. *The J. Phys. Chem. C* **2007,** *111* (20), 7411-7421.
108. Kang, J.; Wei, S.-H.; Zhu, K.; Kim, Y.-H., First-Principles Theory of Electrochemical Capacitance of Nanostructured Materials: Dipole-Assisted Subsurface Intercalation of Lithium in Pseudocapacitive TiO_2 Anatase Nanosheets. *The J. Phys. Chem. C* **2011,** *115* (11), 4909-4915.
109. Jow, T. R.; Delp, S. A.; Allen, J. L.; Jones, J.-P.; Smart, M. C., Factors Limiting Li+ Charge Transfer Kinetics in Li-Ion Batteries. *J. Electrochem. Soc.* **2018,** *165* (2), A361-A367.
110. Smith, A. J.; Dahn, J. R., Delta Differential Capacity Analysis. *J. Electrochem. Soc.* **2012,** *159* (3), A290-A293.
111. Talaie, E.; Bonnick, P.; Sun, X.; Pang, Q.; Liang, X.; Nazar, L. F., Methods and Protocols for Electrochemical Energy Storage Materials Research. *Chem. Mater.* **2017,** *29* (1), 90-105.
112. Hatzikraniotis, E.; Mitsas, C. L.; Siapkas, D. I., Differential Capacity Analysis, a Tool to Examine the Performance of Graphites for Li-Ion Cells. In *Materials for Lithium-Ion Batteries*, Julien, C.; Stoynov, Z., Eds. Springer Netherlands: Dordrecht, 2000; pp 529-534.
113. Ohzuku, T.; Iwakoshi, Y.; Sawai, K., Formation of Lithium-Graphite Intercalation Compounds in Nonaqueous Electrolytes and Their Application as a Negative Electrode for a Lithium Ion (Shuttlecock) Cell. *J. Electrochem. Soc.* **1993,** *140* (9), 2490-2498.

Chapter 2: Vibrational Spectroscopy

2.1: Preface

The goal of this chapter is to describe the underlying principles of vibrational spectroscopic techniques relevant to chapters 3 and 5. An overarching theme throughout this chapter is the effect that optical electromagnetic fields (E-fields) of light have upon a molecular functional group of interest. In section 2.2, vibrational infrared and Raman spectroscopies are distinguished from each other through their *linear* responses to an E-field. Section 2.3 describes the effect of increasing the E-field magnitude to change the response of a vibrational reporter to be *non-linear*. Finally, section 2.4 details how the alignment between a vibrational reporter and electric field of single polarity (by a fixed DC bias) will manifest in different spectroscopic line shapes through the vibrational Stark effect.

2.2: Linear Spectroscopies

Spectroscopy refers to the study of matter by excitation with electromagnetic radiation, the energy of which can range from the X-ray and ultraviolet/visible to the far infrared and microwave regimes. In vibrational spectroscopy, the resonant excitations occur in the mid-infrared (2500 - 25000 nm) region.[114] The mechanism of excitation is a coupling between the transition dipole moment of a functional group within a molecule and the oscillating E-field of light: when the frequency of the light matches the resonance frequency of the vibration, energy can be delivered to the molecular system as the vibrational mode is excited from its fundamental state (v_0) to higher levels (v_1, v_2 etc.).[115] The spacing between the energy levels of each vibrational state is represented by the quantization of an anharmonic potential well that accounts for the potential energy associated with the internuclear separation between the atoms comprising the molecular vibration.[116] When the energy of the light is increased outside of the infrared and into the visible regime, vibrational transitions cannot be resonantly excited as the mass of the nuclei precludes rapid motion. However, the electrons are much lighter and their movement can be modulated by the oscillating E-field, which leads to an induced polarization in the material. This concept is more formally expressed by:

$$\vec{\mu}_{ind} = \alpha\vec{E} \qquad (2.1)$$

Where the induced dipole moment $\vec{\mu}_{ind}$ is instantaneously formed by coupling between the polarizability α and E-field. Because the E-field of light is oscillating, the induced dipole will also oscillate and lead to the formation of secondary waves.[117] The majority of these waves oscillate with the same frequency as the incident E-field and is the origin of scattering. However, if the movement of nuclei in the material is associated with a change in α, secondary waves with a shift in frequency can also be

produced. This non-resonant phenomenon leads to inelastic scattering, called Raman scattering, and results in transitions between energy levels of the vibrational modes. The scattered photon will either lose energy (Stokes Raman) or pick up energy (anti-Stokes Raman), and the relative efficiency of the two depends on the population densities in the ground state vs. excited state of the sample; at room temperature the Stokes signals are several times stronger than the anti-Stokes due to the higher population of the v_0 state per the Boltzmann distribution.[118]

To summarize, there are two main mechanisms for the excitation of vibrational modes with electromagnetic waves. For resonant transitions mediated via the transition dipole moment, the E-field frequency must match the spacing between energy levels, and it can be shown that the vibration must exhibit a nonzero derivative of the molecular dipole moment at the equilibrium internuclear distance. For nonresonant transitions mediated via the transition polarizability α, light of any frequency can be used and the vibration must exhibit a nonzero derivative of the molecular polarizability at the equilibrium nuclear separation. The IR and/or Raman activity of a molecular group is also related to its symmetry,[119] a concept that will be further discussed in section 2.2.

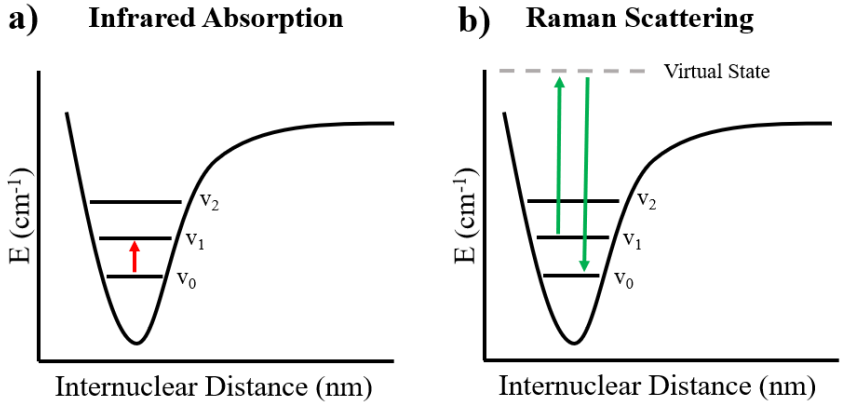

Figure 1: Spacing between vibrational energy states confined to an anharmonic potential well. Infrared absorption (Figure a) occurs from the vibrational ground state v_0, while an anti-Stokes Raman scattering process (Figure b) occurs from a v_1 state (produced by thermal energy) and relaxes down to v_0 from a virtual excited state.

Because the incident E-field of light induces molecular vibrations in many molecules at once within a sample, a more practical expression of Eq. 2.1 is the polarization response, P, representing the sum of induced dipole moments per unit volume:

$$P = \varepsilon_0 \chi^{(1)} E \qquad (2.2)$$

Where ε_0 is the vacuum permittivity and $\chi^{(1)}$ is the linear first order susceptibility, which is related to the macroscopic average of α.

2.3: Non-linear vibrational Sum Frequency Generation spectroscopy

The above description of the molecular dipole approximation and induced polarization express a linear relationship between P and E, therefore invoking the term linear spectroscopies; vibrational infrared and Raman are linear spectroscopies. Spontaneous Raman scattering is incoherent because the vibrations that yield a signal does not exhibit a well-defined phase relation with each other. However, if the phase of their vibrations are resonantly driven by a laser, the anti-Stokes Raman photons will be coherently produced,[120-121] which can yield signal enhancement. This process is utilized in vibrational sum-frequency generation (v-SFG) spectroscopy, which operates under a scenario where both infrared and visible lasers are temporally coincident upon a sample and phase-matched,[122] resulting in a synchronized infrared absorption and anti-Stokes shift enhancement. This process produces a photon at the sum of the incoming light frequencies (Figure 2) and is aptly termed sum-frequency generation.

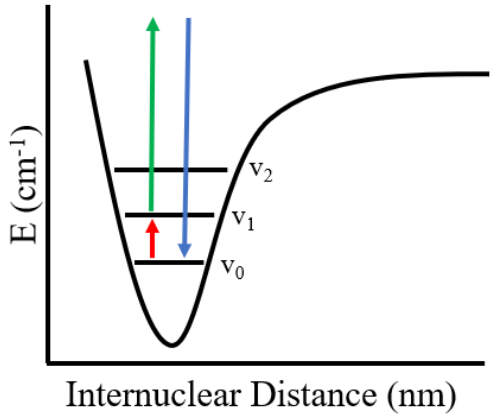

Figure 2: Vibrational sum-frequency generation process. Infrared light induces a vibrational excitation from $v_0 \rightarrow v_1$, whereupon visible light upconverts the energy of the photon to emit at the sum-frequency of both incident photons to a virtual excited state, relaxing back to v_0 by an anti-Stokes shift.

Unlike linear spectroscopies, the ability to produce v-SFG requires the E-fields of light are comparable to the fields experienced by electrons in the molecule, requiring the use of high-power lasers.[123] This is realized by the use of a short-pulsed laser, which leads to enormous peak power intensities for each pulse of light. In effect, the E term expressed in the previous equations becomes too large to be expressed with a linear relationship to the polarization response. As one might assume, this kind of vibrational spectroscopy is termed non-linear spectroscopy. The effect of the high E-fields of light is more formally expressed as an expansion of Eq. 2.1:

$$\vec{\mu}_{ind} = \alpha E + ß\,(E_{vis} \bullet E_{IR}) \qquad (2.3)$$

Where the ß term represents the molecular hyperpolarizability, or the degree of polarization of a dielectric to an E-field. The E-fields of light are now separately represented by E_{vis} and E_{IR}. As v-SFG spectroscopy also measures the response of an ensemble of molecules within a volume to the electric fields of light as linear spectroscopies do, the ß term is better represented with $\chi^{(2)}_{ijk}$, termed the second order susceptibility. $\chi^{(2)}_{ijk}$ is a rank 3 tensor with i, j, and k representing all combinations of the Cartesian coordinates (x, y, and z) describing the field components of the produced SFG response,[124] as well as E_{vis} and E_{IR}. By analogy to the transition from Eq. 2.1 to Eq. 2.2, one can then redefine Equation 3 to account for the induced non-linear polarization:

$$P = \varepsilon_0 (\chi^{(1)} \bullet E + \chi^{(2)}_{ijk} \bullet E_{vis} \bullet E_{IR}) \quad (2.4)$$

The term responsible for the generation of SFG includes $\chi^{(2)}_{ijk}$, and Eq. 2.4 can be simplified to:

$$I_{SFG} = P^2 = \left| \chi^{(2)}_{ijk} \bullet E_{vis} E_{IR} \right|^2 \quad (2.5)$$

Where I_{SFG} is the intensity of the v-SFG signal. In a v-SFG experiment, a collection of the $\chi^{(2)}_{ijk}$ tensor elements are probed, which contribute to the vibrational activity induced by a specific polarization combination.[125] The notation for the incident and emitted light is by convention listed in order of decreasing photon energy (i.e. pps= p-polarized v-SFG, p-polarized E_{vis} and s-polarized E_{IR}). Consideration of the light polarizations is important because the molecular orientation relative the cartesian coordinates defined by the E-field directions affects their v-SFG response in a given polarization combination. Figure 7 establishes this system using an example at an interphase between an electrode an electrolyte solvent; the carbonyl functional group of a representative carbonate electrolyte solvent is used because it is a consistently referenced functional group throughout this dissertation. Both s-polarized infrared light and p-polarized visible light are temporally coincident upon the electrode/electrolyte junction; the electric field of s-polarized light oscillates about the x-y axis, while p-polarized light oscillates about the x-z axis. The photon emitted at the sum-frequency can be measured in s or p-polarization. Using the established coordinate system in Figure 7 reveals a new point group of symmetry along the surface normal for an ensemble of molecules that adsorb with a preferred tilt, but arbitrary azimuthal and twist angles: C_∞. This is a common symmetry for molecules on surfaces, which simplifies the interpretation of v-SFG experiments by limiting the range of nonzero $\chi^{(2)}_{ijk}$. It is from this point group that vibrational activity will be discussed below.

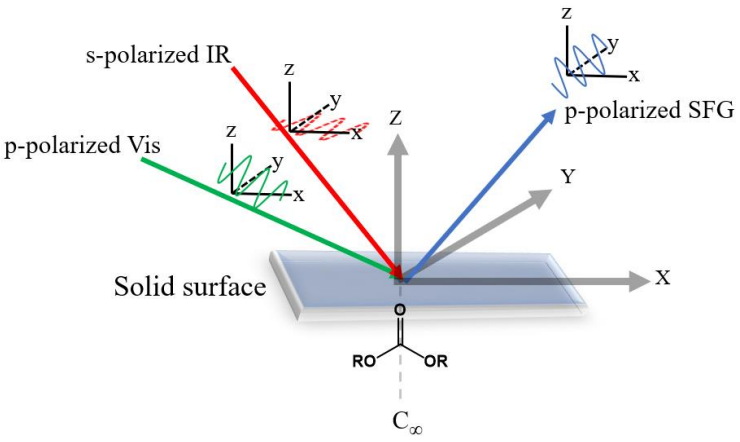

Figure 3: A laboratory coordinate system is established to provide axes for the polarization combination of light to be defined (pps in the above depiction). This reveals a C_∞ axis of symmetry at the junction between a solid surface and C=O group.

In principle, various combinations of incident s- and p-polarized light from E_{vis} and E_{IR} should in total probe 27 tensor elements of $\chi^{(2)}_{ijk}$ because it describes the mixing of three beams with three spatial directions each (3^3=27). In practice, however, only 13 of these elements are v-SFG active for C_∞ symmetries;[126] the rest must be zero. This can be shown by the application of symmetry operators to the C_∞ axis that must result in a scenario that yields an equivalent induced polarization, P. For example, consider an attempt from the experimentalist to probe $\chi^{(2)}_{xxx}$ (using the ppp polarization combination): By changing the x-direction of incident beams in the laboratory coordinate system from +x to -x (Figure 4a to 4b); group theory would describe this as a rotational operation, equivalent to a 180° rotation about the z-axis. Due to the C_∞ symmetry of the sample, $\chi^{(2)}_{xxx} = \chi^{(2)}_{-xxx}$ must hold. By switching the direction with which the incident electric field of light traverses, $P_{SFG} \rightarrow -P_{SFG}$, changing the sign of the left-hand side in Eq. 2.4. Likewise, $E_{vis} \rightarrow -E_{vis}$ and $E_{IR} \rightarrow -E_{IR}$, which means there will be no net switch in sign on the right-hand side in Eq. 2.4. In other words, Eq. 2.4 predicts both a switch and a preservation in sign, which can only be correct when $\chi^{(2)}_{xxx} = 0$, so no v-SFG spectrum will be generated for this tensor element. Despite this, the polarization combination of ppp is often used because it probes the highest number (4) of the 13 active tensor elements in a single spectral collection, giving good prospect for nonzero signals.[127] Applying the example summarized in Figure 8 to the 27 available tensor elements, one can see that for odd numbers of x and y (Table 2.1), there will be no v-SFG activity for molecules exhibiting C_∞ symmetry.

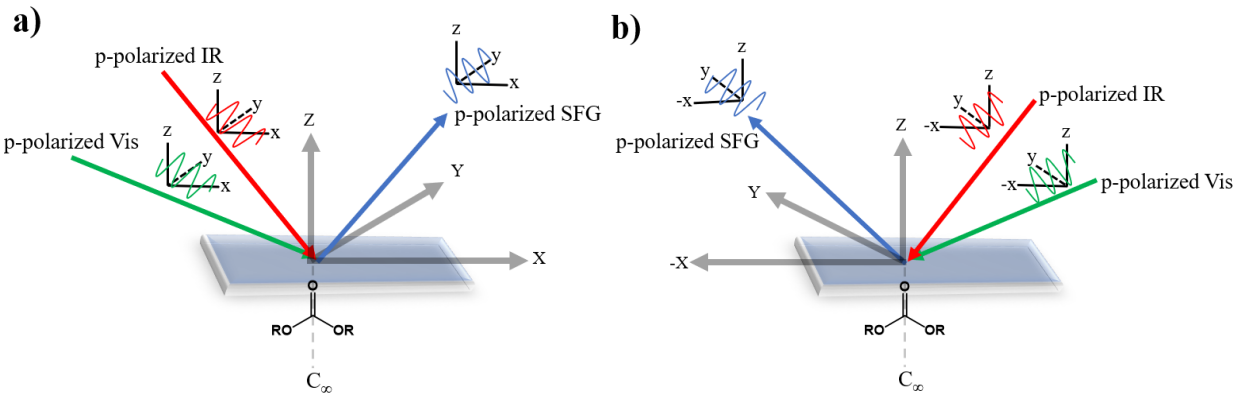

Figure 4: Equal and opposite polarities of E_{vis} and E_{IR} fields (between Figures a and b) do not maintain the equality P = $\chi^{(2)}_{xyz}$, making this tensor element SFG-silent.

Polarization Combination	Tensor Elements
ppp	$\underline{\chi^{(2)}_{zzz}}, \chi^{(2)}_{zzx}, \chi^{(2)}_{zxz}, \chi^{(2)}_{xzz}, \underline{\chi^{(2)}_{zxx}}, \underline{\chi^{(2)}_{xzx}}, \underline{\chi^{(2)}_{xxz}}, \chi^{(2)}_{xxx}$
pps	$\chi^{(2)}_{zzy}, \underline{\chi^{(2)}_{zxy}}, \underline{\chi^{(2)}_{xzy}}, \chi^{(2)}_{xxy}$
psp	$\chi^{(2)}_{zyz}, \underline{\chi^{(2)}_{zyx}}, \underline{\chi^{(2)}_{xyz}}, \chi^{(2)}_{xyx}$
spp	$\chi^{(2)}_{yzz}, \underline{\chi^{(2)}_{yzx}}, \underline{\chi^{(2)}_{yxz}}, \chi^{(2)}_{yxx}$
pss	$\underline{\chi^{(2)}_{zyy}}, \chi^{(2)}_{xyy}$
sps	$\underline{\chi^{(2)}_{yzy}}, \chi^{(2)}_{yxy}$
ssp	$\underline{\chi^{(2)}_{yyz}}, \chi^{(2)}_{yyx}$
sss	$\chi^{(2)}_{yyy}$

Table 1: Specification of SFG-active and silent (underlined) $\chi^{(2)}_{ijk}$ modes, as well as the polarization combination of light needed to probe each mode. Adapted from Ref. 126

The inspiration to use v-SFG in this work originates from the high interface specificity of the technique, a property that can be illustrated with phase relationships of the P response for molecules in various organizations.[126] Recalling that $\chi^{(2)}_{ijk}$ represents the polarization (P) response from an ensemble of molecules, it should be recalled that the dipole moments are coherently oscillating in response to the E_{vis} and E_{IR} fields as discussed in section 2.2. At interfaces, the preferred orientation adopted by molecules due the surface interactions lead to a constructive interference and an enhanced v-SFG signal.[128] However, in isotropic environments, the existence of opposite orientations for the molecules lead to destructive interference and no detectable signal. This concept can be visualized by considering cases a and b in Figure 9, representing a region at the electrode/electrolyte interphase (9 a) and away from the

electrode/electrolyte junction (9 b, representing an ideally isotropic environment). In Figure 8a, the oriented C=O groups will result in a coherent and constructive polarization response, while destructive interference occurs for vibrational modes in the isotropic system (8b).

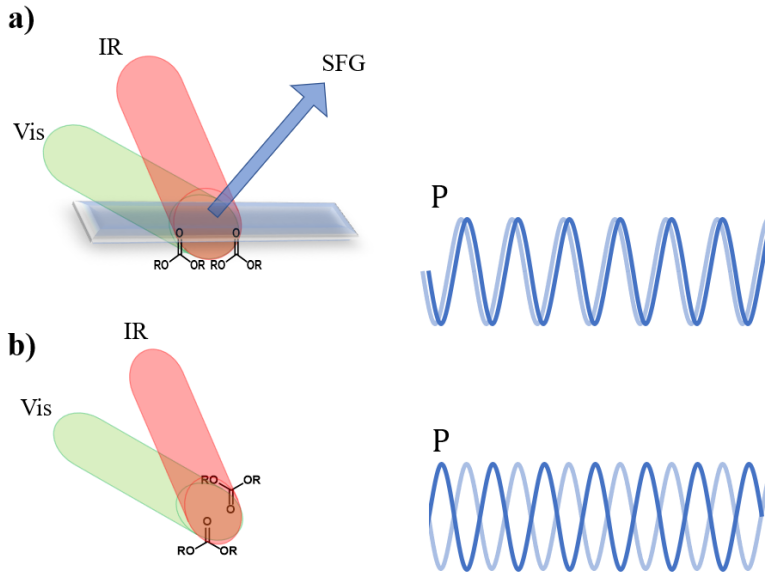

Figure 5: a) the preferential orientation of molecules at an interface enables dipole moments to oscillate in phase from coincident IR and Vis photons, enabling v-SFG. b) in an isotropic environment, the phase relation leads to destructively interfering polarization responses that prevent the emission of photons at the sum of IR and Vis frequencies.

2.4: Vibrational Stark effect spectroscopy

While section 2.2 focuses on the effect of strong *oscillating* electric fields upon a chromophore, an effect of strong DC electric fields upon it is a change to its absorption profile. Johannes Stark was the first to observe this effect over a hundred years ago,[129] birthing the field of Stark effect spectroscopy. In the context of vibrational spectroscopy, the vibrational Stark effect (VSE) has been described for infrared absorbers most, the theoretical basis of which has been most notably deconvoluted by Boxer and colleagues for the past several decades.[130-132]

As described in section 2.1, the transition energy from the ground to excited state ($v_0 \rightarrow v_1$) of a molecular vibration possessing a permanent dipole moment requires the incident electric field of light to match the spacing between these energy levels. Unique to each of these states is extent of charge separation between positive and negative poles of the dipole; at the higher vibrational energy level v_1, there is an increase to the bond length *d*. As a result, the vibration of interest has a larger dipole moment in the v_1 state than the v_0 state (Figure 9). The transition energy therefore is directly correlated with the difference in dipole moments between the v_0 and v_1 energy levels. This difference, represented with $\Delta\vec{\mu}$,

was traditionally expressed in units of Debye (D), but over the past several years is now more formally referenced in units of $cm^{-1}/(MV/cm)$; 1D= 16.8 $cm^{-1}/(MV/cm)$.[132]

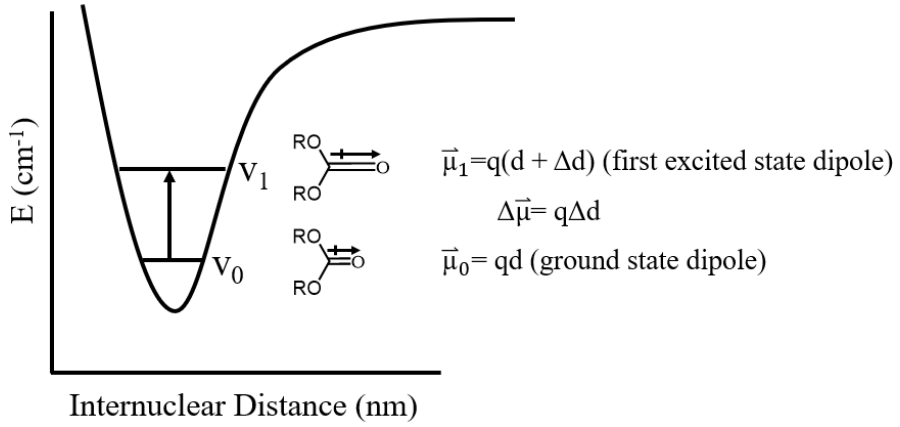

Figure 6: Between the ground and first vibrational energy states of a C=O stretching vibration, its dipole moment changes (represented with the symbol ↠) due to an increase in charge separation (q) over a bond distance d.

The mechanism with which the absorbance profile of a vibrational mode changes while under the influence of *static* DC fields is by perturbation of the transition energy (Figure 7a).[133-134] Assessed in two extremes (7 b), the vibrational transition energy changes due to the C=O dipole moment being more or less stabilized by its vector aligning parallel or antiparallel to an electric field vector, manifesting in a shift in absorption energy to lower (red) or higher (blue) values. The value of $\Delta\vec{\mu}$ therefore associates a shift in transition energy (a shift in peak absorption) to the magnitude of a field projected onto it. Direct measurements of the value of $\Delta\vec{\mu}$ are made with a DC power supply and infrared spectrometer to calibrate shifts in vibrational absorption energy,[135-136] whereupon the vibrational reporter can be used as a molecular voltmeter in applications where vibrational peak shifts are hypothesized to be a consequence of strong electric fields on the order of MV/cm.

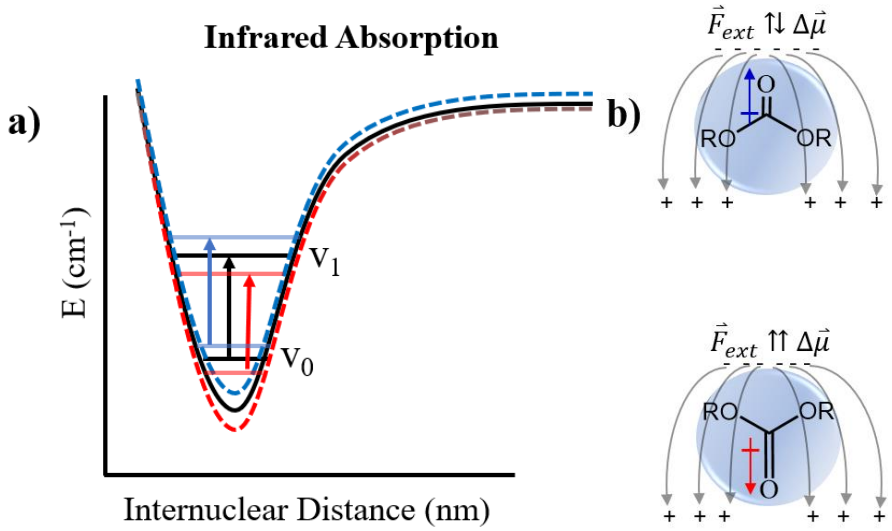

Figure 7: a) between the v_0 and v_1 energy levels, a DC electric field shifts the vibrational transition energy to higher (blue) and lower (red) values. b) depending on the orientation of the difference dipole vector relative to the DC field vector, the dipole moment is more or less stabilized, resulting in a blue or red shift.

Applications of the vibrational Stark effect had been popularized by their use in the calculation of electrostatic fields within enzyme active sites.[137-138] Recently, the transferability of Stark effects to study electrochemical processes has realized in energy materials, significantly advancing the understanding of electrocatalysis,[139-142] photovoltaic efficiencies,[143-153] and redox potentials.[154-155] This has been particularly useful because the calibration of a chromophore to electric fields requires the application of MV/cm upon the chromophore in Stark effect spectroscopy, which are similar in magnitude to those predicted as at electrochemical interfaces.[156-157]

2.5 References:

114. Reichenbächer, M.; Popp, J., *Challenges in Molecular Structure Determination*. 2012.
115. Andrews, D. L., Mechanism for the absorption of light. In *Molecular Photophysics and Spectroscopy*, Morgan & Claypool Publishers: 2014; pp 3-1-3-4.
116. Sathyanarayana, D. N., *Vibrational Spectroscopy: Theory and Applications*. New Age International (P) Limited: 2015.
117. Siebert, F.; Hildebrandt, P., Vibrational Spectroscopy in Life Science. Wiley-VCH: 2008.
118. Ornstein, L. S.; Rekveld, J.; Utrecht, Intensity Measurements in the Raman Effect and the Distribution Law of Maxwell-Boltzmann. *Physical Review* **1929,** *34* (5), 720-725.
119. Rykhlinskaya, K.; Fritzsche, S., Use of group theory for the analysis of vibrational spectra. *Comput. Phys. Commun.* **2004,** *162* (2), 124-142.
120. Pestov, D.; Ariunbold, G. O.; Wang, X.; Murawski, R. K.; Sautenkov, V. A.; Sokolov, A. V.; Scully, M. O., Coherent versus incoherent Raman scattering: molecular coherence excitation and measurement. *Opt. Lett.* **2007,** *32* (12), 1725-1727.
121. Tolles, W. M.; Turner, R. D., A Comparative Analysis of the Analytical Capabilities of Coherent Anti-Stokes Raman Spectroscopy (CARS) Relative to Raman Scattering and Absorption Spectroscopy. *Appl. Spectrosc.* **1977,** *31* (2), 96-103.

122. Vidal, F.; Tadjeddine, A., Sum-frequency generation spectroscopy of interfaces. *Rep. Prog. Phys.* **2005,** *68* (5), 1095-1127.
123. Lambert, A. G.; Davies, P. B.; Neivandt, D. J., Implementing the Theory of Sum Frequency Generation Vibrational Spectroscopy: A Tutorial Review. *Applied Spectroscopy Reviews* **2005,** *40* (2), 103-145.
124. Vauthey, E. Introduction to nonlinear optical spectroscopic techniques for investigating ultrafast processes *Lectures of Virtual European University on Lasers* [Online]. http://www.mitr.p.lodz.pl/evu/wyklady.
125. Wang, H.-F.; Velarde, L.; Gan, W.; Fu, L., Quantitative Sum-Frequency Generation Vibrational Spectroscopy of Molecular Surfaces and Interfaces: Lineshape, Polarization, and Orientation. *Annu. Rev. Phys. Chem.* **2015,** *66* (1), 189-216.
126. Hofmann, M. J.; Koelsch, P., Introduction to Quantitative Data Analysis in Vibrational Sum-Frequency Generation Spectroscopy. In *Soft Matter at Aqueous Interfaces*, Lang, P. R.; Liu, Y., Eds. Springer International Publishing: Cham, 2016; pp 491-513.
127. Johansson, P.; Schmüser, L.; G. Castner, D., *Nonlinear Optical Methods for Characterization of Molecular Structure and Surface Chemistry*. 2018; Vol. 61.
128. Velarde, L.; Wang, H.-F., Unified treatment and measurement of the spectral resolution and temporal effects in frequency-resolved sum-frequency generation vibrational spectroscopy (SFG-VS). *PCCP* **2013,** *15* (46), 19970-19984.
129. Stark, J., Observation of the Separation of Spectral Lines by an Electric Field. *Nature* **1913,** *92*, 401.
130. Boxer, S. G., Stark Realities. *The J. Phys. Chem. B* **2009,** *113* (10), 2972-2983.
131. Boxer, S. G.; Bublitz, G. U., Stark spectroscopy: Applications in Chemistry, Biology, and Materials Science. *Annu. Rev. Phys. Chem.* **1997,** *48*, 213–242.
132. Fried, S. D.; Boxer, S. G., Measuring electric fields and noncovalent interactions using the vibrational stark effect. *Acc. Chem. Res.* **2015,** *48* (4), 998-1006.
133. Andrews, S. S.; Boxer, S. G., Vibrational Stark Effects of Nitriles II. Physical Origins of Stark Effects from Experiment and Perturbation Models. *The J. Phys. Chem. A* **2002,** *106* (3), 469-477.
134. Park, E. S.; Boxer, S. G., Origins of the Sensitivity of Molecular Vibrations to Electric Fields: Carbonyl and Nitrosyl Stretches in Model Compounds and Proteins. *The J. Phys. Chem. B* **2002,** *106* (22), 5800-5806.
135. Andrews, S. S.; Boxer, S. G., A liquid nitrogen immersion cryostat for optical measurements. *Rev. Sci. Instrum.* **2000,** *71* (9), 3567.
136. Andrews, S., Boxer, S. G., Analysis of noise for rapid-scan and step-scan methods of FT-IR difference spectroscopy. *Applied Spectroscopy*. 2001, *55* (9), 161
137. Fried, S. D.; Bagchi, S.; Boxer, S. G., Extreme electric fields power catalysis in the active site of ketosteroid isomerase. *Science* **2014,** *346* (6216), 1510.
138. Fafarman, A. T.; Sigala, P. A.; Schwans, J. P.; Fenn, T. D.; Herschlag, D.; Boxer, S. G., Quantitative, directional measurement of electric field heterogeneity in the active site of ketosteroid isomerase. *Proc Natl Acad Sci U S A* **2012,** *109* (6), E299-308.
139. Ge, A.; Videla, P.; Lee, G. L.; Rudshteyn, B.; Song, J.; Kubiak, C. P.; Batista, V. S.; Lian, T., Interfacial Structure and Electric Field Probed by in situ Electrochemical Vibrational Stark Effect Spectroscopy and Computational Modeling. *The J. Phys. Chem. C* **2017**.
140. Clark, M. L.; Ge, A.; Videla, P. E.; Rudshteyn, B.; Miller, C. J.; Song, J.; Batista, V. S.; Lian, T.; Kubiak, C. P., CO_2 Reduction Catalysts on Gold Electrode Surfaces Influenced by Large Electric Fields. *J. Am. Chem. Soc.* **2018**.
141. Sorenson, S. A.; Patrow, J. G.; Dawlaty, J. M., Solvation Reaction Field at the Interface Measured by Vibrational Sum Frequency Generation Spectroscopy. *J. Am. Chem. Soc.* **2017,** *139* (6), 2369-2378.

142. Shi, H.; Cai, Z.; Patrow, J.; Zhao, B.; Wang, Y.; Wang, Y.; Benderskii, A.; Dawlaty, J.; Cronin, S. B., Monitoring Local Electric Fields at Electrode Surfaces Using Surface Enhanced Raman Scattering-Based Stark-Shift Spectroscopy during Hydrogen Evolution Reactions. *ACS Appl. Mater. Interfaces* **2018,** *10* (39), 33678-33683.
143. Ardo, S.; Sun, Y.; Staniszewski, A.; Castellano, F. N.; Meyer, G. J., Stark Effects after Excited-State Interfacial Electron Transfer at Sensitized TiO_2 Nanocrystallites. *J. Am. Chem. Soc.* **2010,** *132* (19), 6696-6709.
144. O'Donnell, R. M.; Ardo, S.; Meyer, G. J., Charge-Screening Kinetics at Sensitized TiO_2 Interfaces. *The J. Phys. Chem. Lett.* **2013,** *4* (17), 2817-2821.
145. O'Donnell, R. M.; Sampaio, R. N.; Barr, T. J.; Meyer, G. J., Electric Fields and Charge Screening in Dye Sensitized Mesoporous Nanocrystalline TiO_2 Thin Films. *The J. Phys. Chem. C* **2014,** *118* (30), 16976-16986.
146. Sampaio, R. N.; O'Donnell, R. M.; Barr, T. J.; Meyer, G. J., Electric Fields Control $TiO_2(e–) + I_3^–$ → Charge Recombination in Dye-Sensitized Solar Cells. *The J. Phys. Chem. Lett.* **2014,** *5* (18), 3265-3268.
147. Ward, C. L.; DiMarco, B. N.; O'Donnell, R. M.; Meyer, G. J., Dye Excited States Oriented Relative to TiO_2 Surface Electric Fields. *The J. Phys. Chem. C* **2018,** *122* (25) 13863-13871
148. Cappel, U. B.; Feldt, S. M.; Schöneboom, J.; Hagfeldt, A.; Boschloo, G., The Influence of Local Electric Fields on Photoinduced Absorption in Dye-Sensitized Solar Cells. *J. Am. Chem. Soc.* **2010,** *132* (26), 9096-9101.
149. Yang, W.; Pazoki, M.; Eriksson, A. I. K.; Hao, Y.; Boschloo, G., A key discovery at the TiO_2/dye/electrolyte interface: slow local charge compensation and a reversible electric field. *PCCP* **2015,** *17* (26), 16744-16751.
150. Pazoki, M.; Hagfeldt, A.; Boschloo, G., Stark effects in D35-sensitized mesoporous TiO_2: influence of dye coverage and electrolyte composition. *Electrochim. Acta* **2015,** *179*, 174-178.
151. Yang, W.; Hao, Y.; Vlachopoulos, N.; Eriksson, A. I. K.; Boschloo, G., Studies on the Interfacial Electric Field and Stark Effect at the TiO_2/Dye/Electrolyte Interface. *The J. Phys. Chem. C* **2016,** *120* (39), 22215-22224.
152. Yang, W.; Vlachopoulos, N.; Boschloo, G., Impact of Local Electric Fields on Charge-Transfer Processes at the TiO_2/Dye/Electrolyte Interface. *ACS Energy Letters* **2017,** *2* (1), 161-167.
153. Pazoki, M.; Jacobsson, T. J.; Kullgren, J.; Johansson, E. M. J.; Hagfeldt, A.; Boschloo, G.; Edvinsson, T., Photoinduced Stark Effects and Mechanism of Ion Displacement in Perovskite Solar Cell Materials. *ACS Nano* **2017,** *11* (3), 2823-2834.
154. Mani, T.; Grills, D. C.; Miller, J. R., Vibrational Stark Effects To Identify Ion Pairing and Determine Reduction Potentials in Electrolyte-Free Environments. *J. Am. Chem. Soc.* **2015,** *137* (3), 1136-1140.
155. Hack, J.; Grills, D. C.; Miller, J. R.; Mani, T., Identification of Ion-Pair Structures in Solution by Vibrational Stark Effects. *The J. Phys. Chem. B* **2016,** *120* (6), 1149-1157.
156. Silva, A. F., *Trends in interfacial electrochemistry / edited by A. Fernando Silva*. 2019.
157. Kötz, R.; Carlen, M., Principles and applications of electrochemical capacitors. *Electrochim. Acta* **2000,** *45* (15), 2483-2498.

Chapter 3:

Operando Sum-Frequency Generation Detection of Electrolyte Redox Products at Active Si Nanoparticle Li-Ion Battery Interfaces

This chapter contains the work published originally in "Operando Sum-Frequency Generation Detection of Electrolyte Redox Products at Active Si Nanoparticle Li-Ion Battery Interfaces" by Olson, J. Z.; Johansson, P. K.; Castner, D. G.; Schlenker, C. W., in Chemistry of Materials 2018, 30 (4), 1239-1248 10.1021/acs.chemmater.7b04087

3.1 Overview

For the first time on nanoparticle-based Si electrodes, we monitor electrochemical reduction products of ethylene carbonate (EC) and fluoroethylene carbonate (FEC) using interface-sensitive operando spectroelectrochemical sum-frequency generation (SFG). We observe SFG signatures that suggest carbon monoxide (CO) evolution on nano-Si proceeds at distinct lithiation potentials for different electrolyte solvents. EC reduction to yield CO occurs at potentials associated with silicon's most highly lithiated state (10mV), whereas FEC is reduced to CO at 10mV and 500mV (vs. Li/Li+). These results suggest that EC reduction is more sensitive than FEC to the lithiation state, validating previous computational predictions describing the reduction of both solvents. Our results suggest that low molecular weight oligomers that readily diffuse from the interface are formed during cycling, leading to SEI instability and an absence of SFG signal. Only upon prolonged EC reduction at 10mV do we observe SFG signatures for poly(EC), which we hypothesize are due to the formation of higher molecular weight chains that remain on the electrode surface during SFG acquisition. Potential-dependent FEC reduction to Li_2CO_3, LiF and CF-containing moieties evidently induces the predominant stabilizing effects to the interface, irrespective of the lithiation timescale. These results provide new, precise insight on the stability of high-capacity anodes.

3.2 Introduction

Silicon-based Li-ion battery anode materials are attractive as high-capacity replacements for conventional graphite anodes.[158-159] However, fundamental problems ranging from surface passivation to volume expansion continue to prevent widespread integration of silicon into modern technologies. Nanostructured silicon is a promising solution to mitigate volume expansion and pulverization associated with single crystal Si electrode cycling.[159-161] Currently, silicon nanoparticle-based anodes continue to suffer from drastic capacity fade that arises due to the evolution of electrochemically reactive species at the electrode/electrolyte interface. The integrity and composition of this solid-electrolyte interphase (SEI) layer, a mosaic structure induced by electro-reduction of a solution-phase electrolyte system on the solid-phase surface of an electrode, manifest in ionic conduction and electronic resistance. It is known that these traits are heavily influenced by the type and purity of the electrode material in contact with the electrolyte,[19,

[56, 162] as well as components of the composite architecture.[15, 54, 66, 163-164] Understanding the electrochemical evolution of molecular and polymeric species that form at the interface between a nanostructured Si electrode and a prospective electrolyte component is vital, as incompatible electrode/electrolyte combinations result in severe capacity fade. It is therefore extremely compelling to characterize the molecular processes and structural attributes that contribute to device failure in order to identify possible molecular design motifs to mitigate these degradation pathways.

Fluoroethylene carbonate (FEC), an electrolyte additive that appears to prolong the cycle life of Si anodes, has been considered as one possible solution to Si anode capacity fade.[60, 165] However, the underlying chemistry that governs FEC's mechanism of action remains unclear. Methods such as X-ray photoelectron spectroscopy (XPS), time-of-flight secondary ion mass spectrometry and neutron scattering have been used to help clarify the mechanisms responsible for the apparent stability enhancements that result from adding fluorinated co-solvents to electrolyte mixtures. These methods largely reveal SEI compositions comprising LiF and species with fewer oxygen-containing moieties in the SEI when compared with electrolyte solutions containing no FEC.[166-171]

Experimental vibrational characterization and computational analysis of the SEI formed from electrolyte solvent reduction suggests that polymerized structures (polycarbonates and conjugated networks)[172-177] and inorganic salts[10, 178-181] form as major byproducts on electrode surfaces. Polycarbonates can be generated by volatile nucleophiles[182] formed during solvent reduction, reacting with intact solvent molecules.[183] With EC as an electrolyte solvent, resulting polymers and oligomeric precursors are typically soluble in carbonate-based electrolytes and have a range of molecular weights.[56, 162, 173, 184-187] The solubility of inorganic salts is highly dependent on the structures that form; alkyl carbonate salts with longer chain lengths dissolve more readily in carbonate solvents,[188-189] and have been experimentally observed.[190-191] Additionally, inorganic salts may decompose on highly reducing surfaces rich in lithium content, propagating the polymerization of soluble moieties such as poly(EC).[192-193] The well-characterized solubility of such byproducts thus contributes to the capacity fade of a device, as the Faradaic processes to generate a robust SEI are 'lost' to dissolution in the solvent over time.

Assessing the electrochemical evolution of buried electrode interface species in Li-ion batteries is a notoriously challenging problem.[194-195] There are few techniques that can provide compositional information with interface sensitivity under the native operational conditions of the battery. Many of the air-sensitive species that develop at the native electrode cannot be readily observed using most *ex situ* surface analyses, while most bulk *operando* techniques lack the sensitivity to interrogate the true interface. However, sum-frequency generation (SFG) vibrational spectroelectrochemistry provides the ability to

characterize electrochemical processes at the molecular level by probing vibrational modes that are infrared (IR) *and* Raman active of molecules that are preferentially ordered at an electrode interface. This technique is thus particularly attractive for monitoring heterogeneous electrochemical reactions at electrode interfaces.

With regard to electrochemical energy storage devices, Ye and colleagues used SFG to infer the preferential orientation that carbonyl groups of carbonate solvent molecules adopt at cathode[72, 196] and carbon-based electrode[197] surfaces in the absence of electrochemical cycling. They also found cyclic carbonates at a higher concentration on the electrode surfaces even when used as a co-solvent with linear carbonates. The Dlott group employed SFG to monitor the spectroelectrochemical evolution of EC's electrochemical reduction on copper and gold surfaces,[178-179] consistent with the presence of lithium ethylene dicarbonate (LiEDC) as a structural component of the SEI, using its CH_2 mode at 1410 cm^{-1} as a vibrational marker. The Somorjai group observed similar effects on H-terminated, boron-doped single crystal silicon wafers while monitoring the reduction of DEC,[198] and in a separate study identified that the differences in homogeneity of SEIs formed on intrinsic single-crystal Si from fluorinated and nonfluorinated ethereal electrolyte solvents were the result of variations in molecular orientation before electrochemical cycling.[199]

The identity of gas molecules that are generated as a result of electrochemical bond-breaking in battery formulations are intimately linked to the mechanisms of SEI formation. Computational models of solvent reduction suggest that varying amounts of CO, CO_2, ethylene, and molecular hydrogen may be liberated as a result of the Faradaic processes that generate the SEI from carbonate-based electrolyte solvents.[193, 200] One factor controlling the composition of evolved gases from EC and FEC is the number of electrons initiating the reduction process. One-electron reduction is typically associated with CO_2 evolution, while two-electron reduction is associated with CO_2 and/or CO formation (interface chemistry appears to be a major factor determining these ratios).[183, 201-205] CO has been predicted to comprise a significant fraction of evolved gas molecules during FEC reduction on Si anodes during early stages of SEI formation.[206-207] Another important variable controlling the type and amount of gas evolved is the ratio of materials comprising the electrolyte formulation and supporting electrolyte salt, effects which have been studied by computational methods[208] and experimentally observed by bulk mass spectrometry methods.[174-175, 209-217] While the observed relative concentrations depend on measurement method, applied potential, electrolyte composition, and electrode surface chemistry, we associate liberation of small molecules such as CO with electrochemical carbonate solvent reduction reactions.

Here we measure the electrochemical reaction products formed at the interface between concentrated electrolyte solutions and Si nanoparticle-based electrode materials used in device-level composite

architectures by applying time- and potential-dependent electrochemical SFG. While gases such as CO_2, ethylene, and hydrogen have also been predicted theoretically and observed experimentally as major byproducts of electrolyte solvent reduction, their SFG activity is dependent on chemisorption that breaks their centrosymmetry (further described in Appendix A) and the vibrational modes[218-219] are located within energy regions that induced damage to the Si electrode in our setup. This issue also precluded our analysis of the SEI in the C-H stretching region as characterized by Somorjai and colleagues when monitoring the reduction of EC on Si-H (100) single crystal electrodes.[198] To overcome these challenges, we studied the vibrational modes in the spectral region of 1300 cm^{-1} – 2000 cm^{-1}. As summarized in Figure 1, using EC as the electrolyte solvent, we observe molecular signatures that are indicative of CO and poly(EC) at potentials associated with the highest lithiation state of Si. Using FEC as the solvent, CO is liberated even at the lowest lithiation state of Si, resulting in the preferential formation of LiF at low lithiation states; both LiF and Li_2CO_3 are formed at the highest state of lithiation. Our work highlights a strong correlation between molecular-level analyses at battery material interfaces and the device failure/optimization mechanisms of EC and FEC-based electrolytes. Additionally, we provide the first potential-dependent spectroscopic evidence to validate prior theoretical descriptions of solvent reduction at lithiated Si anodes. Using concentrated electrolytes containing EC as a solvent, our results reveal that polymeric species form that are known to dissolve in carbonate electrolytes, while inorganic salts and fluorinated alkyl chains appear to dominate the molecular composition of the SEI at the electrode surface upon the reduction of FEC.

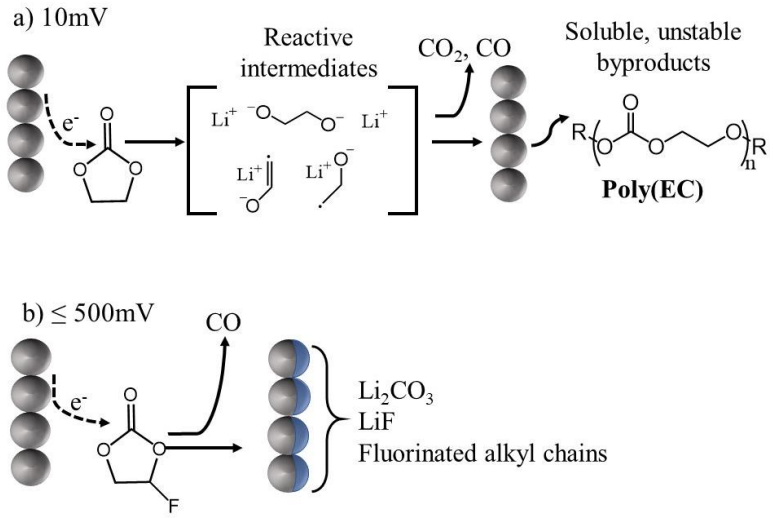

Figure 1. Summary of reactions describing electrolyte solvent reduction occurring on Si nanoparticles under different reducing conditions. a) With ethylene carbonate (EC) the measured byproducts of electrochemical reduction are soluble polymeric species. b) Fluoroethylene carbonate (FEC) reduces to inorganic salts and fluorinated alkyl chains that precipitate at the electrode surface.

3.3 Results and Discussion

To ensure that the concentrated electrolytes tested within this study were suitable for device applications, we tested both formulations in a composite coin cell architecture. Following the first charge/discharge cycle (Figure 3) with the 2M $LiClO_4$ / FEC electrolyte solution that we utilized for our *operando* SFG spectroelectrochemical measurements, we observed more robust capacity retention and higher overall device capacities compared to our control devices based on an EC electrolyte solvent. Our selection of $LiClO_4$ over $LiPF_6$ was motivated by our desire to avoid interference by competing reaction pathways that would preclude FEC from being the sole contributor to any fluorinated species contained within the SEI in our *operando* interface studies. It is important to note that, although devices cycling with $LiClO_4$ perform well, the composition of the SEI is not necessarily the same as it is for $LiPF_6$, a commonly used salt in battery research.[220-221] This is important because the PF_6 anion is known to electrolytically decompose and produce fluorinated components of the SEI.[170-171] Additionally, the concentration of FEC and lithium salt in the electrolyte can further influence cycling behavior.[174, 222] This is significant because spectroelectrochemical SFG studies commonly require dilute electrolyte solutions due to complications associated with experimental geometry. Specifically, the setup for acquiring SFG spectra commonly comprises IR and visible laser beams that traverse the bulk of the electrolyte solution before reaching the electrode surface from which SFG is produced. This can result in signal loss and spectral artifacts for undiluted electrolyte solutions due to significant absorption of the IR beam. In such cases, the co-solvents used to dilute the analyte molecule of interest are not typically used in lithium ion batteries, and can actually adversely influence the electrode material.[223] We overcame the above issues by performing SFG in internal reflection mode (Figure 2), so that we can use concentrated electrolyte solutions.

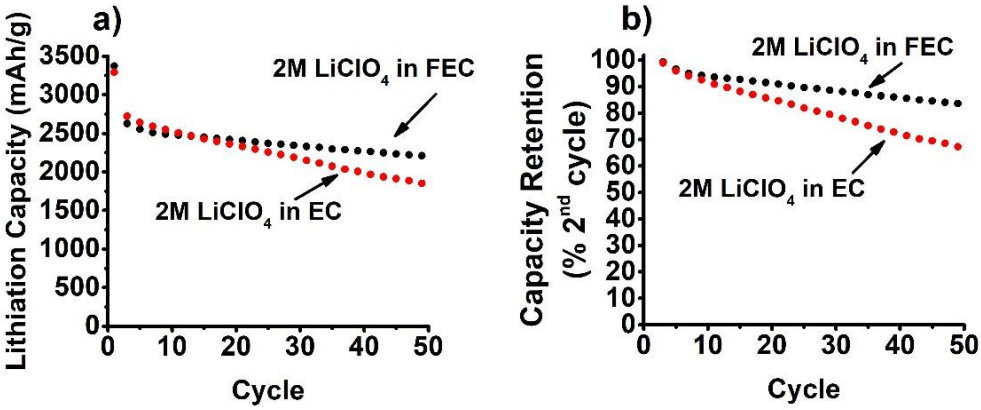

Figure 2. a) Lithiation capacity and b) capacity retention normalized to the second lithiation cycle for the FEC-based electrolyte with 2M $LiClO_4$ (black circles) and the EC-based electrolyte with 2M $LiClO_4$ (red circles).

In Figure 4 we compare the spectroelectrochemical SFG peaks of EC evolving in the 1300–1500 cm^{-1} and 1700-1950 cm^{-1} regions for the Si electrode cycled 5 times at 3mV/s (see Figure A.2 for associated voltammogram). The lack of signal in the 1300-1500 cm^{-1} (4a) range indicates that LiEDC and Li_2CO_3, some of the more commonly characterized insoluble inorganic SEI salts, have not precipitated with a preferred orientation at the surface. It is therefore possible that soluble species of longer chain length and oligomers have formed, contributing to device failure with the EC-based battery in Figure 3. The observed evolution of a non-resonant ($\chi_{NR}^{(2)}$) signal upon cycling throughout this work may be due to a change in the electronic structure of the Si electrode. Interference between $\chi_{NR}^{(2)}$ and a resonant SFG signal can yield asymmetric line shapes including dips as well as peaks,[224-227] which may lead to apparent shifts of the resonant peak positions. Fitting of the data captured after 5 cycles using Eqs. 1 and 2 revealed that the C=O vibration of the EC is centered at about 1840 cm^{-1}, resulting in a minimum followed by a peak. The fitting parameters for all experiments with EC are tabulated in Table 1.

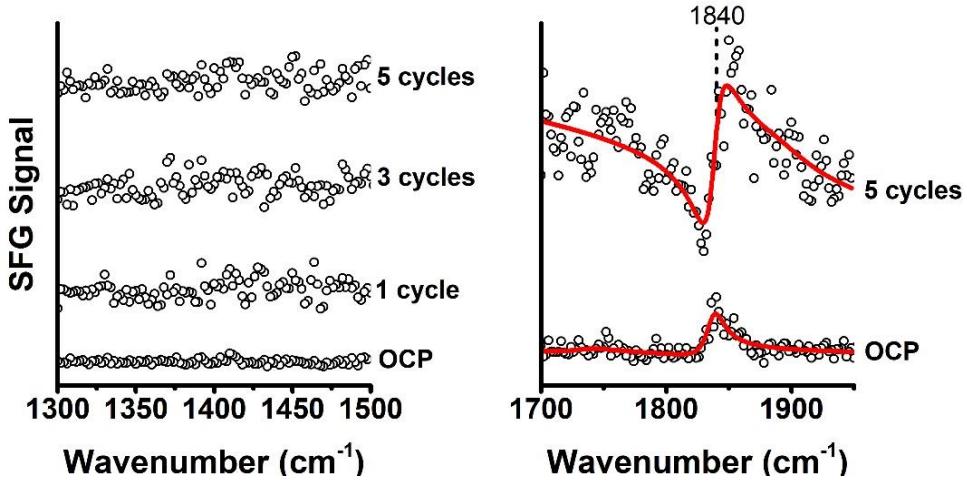

Figure 3. Cycle-dependent SFG profile developed with the use of EC as an electrolyte solvent. a) After 5 cycles, it is clear that no SFG activity for ordered lithium alkyl carbonates exists on the electrode surface; b) only a signal for EC at 1840 cm^{-1} is present.

To further study the evolution of chemical species as the electrode is lithiated at specific potentials for longer periods of time during the first cycle, we implement the potential scan/hold protocol that we described in the experimental section. As seen in Figure 5, substantial changes arise in the carbonyl stretching region of the SFG spectra depending on the applied potential, in comparison to voltammetric cycling without any potential hold steps. The prominent feature at 1940 cm^{-1} forms at the most reducing potential. Previously characterized interactions of CO on strongly reducing alkali metals (Li, Na, and K) in low-temperature, matrix-phase measurements manifest in IR absorption between 1920-1990 cm^{-1}, associated with the formation of $Li_x(CO)_y$ aggregates and/or oxycarbon anion ($C_xO_x^{2-}$) species due to the

instability of CO at the metal surface.[228-229] Furthermore, the vibrational spectra of CO on alkali metals supported on Si are rich in absorptivity at 1970 cm^{-1}.[230] Moreover, the vibrational frequency of CO is known to exhibit a redshift to 1930-1980 cm^{-1} on silicon clusters,[231] in contrast to its position at 2080 cm^{-1} on crystalline silicon.[232] Based on these observations of redshifted IR absorption for CO upon interacting with alkali metals and given the lithiated silicon cluster-like chemical motifs that are known to persist after electrochemical cycling and restructuring of the electrode interface,[96-97] we associate the new SFG signal that appears in the 1924-1975 cm^{-1} spectral range of our measurements with the liberation of carbon monoxide. As previously mentioned, it is likely that subsequent chemical reactions take place after CO is formed; computational studies have described the instability of neutral CO on Li at room temperature.[42] Thus, it is likely that the reducing potentials used in this study induce subsequent CO chemistry to form $Li_x(CO)_y$ aggregates and/or oxycarbon anion species, which contribute to the SFG signal that we observe. While isotopic labeling that would be required to determine the precise coordination environment and chemical identity of these CO-associated species[228] is beyond the scope of this study, the vibrational peaks in the 1924-1975 cm^{-1} spectral range are consistent with the presence of a carbon monoxide-associated species in our samples.

The peak appearing at 1758 cm^{-1} (Figure 5b) is consistent with the generation of high molecular weight, soluble poly(EC) species observed by Shi and colleagues.[56] Evidently, the timescales of poly(EC)'s solvation and diffusion from the electrode surface therefore appear to be longer than the duration of our experiment. Similar potential-dependent results were previously observed on Si anodes, when soluble byproducts of carbonate-based electrolyte transesterification[233] were measured on the electrode surface.[57] Nevertheless, the established solubility of poly(EC) in carbonate electrolytes implies that at least one failure mechanism with a concentrated EC-based electrolyte proceeds via poly(EC) buildup and eventual dissolution. Polymerization of EC at the electrode surface has also been reported through an unstable, adsorbed dianion of carbon monoxide (CO^{2-}) formed from an electrochemically reduced molecule of the carbonate solvent at the electrode surface as an alternative reaction pathway to those described above.[234-236]

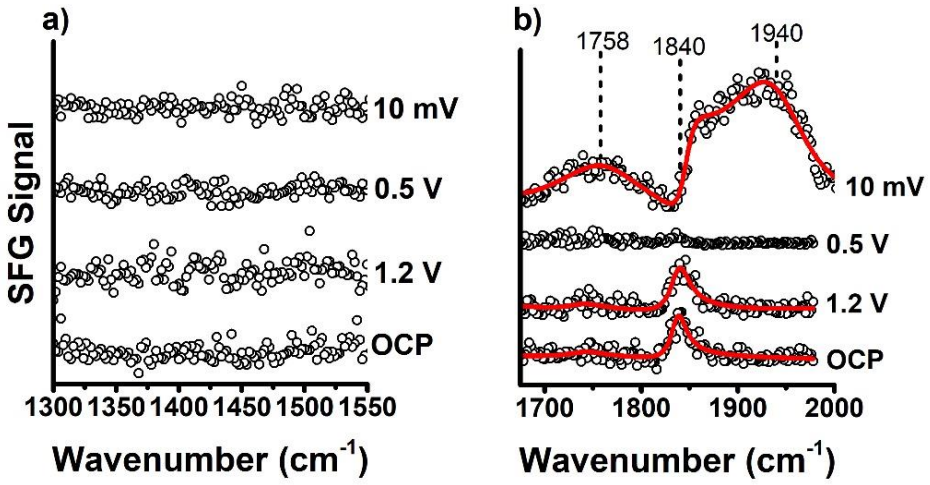

Figure 4. SFG signals as a function of potential used in scan/hold protocol, captured at OCP following electrochemical cycling. a) Limited spectral evolution is seen regardless of potential. b) At a potential of 0.5 V, the interfacial signature for intact EC (1840 cm^{-1}) has clearly decreased. At 10 mV, a spectrum indicative of poly(EC) at 1758 cm^{-1} and carbon monoxide at 1940 cm^{-1} has developed.

Assign.	(cm^{-1})*	**OCP**	**Cycle 5**[a]	**1.2V**[b]	**0.01 V**[b]
CO[c]	ω_k	-	-	-	1940
	Γ_k				60.7
	A_K				1.19
EC (C=O)	ω_k	1837	1840	1838	1840
	Γ_k	9.0	10.2	12.2	11.8
	A_K	0.11	-0.19	0.12	-0.15
Poly(EC) (C=O)	ω_k	-	-	-	1758
	Γ_k				49
	A_K				0.42

[a] voltammetric cycling protocol [b] scan/hold protocol *unit for ω_k and Γ_k [c] as described in refs. 83-86

Table 1: parameters used to fit SFG spectra in Eqs. A.1.1 & A.1.2, using EC as an electrolyte solvent

While a larger signal for the peak that we associate with CO exists, no new peaks appear in the 1300-1500 cm^{-1} region at longer lithiation timescales. These results indicate that the highly reducing electrode surface associated with lithiating Si at longer timescales provides an environment that promotes poly(EC) formation at the electrode interface.[177, 192-193] Starting at 0.5 V, the absence of a C=O mode for intact EC (as part of the cyclic structure) and absence of poly(EC) suggests the formation of low molecular weight oligomers,[186] as the spectroscopic characterization of electrochemically-produced poly(EC) observed by Shi and colleagues has a high molecular weight.[56] Voltage-dependent formation of high molecular-weight polycarbonates is known to be obtainable at potentials close to lithiation of the electrode,[237] which would be consistent with the appearance of poly(EC) at 10 mV in our measurements.

Adapting the same set of voltammetric cycling tests using FEC as an electrolyte solvent, we recover several unique differences in electrochemical and vibrational signatures when compared to EC. Firstly, the voltammogram (Figure A.3) exhibits greater Faradaic behavior beginning at potentials near 1.2 V. Secondly, the cycle-dependent SFG profiles (Figure 6) differ from the EC-derived SEI in the 1300-1500 cm^{-1} region. The SFG-active vibrational modes spanning the 1420 – 1500 cm^{-1} region that grow in after each cycle are indicative of Li_2CO_3,[59, 175, 238] and include the asymmetric stretches of the C-O bond.[239-241] As in the case of the EC based electrolyte, the absence of a peak at 1410 cm^{-1} indicates a lack of a ordered species with SFG active CH_2 scissoring modes, such as LiEDC. Also similar to EC, the C=O stretch vibration at about 1878 cm^{-1} interferes with $\chi_{NR}^{(2)}$, creating a line shape with a minimum followed by a peak, with a small shoulder in this case near 1924 cm^{-1} that we ascribe to the early formation of CO.

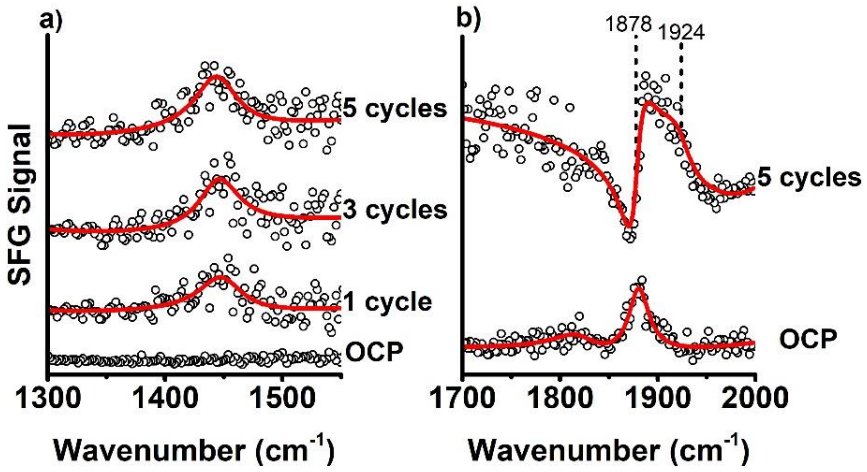

Figure 5. SFG characterization of the SEI generated with voltammetric cycling at the Si/FEC junction, collected at OCP. In addition to the FEC carbonyl stretch at 1878 cm^{-1} spectral signatures emerge post-cycling at 1440-1450 cm^{-1} associated with Li_2CO_3 (a) and at about 1924 cm^{-1} for CO (b).

As seen in Figure 7, scan/hold conditions result in substantial changes to the electrode interface, beginning already at 0.5 V for FEC, at which CO is readily formed. This result appears to be consistent with computational efforts that have analyzed the reactivity of carbonate solvents, which suggest that the decomposition pathways for FEC are independent of the degree of electrode lithiation.[207, 242] Conversely, the voltage-dependent EC reduction mechanism appears to be more sensitive to the lithiation state of the electrode, [201, 243-244] which may explain why no CO is observed at the electrode surface after the 0.5 V scan/hold step; other gases may be preferentially evolving at less reducing potentials with EC as the electrolyte solvent. More importantly, the polycarbonate signals that we observed for EC are absent at all reducing potentials for FEC. Additionally, the 1300-1500 cm^{-1} region indicates the SEI components remain intact at long lithiation times. This improved SEI fidelity is reflected in the signal magnitude after the

scan/hold protocol being approximately the same as in post-cycle 1-5 (red trace) of Figure 6a. Table 2 lists peak positions and their corresponding fitting parameters.

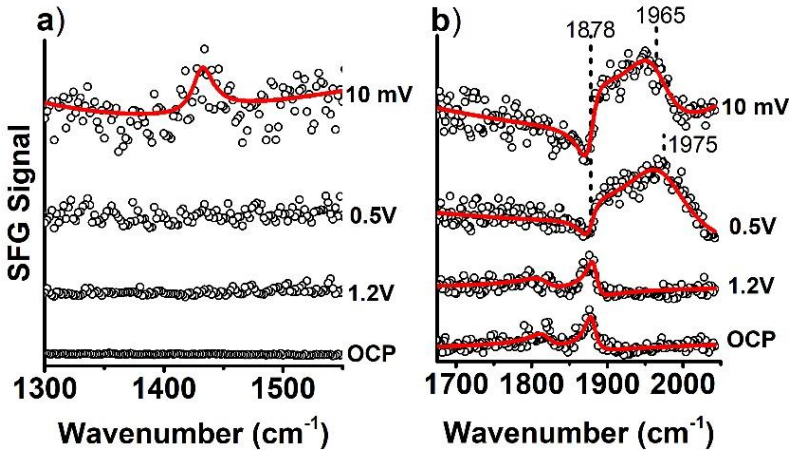

Figure 6. First cycle analysis of the alkyl dicarbonate a) and carbonyl b) region using FEC as an electrolyte solvent, captured at OCP. After a scan/hold at 0.5 V, it is clear the electrolysis of FEC initially at the Si electrode interface has begun, resulting in CO-associated species detectable at roughly 1975 cm^{-1}. After scan/hold at 10 mV, a peak at 1431 cm^{-1} also emerged, indicative of Li_2CO_3.

Assign.	**(cm^{-1})***	**OCP**	**Cycle 1[a]**	**Cycle 3[a]**	**Cycle 5[a]**	**1.2V[b]**	**0.5V[b]**	**0.01V[b]**
Li_2CO_3 (C-O asymm.)	ω_k	-	1449	1445	1445	-	-	1431
	Γ_k		22.8	21.1	22.3			10.6
	A_k		0.23	0.22	0.23			0.12
CO[c]	ω_k	-	-	-	1924	-	1975	1965
	Γ_k				18.1		51.4	36.8
	A_k				0.03		0.56	0.23
FEC (C=O)	ω_k	1880	-	-	1878	1883	1878	1878
	Γ_k	12.6			10.0	8.2	11.1	12.6
	A_k	0.07			-0.11	0.08	-0.06	-0.09

[a] voltammetric cycling protocol [b] scan/hold protocol *unit for ω_k and Γ_k [c] as described in refs. 83-86

Table 2: parameters used for fitting SFG spectra in Eqs. A.1.1 & A.1.2, using FEC as an electrolyte solvent

The presence of LiF as part of the SEI is commonly regarded as a stabilizing contributor to capacity retention in Si anodes.[245-246] In Figure 8 we present the F1s XPS spectrum for the formation of LiF as a function of applied potential. Under potential scan/hold experiments to 0.5 V and 10 mV, the LiF peak dominates the spectrum. The shoulder at less reducing potentials (starting at ~687.5 eV) correlates with binding energies found in other works associated with the presence of C-F bonds from FEC reduction, as the presence of fluorine (from FEC) has been postulated to result in the incorporation of C-F bonds within

the SEI structure in the form of fluorinated alkyl chains of varied length, terminated with carbonate or carboxylate groups that coordinate lithium ions.[59, 168, 177, 247-248] The apparent shift to lower binding energy of the C-F bond at 10 mV is likely due to the degree of fluorination of the carbon network,[249] while any broadening of the peak is likely reflective of an ensemble of C-F bond types; those with more covalent character are at higher binding energies, while those with more ionic character are at lower binding energies.[250-251]

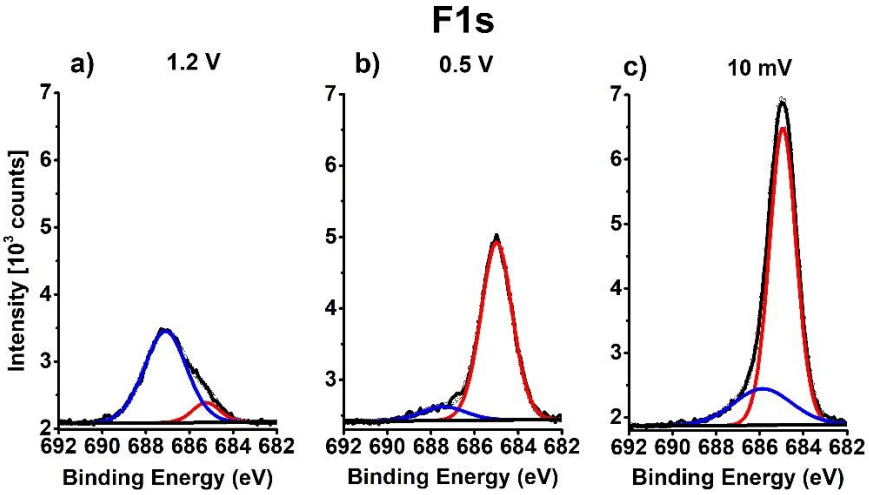

Figure 7. F 1s XPS profile of the potential-dependent SEI formed on Si nanoparticle electrodes using FEC as the electrolyte solvent. The C-F peak that appears in the F 1s spectrum between 686-687.5 eV suggests the presence of fluorinated organic species form under mildly reducing potentials (a), while the signal at 685eV indicates the formation of LiF dominates under more harshly reducing potentials (b & c).

3.4 Conclusion:

Using vibrational sum frequency generation (SFG) spectroscopy, we monitor the interfacial electrochemical products generated between silicon nanoparticle electrodes and concentrated organic carbonate-based electrolytes. We demonstrate that the early electrochemical reduction cycles of ethylene carbonate (EC) on lithiated Si nanoparticle electrodes precipitate few if any stable SEI components that are observable by SFG. We also show that the generation of CO is sensitive to the degree of lithiation. These findings suggest that EC reduction liberates oligomeric products that are soluble in the electrolyte solution, some of which appear to polymerize at higher charge densities to form poly(EC), another soluble species. Substituting FEC for EC stabilizes the Si electrode by concomitantly generating LiF, Li_2CO_3 and fluorinated alkyl chains that appear to suppress the formation of soluble moieties. It appears that carbon monoxide forms as a byproduct also of FEC reduction, but at less-reducing potentials than required for EC. Although we have observed chemical species over a large spectral window, there may exist additional components that lack the properties necessary to be SFG active or that appear in other spectral regions. Nevertheless,

our results provide vital new insights into the electrochemical reduction of concentrated organic carbonate-based electrolyte systems at alloyed semiconductor nanoparticle electrode interfaces. These results also validate computational descriptions of voltage-dependent reactions that these electrochemical solvents can undergo at the electrode/electrolyte junction. As a forward-looking application of these results, tailoring the active material interface with oxygen-free carbonaceous networks before electrochemical cycling may stabilize the performance of high-capacity, next-generation electrode materials.

3.5 Appendix A:

Experimental methods and supporting information for chapter 3

3.6 Acknowledgements:

This material is based in part upon work supported by the State of Washington through the University of Washington Clean Energy Institute and via funding from the Washington Research Foundation. Part of this work was conducted at the Molecular Analysis Facility, a National Nanotechnology Coordinated Infrastructure site at the University of Washington which is supported in part by the National Science Foundation (grant ECC-1542101), the University of Washington, the Molecular Engineering & Sciences Institute, the Clean Energy Institute, and the National Institutes of Health. We acknowledge Gerry Hammer for acquisition of XPS data.

3.7 References:

10. Aurbach, D.; Gofer, Y.; Ben-Zion, M.; Aped, P., The behaviour of lithium electrodes in propylene and ethylene carbonate: Te major factors that influence Li cycling efficiency. *J. Electroanal. Chem.* **1992,** *339* (1), 451-471.
15. Zheng, H.; Yang, R.; Liu, G.; Song, X.; Battaglia, V. S., Cooperation between Active Material, Polymeric Binder and Conductive Carbon Additive in Lithium Ion Battery Cathode. *The J. Phys. Chem. C* **2012,** *116* (7), 4875-4882.
19. Peled, E.; Golodnitsky, D.; Ulus, A.; Yufit, V., Effect of carbon substrate on SEI composition and morphology. *Electrochim. Acta* **2004,** *50* (2–3), 391-395.
54. Nguyen, C. C.; Yoon, T.; Seo, D. M.; Guduru, P.; Lucht, B. L., Systematic Investigation of Binders for Silicon Anodes: Interactions of Binder with Silicon Particles and Electrolytes and Effects of Binders on Solid Electrolyte Interphase Formation. *ACS Appl. Mater. Interfaces* **2016,** *8* (19), 12211-12220.
56. Shi, F.; Zhao, H.; Liu, G.; Ross, P. N.; Somorjai, G. A.; Komvopoulos, K., Identification of Diethyl 2,5-Dioxahexane Dicarboxylate and Polyethylene Carbonate as Decomposition Products of Ethylene Carbonate Based Electrolytes by Fourier Transform Infrared Spectroscopy. *The J. Phys. Chem. C* **2014,** *118* (27), 14732-14738.
57. Shi, F.; Ross, P. N.; Somorjai, G. A.; Komvopoulos, K., The Chemistry of Electrolyte Reduction on Silicon Electrodes Revealed by in Situ ATR-FTIR Spectroscopy. *The J. Phys. Chem. C* **2017,** *121* (27), 14476-14483.
59. Jo, H.; Kim, J.; Nguyen, D.-T.; Kang, K. K.; Jeon, D.-M.; Yang, A. R.; Song, S.-W., Stabilizing the Solid Electrolyte Interphase Layer and Cycling Performance of Silicon–Graphite Battery

Anode by Using a Binary Additive of Fluorinated Carbonates. *The J. Phys. Chem. C* **2016,** *120* (39), 22466-22475.
60. Lin, Y.-M.; Klavetter, K. C.; Abel, P. R.; Davy, N. C.; Snider, J. L.; Heller, A.; Mullins, C. B., High performance silicon nanoparticle anode in fluoroethylene carbonate-based electrolyte for Li-ion batteries. *Chem. Commun.* **2012,** *48* (58), 7268-7270.
66. Jones, E. M. C.; Çapraz, Ö. Ö.; White, S. R.; Sottos, N. R., Reversible and Irreversible Deformation Mechanisms of Composite Graphite Electrodes in Lithium-Ion Batteries. *J. Electrochem. Soc.* **2016,** *163* (9), A1965-A1974.
72. Yu, L.; Liu, H.; Wang, Y.; Kuwata, N.; Osawa, M.; Kawamura, J.; Ye, S., Preferential Adsorption of Solvents on the Cathode Surface of Lithium Ion Batteries. *Angew. Chem. Int. Ed.* **2013,** *52* (22), 5753-5756.
96. Key, B.; Morcrette, M.; Tarascon, J.-M.; Grey, C. P., Pair Distribution Function Analysis and Solid State NMR Studies of Silicon Electrodes for Lithium Ion Batteries: Understanding the (De)lithiation Mechanisms. *J. Am. Chem. Soc.* **2011,** *133* (3), 503-512.
97. Ogata, K.; Salager, E.; Kerr, C. J.; Fraser, A. E.; Ducati, C.; Morris, A. J.; Hofmann, S.; Grey, C. P., Revealing lithium–silicide phase transformations in nano-structured silicon-based lithium ion batteries via in situ NMR spectroscopy. *Nat. Comm.* **2014,** *5*, 3217.
158. Li, F.-S.; Wu, Y.-S.; Chou, J.; Wu, N.-L., A dimensionally stable and fast-discharging graphite-silicon composite Li-ion battery anode enabled by electrostatically self-assembled multifunctional polymer-blend coating. *Chem. Commun.* **2015,** *51* (40), 8429-8431.
159. Magasinski, A.; Dixon, P.; Hertzberg, B.; Kvit, A.; Ayala, J.; Yushin, G., High-performance lithium-ion anodes using a hierarchical bottom-up approach. *Nat. Mater.* **2010,** *9* (4), 353-358.
160. Chan, C. K.; Peng, H.; Liu, G.; McIlwrath, K.; Zhang, X. F.; Huggins, R. A.; Cui, Y., High-performance lithium battery anodes using silicon nanowires. *Nat. Nano.* **2008,** *3* (1), 31-35.
161. Wada, T.; Ichitsubo, T.; Yubuta, K.; Segawa, H.; Yoshida, H.; Kato, H., Bulk-Nanoporous-Silicon Negative Electrode with Extremely High Cyclability for Lithium-Ion Batteries Prepared Using a Top-Down Process. *Nano Lett.* **2014,** *14* (8), 4505-4510.
162. Tavassol, H.; Buthker, J. W.; Ferguson, G. A.; Curtiss, L. A.; Gewirth, A. A., Solvent Oligomerization during SEI Formation on Model Systems for Li-Ion Battery Anodes. *J. Electrochem. Soc.* **2012,** *159* (6), A730-A738.
163. Zheng, J.; Xiao, J.; Xu, W.; Chen, X.; Gu, M.; Li, X.; Zhang, J.-G., Surface and structural stabilities of carbon additives in high voltage lithium ion batteries. *J. Power Sources* **2013,** *227*, 211-217.
164. Jeschull, F.; Lindgren, F.; Lacey, M. J.; Björefors, F.; Edström, K.; Brandell, D., Influence of inactive electrode components on degradation phenomena in nano-Si electrodes for Li-ion batteries. *J. Power Sources* **2016,** *325*, 513-524.
165. Choi, N.-S.; Yew, K. H.; Lee, K. Y.; Sung, M.; Kim, H.; Kim, S.-S., Effect of fluoroethylene carbonate additive on interfacial properties of silicon thin-film electrode. *J. Power Sources* **2006,** *161* (2), 1254-1259.
166. Fears, T. M.; Doucet, M.; Browning, J. F.; Baldwin, J. K. S.; Winiarz, J. G.; Kaiser, H.; Taub, H.; Sacci, R. L.; Veith, G. M., Evaluating the solid electrolyte interphase formed on silicon electrodes: a comparison of ex situ X-ray photoelectron spectroscopy and in situ neutron reflectometry. *PCCP* **2016,** *18* (20), 13927-13940.
167. Schroder, K.; Alvarado, J.; Yersak, T. A.; Li, J.; Dudney, N.; Webb, L. J.; Meng, Y. S.; Stevenson, K. J., The Effect of Fluoroethylene Carbonate as an Additive on the Solid Electrolyte Interphase on Silicon Lithium-Ion Electrodes. *Chem. Mater.* **2015,** *27* (16), 5531-5542.
168. Xu, C.; Lindgren, F.; Philippe, B.; Gorgoi, M.; Björefors, F.; Edström, K.; Gustafsson, T., Improved Performance of the Silicon Anode for Li-Ion Batteries: Understanding the Surface Modification Mechanism of Fluoroethylene Carbonate as an Effective Electrolyte Additive. *Chem. Mater.* **2015,** *27* (7), 2591-2599.

169. Markevich, E.; Fridman, K.; Sharabi, R.; Elazari, R.; Salitra, G.; Gottlieb, H. E.; Gershinsky, G.; Garsuch, A.; Semrau, G.; Schmidt, M. A.; Aurbach, D., Amorphous Columnar Silicon Anodes for Advanced High Voltage Lithium Ion Full Cells: Dominant Factors Governing Cycling Performance. *J. Electrochem. Soc.* **2013,** *160* (10), A1824-A1833.
170. Ortiz, D.; Jiménez Gordon, I.; Baltaze, J.-P.; Hernandez-Alba, O.; Legand, S.; Dauvois, V.; Si Larbi, G.; Schmidhammer, U.; Marignier, J.-L.; Martin, J.-F.; Belloni, J.; Mostafavi, M.; Le Caër, S., Electrolytes Ageing in Lithium-ion Batteries: A Mechanistic Study from Picosecond to Long Timescales. *ChemSusChem* **2015,** *8* (21), 3605-3616.
171. Lux, S. F.; Chevalier, J.; Lucas, I. T.; Kostecki, R., HF Formation in $LiPF_6$-Based Organic Carbonate Electrolytes. *ECS Electrochemistry Letters* **2013,** *2* (12), A121-A123.
172. Etacheri, V.; Haik, O.; Goffer, Y.; Roberts, G. A.; Stefan, I. C.; Fasching, R.; Aurbach, D., Effect of Fluoroethylene Carbonate (FEC) on the Performance and Surface Chemistry of Si-Nanowire Li-Ion Battery Anodes. *Langmuir* **2012,** *28* (1), 965-976.
173. Sloop, S. E.; Kerr, J. B.; Kinoshita, K., The role of Li-ion battery electrolyte reactivity in performance decline and self-discharge. *J. Power Sources* **2003,** *119*, 330-337.
174. Jung, R.; Metzger, M.; Haering, D.; Solchenbach, S.; Marino, C.; Tsiouvaras, N.; Stinner, C.; Gasteiger, H. A., Consumption of Fluoroethylene Carbonate (FEC) on Si-C Composite Electrodes for Li-Ion Batteries. *J. Electrochem. Soc.* **2016,** *163* (8), A1705-A1716.
175. Michan, A. L.; Parimalam, B. S.; Leskes, M.; Kerber, R. N.; Yoon, T.; Grey, C. P.; Lucht, B. L., Fluoroethylene Carbonate and Vinylene Carbonate Reduction: Understanding Lithium-Ion Battery Electrolyte Additives and Solid Electrolyte Interphase Formation. *Chem. Mater.* **2016,** *28* (22) 8149-8159.
176. Nie, M.; Demeaux, J.; Young, B. T.; Hesket, D. R.; Chen, Y.; Bose, A.; Woicik, J. C.; Lucht, B. L., Effect of Vinylene Carbonate and Fluoroethylene Carbonate on SEI Formation on Graphitic Anodes in Li-Ion Batteries. *J. Electrochem. Soc.* **2015,** *162* (13), A7008-A7014.
177. Young, B. T.; Heskett, D. R.; Nguyen, C. C.; Nie, M.; Woicik, J. C.; Lucht, B. L., Hard X-ray Photoelectron Spectroscopy (HAXPES) Investigation of the Silicon Solid Electrolyte Interphase (SEI) in Lithium-Ion Batteries. *ACS Appl. Mater. Interfaces* **2015,** *7* (36), 20004-20011.
178. Mukherjee, P.; Lagutchev, A.; Dlott, D. D., In Situ Probing of Solid-Electrolyte Interfaces with Nonlinear Coherent Vibrational Spectroscopy. *J. Electrochem. Soc.* **2012,** *159* (3), A244-A252.
179. Nicolau, B. G.; García-Rey, N.; Dryzhakov, B.; Dlott, D. D., Interfacial Processes of a Model Lithium Ion Battery Anode Observed, in Situ, with Vibrational Sum-Frequency Generation Spectroscopy. *The J. Phys. Chem. C* **2015,** *119* (19), 10227-10233.
180. Guorong V. Zhuang, K. X., Hui Yang, T. Richard Jow, Philip N. Ross, Lithium Ethylene Dicarbonate Identified as the Primary Product of Chemical and Electrochemical Reduction of EC in 1.2 M $LiPF_6$/EC:EMC Electrolyte. *J. Phys. Chem. B* **2005,** (109), 17567-17573.
181. Xu, K.; Zhuang, G. V.; Allen, J. L.; Lee, U.; Zhang, S. S.; Ross, P. N.; Jow, T. R., Syntheses and Characterization of Lithium Alkyl Mono- and Dicarbonates as Components of Surface Films in Li-Ion Batteries. *The J. Phys. Chem. B* **2006,** *110* (15), 7708-7719.
182. Shkrob, I. A.; Zhu, Y.; Marin, T. W.; Abraham, D., Reduction of Carbonate Electrolytes and the Formation of Solid-Electrolyte Interface (SEI) in Lithium-Ion Batteries. 1. Spectroscopic Observations of Radical Intermediates Generated in One-Electron Reduction of Carbonates. *The J. Phys. Chem. C* **2013,** *117* (38), 19255-19269.
183. Leung, K., Two-electron reduction of ethylene carbonate: A quantum chemistry re-examination of mechanisms. *Chem. Phys. Lett.* **2013,** *568–569*, 1-8.
184. Gachot, G.; Ribière, P.; Mathiron, D.; Grugeon, S.; Armand, M.; Leriche, J.-B.; Pilard, S.; Laruelle, S., Gas Chromatography/Mass Spectrometry As a Suitable Tool for the Li-Ion Battery Electrolyte Degradation Mechanisms Study. *Anal. Chem.* **2011,** *83* (2), 478-485.

185. Gachot, G.; Grugeon, S.; Armand, M.; Pilard, S.; Guenot, P.; Tarascon, J.-M.; Laruelle, S., Deciphering the multi-step degradation mechanisms of carbonate-based electrolyte in Li batteries. *J. Power Sources* **2008,** *178* (1), 409-421.
186. Gourdin, G.; Collins, J.; Zheng, D.; Foster, M.; Qu, D., Spectroscopic Compositional Analysis of Electrolyte during Initial SEI Layer Formation. *The J. Phys. Chem. C* **2014,** *118* (31), 17383-17394.
187. Shkrob, I. A.; Zhu, Y.; Marin, T. W.; Abraham, D., Reduction of Carbonate Electrolytes and the Formation of Solid-Electrolyte Interface (SEI) in Lithium-Ion Batteries. 2. Radiolytically Induced Polymerization of Ethylene Carbonate. *The J. Phys. Chem. C* **2013,** *117* (38), 19270-19279.
188. Wang, Y.; Nakamura, S.; Ue, M.; Balbuena, P. B., Theoretical Studies To Understand Surface Chemistry on Carbon Anodes for Lithium-Ion Batteries: Reduction Mechanisms of Ethylene Carbonate. *J. Am. Chem. Soc.* **2001,** *123* (47), 11708-11718.
189. Tasaki, K.; Goldberg, A.; Lian, J.-J.; Walker, M.; Timmons, A.; Harris, S. J., Solubility of Lithium Salts Formed on the Lithium-Ion Battery Negative Electrode Surface in Organic Solvents. *J. Electrochem. Soc.* **2009,** *156* (12), A1019-A1027.
190. Michan, A. L.; Leskes, M.; Grey, C. P., Voltage Dependent Solid Electrolyte Interphase Formation in Silicon Electrodes: Monitoring the Formation of Organic Decomposition Products. *Chem. Mater.* **2016,** *28* (1), 385-398.
191. Naji, A.; Ghanbaja, J.; Humbert, B.; Willmann, P.; Billaud, D., Electroreduction of graphite in $LiClO_4$-ethylene carbonate electrolyte. Characterization of the passivating layer by transmission electron microscopy and Fourier-transform infrared spectroscopy. *J. Power Sources* **1996,** *63* (1), 33-39.
192. Leung, K.; Soto, F.; Hankins, K.; Balbuena, P. B.; Harrison, K. L., Stability of Solid Electrolyte Interphase Components on Lithium Metal and Reactive Anode Material Surfaces. *The J. Phys. Chem. C* **2016,** *120* (12), 6302-6313.
193. Soto, F. A.; Ma, Y.; Martinez de la Hoz, J. M.; Seminario, J. M.; Balbuena, P. B., Formation and Growth Mechanisms of Solid-Electrolyte Interphase Layers in Rechargeable Batteries. *Chem. Mater.* **2015,** *27* (23), 7990-8000.
194. Schwager, P.; Bülter, H.; Plettenberg, I.; Wittstock, G., Review of Local In Situ Probing Techniques for the Interfaces of Lithium-Ion and Lithium–Oxygen Batteries. *Energy Technology* **2016**.
195. Yang, Y.; Liu, X.; Dai, Z.; Yuan, F.; Bando, Y.; Golberg, D.; Wang, X., In Situ Electrochemistry of Rechargeable Battery Materials: Status Report and Perspectives. *Adv. Mater.* **2017,** *29* (31), 1606922.
196. Liu, H.; Tong, Y.; Kuwata, N.; Osawa, M.; Kawamura, J.; Ye, S., Adsorption of Propylene Carbonate (PC) on the $LiCoO_2$ Surface Investigated by Nonlinear Vibrational Spectroscopy. *The J. Phys. Chem. C* **2009,** *113* (48), 20531-20534.
197. Peng, Q.; Liu, H.; Ye, S., Adsorption of organic carbonate solvents on a carbon surface probed by sum frequency generation (SFG) vibrational spectroscopy. *J. Electroanal. Chem.* **2016**, 800
198. Horowitz, Y.; Han, H.-L.; Ross, P. N.; Somorjai, G. A., In Situ Potentiodynamic Analysis of the Electrolyte/Silicon Electrodes Interface Reactions - A Sum Frequency Generation Vibrational Spectroscopy Study. *J. Am. Chem. Soc.* **2016**.
199. Horowitz, Y.; Han, H.-L.; Ralston, W. T.; de Araujo, J. R.; Kreidler, E.; Brooks, C.; Somorjai, G. A., Fluorinated End-Groups in Electrolytes Induce Ordered Electrolyte/Anode Interface Even at Open-Circuit Potential as Revealed by Sum Frequency Generation Vibrational Spectroscopy. *Adv. Energy Mater.* **2017**, 1602060.
200. Tasaki, K., Solvent Decompositions and Physical Properties of Decomposition Compounds in Li-Ion Battery Electrolytes Studied by DFT Calculations and Molecular Dynamics Simulations. *The J. Phys. Chem. B* **2005,** *109* (7), 2920-2933.

201. Ma, Y.; Balbuena, P. B., DFT Study of Reduction Mechanisms of Ethylene Carbonate and Fluoroethylene Carbonate on Li^+-Adsorbed Si Clusters. *J. Electrochem. Soc.* **2014,** *161* (8), E3097-E3109.
202. Leung, K.; Tenney, C. M., Toward First Principles Prediction of Voltage Dependences of Electrolyte/Electrolyte Interfacial Processes in Lithium Ion Batteries. *The J. Phys. Chem. C* **2013,** *117* (46), 24224-24235.
203. Leung, K.; Budzien, J. L., Ab initio molecular dynamics simulations of the initial stages of solid-electrolyte interphase formation on lithium ion battery graphitic anodes. *PCCP* **2010,** *12* (25), 6583-6586.
204. An, S. J.; Li, J.; Daniel, C.; Mohanty, D.; Nagpure, S.; Wood Iii, D. L., The state of understanding of the lithium-ion-battery graphite solid electrolyte interphase (SEI) and its relationship to formation cycling. *Carbon* **2016,** *105*, 52-76.
205. Perez-Beltran, S.; Ramírez-Caballero, G. E.; Balbuena, P. B., Ethylene Carbonate Reduction on Lithiated Surfaces of Hydroxylated Amorphous Silicon Dioxide. *J. Electrochem. Soc.* **2016,** *163* (10), A2197-A2202.
206. Leung, K.; Rempe, S. B.; Foster, M. E.; Ma, Y.; Martinez del la Hoz, J. M.; Sai, N.; Balbuena, P. B., Modeling Electrochemical Decomposition of Fluoroethylene Carbonate on Silicon Anode Surfaces in Lithium Ion Batteries. *J. Electrochem. Soc.* **2014,** *161* (3), A213-A221.
207. Okuno, Y.; Ushirogata, K.; Sodeyama, K.; Tateyama, Y., Decomposition of the fluoroethylene carbonate additive and the glue effect of lithium fluoride products for the solid electrolyte interphase: an ab initio study. *PCCP* **2016,** *18* (12), 8643-8653.
208. Martinez de la Hoz, J. M.; Soto, F. A.; Balbuena, P. B., Effect of the Electrolyte Composition on SEI Reactions at Si Anodes of Li-Ion Batteries. *The J. Phys. Chem. C* **2015,** *119* (13), 7060-7068.
209. Teng, X.; Zhan, C.; Bai, Y.; Ma, L.; Liu, Q.; Wu, C.; Wu, F.; Yang, Y.; Lu, J.; Amine, K., In Situ Analysis of Gas Generation in Lithium-Ion Batteries with Different Carbonate-Based Electrolytes. *ACS Appl. Mater. Interfaces* **2015,** *7* (41), 22751-22755.
210. Yang , J.; Solomatin, N.; Kraytsberg, A.; Ein-Eli , Y., In-Situ Spectro–electrochemical Insight Revealing Distinctive Silicon Anode Solid Electrolyte Interphase Formation in a Lithium–ion Battery. *ChemistrySelect* **2016,** *1* (3), 572-576.
211. Yoshida, H.; Fukunaga, T.; Hazama, T.; Terasaki, M.; Mizutani, M.; Yamachi, M., Degradation mechanism of alkyl carbonate solvents used in lithium-ion cells during initial charging. *J. Power Sources* **1997,** *68* (2), 311-315.
212. Novák, P.; Joho, F.; Imhof, R.; Panitz, J.-C.; Haas, O., In situ investigation of the interaction between graphite and electrolyte solutions. *J. Power Sources* **1999,** *81*, 212-216.
213. Schiele, A.; Breitung, B.; Hatsukade, T.; Berkes, B. B.; Hartmann, P.; Janek, J.; Brezesinski, T., The Critical Role of Fluoroethylene Carbonate in the Gassing of Silicon Anodes for Lithium-Ion Batteries. *ACS Energy Letters* **2017,** *2* (10), 2228-2233.
214. He, Y.-B.; Li, B.; Liu, M.; Zhang, C.; Lv, W.; Yang, C.; Li, J.; Du, H.; Zhang, B.; Yang, Q.-H.; Kim, J.-K.; Kang, F., Gassing in $Li_4Ti_5O_{12}$-based batteries and its remedy. **2012,** *2*, 913.
215. Song, W.; Bharath, S.; Reutt-Robey, J., Adsorption and Reaction Branching of Molecular Carbonates on Lithiated C(0001) Substrates. *The J. Phys. Chem. C* **2014,** *118* (33), 19017-19022.
216. Spinner, N. S.; Field, C. R.; Hammond, M. H.; Williams, B. A.; Myers, K. M.; Lubrano, A. L.; Rose-Pehrsson, S. L.; Tuttle, S. G., Physical and chemical analysis of lithium-ion battery cell-to-cell failure events inside custom fire chamber. *J. Power Sources* **2015,** *279*, 713-721.
217. Xiong, D. J.; Ellis, L. D.; Petibon, R.; Hynes, T.; Liu, Q. Q.; Dahn, J. R., Studies of Gas Generation, Gas Consumption and Impedance Growth in Li-Ion Cells with Carbonate or Fluorinated Electrolytes Using the Pouch Bag Method. *J. Electrochem. Soc.* **2017,** *164* (2), A340-A347.

218. Ghosh, A.; Hsu, B. B.; Dougal, S. M.; Afeworki, M.; Stevens, P. A.; Yeganeh, M. S., Effects of Gas Feed Ratios and Sequence on Ethylene Hydrogenation on Powder Pt Catalyst Studied by Sum Frequency Generation and Mass Spectrometry. *ACS Catalysis* **2014,** *4* (6), 1964-1971.
219. Braunschweig, B.; Mukherjee, P.; Haan, J. L.; Dlott, D. D., Vibrational sum-frequency generation study of the CO_2 electrochemical reduction at Pt/EMIM-BF_4 solid/liquid interfaces. *J. Electroanal. Chem.* **2017,** *800* (Supplement C), 144-150.
220. Corte, D. A. D.; Caillon, G.; Jordy, C.; Chazalviel, J. N.; Rosso, M.; Ozanam, F., Spectroscopic Insight into Li-Ion Batteries during Operation: An Alternative Infrared Approach. *Adv. Energy Mater.* **2016,** *6* (2).
221. Kwon, K.; Kong, F.; McLarnon, F.; Evans, J. W., Characterization of the SEI on a Carbon Film Electrode by Combined EQCM and Spectroscopic Ellipsometry. *J. Electrochem. Soc.* **2003,** *150* (2), A229-A233.
222. Nguyen, C. C.; Lucht, B. L., Comparative Study of Fluoroethylene Carbonate and Vinylene Carbonate for Silicon Anodes in Lithium Ion Batteries. *J. Electrochem. Soc.* **2014,** *161* (12), A1933-A1938.
223. Aurbach, D.; Ein-Eli, Y., The Study of Li-Graphite Intercalation Processes in Several Electrolyte Systems Using In Situ X-Ray Diffraction. *J. Electrochem. Soc.* **1995,** *142* (6), 1746-1752.
224. Shaw, S. K.; Lagutchev, A.; Dlott, D. D.; Gewirth, A. A., Sum-Frequency Spectroscopy of Molecular Adsorbates on Low-Index Ag Surfaces: Effects of Azimuthal Rotation. *Anal. Chem.* **2009,** *81* (3), 1154-1161.
225. Curtis, A. D.; Reynolds, S. B.; Calchera, A. R.; Patterson, J. E., Understanding the Role of Nonresonant Sum-Frequency Generation from Polystyrene Thin Films. *The J. Phys. Chem. Lett.* **2010,** *1* (16), 2435-2439.
226. Laaser, J. E.; Xiong, W.; Zanni, M. T., Time-Domain SFG Spectroscopy Using Mid-IR Pulse Shaping: Practical and Intrinsic Advantages. *The J. Phys. Chem. B* **2011,** *115* (11), 2536-2546.
227. Koelsch, P.; Muglali, M. I.; Rohwerder, M.; Erbe, A., Third-order effects in resonant sum-frequency-generation signals at electrified metal/liquid interfaces. *J. Opt. Soc. Am. B* **2013,** *30* (1), 219-223.
228. Krishnan, C. N.; Hauge, R. H.; Margrave, J. L., Studies of carbon monoxide activation with atomic lithium: IR spectra of LiCO, LiOC, LiC_2O_2 and $Li_2C_2O_2$ in cryogenic matrices. *J. Mol. Struct.* **1987,** *157* (1), 187-196.
229. Ayed, O.; Loutellier, A.; Manceron, L.; Perchard, J. P., Interaction between lithium and carbon monoxide. 1. A matrix infrared study. *J. Am. Chem. Soc.* **1986,** *108* (26), 8138-8147.
230. Kubo, T.; Aruga, T.; Takagi, N.; Nishijima, M., Adsorbed states of CO on the Si(100)-K surface: electron energy-loss spectroscopy and thermal desorption studies. *Surf. Sci.* **1998,** *395* (2), L246-L251.
231. Zhou, M.; Jiang, L.; Xu, Q., Reactions of silicon atoms and small clusters with CO: Experimental and theoretical characterization of Si_nCO(n=1–5), $Si_2(CO)_2$, c-Si_2(μ-O)(μ-CSi), and c-Si_2(μ-O)(μ-CCO) in solid argon. *The J. Chem. Phys.* **2004,** *121* (21), 10474-10482.
232. Laß, K.; Han, X.; Hasselbrink, E., Dynamics of the C–O stretch vibration on Si(100). *Surf. Sci.* **2006,** *600* (18), 4275-4279.
233. Shi, F.; Ross, P. N.; Zhao, H.; Liu, G.; Somorjai, G. A.; Komvopoulos, K., A Catalytic Path for Electrolyte Reduction in Lithium-Ion Cells Revealed by in Situ Attenuated Total Reflection-Fourier Transform Infrared Spectroscopy. *J. Am. Chem. Soc.* **2015,** *137* (9), 3181-3184.
234. Benitez, L.; Cristancho, D.; Seminario, J. M.; Martinez de la Hoz, J. M.; Balbuena, P. B., Electron transfer through solid-electrolyte-interphase layers formed on Si anodes of Li-ion batteries. *Electrochim. Acta* **2014,** *140* (Supplement C), 250-257.
235. Hankins, K.; Soto, F. A.; Balbuena, P. B., Insights into the Li Intercalation and SEI Formation on LiSi Nanoclusters. *J. Electrochem. Soc.* **2017,** *164* (11), E3457-E3464.

236. Soto, F. A.; Martinez de la Hoz, J. M.; Seminario, J. M.; Balbuena, P. B., Modeling solid-electrolyte interfacial phenomena in silicon anodes. *Current Opinion in Chemical Engineering* **2016,** *13*, 179-185.
237. Gourdin, G.; Zheng, D.; Qu, D., Adaption of kinetics to solid electrolyte interphase layer formation and application to electrolyte-soluble reaction products. *J. Power Sources* **2015,** *299*, 451-459.
238. Nie, M.; Abraham, D. P.; Chen, Y.; Bose, A.; Lucht, B. L., Silicon Solid Electrolyte Interphase (SEI) of Lithium Ion Battery Characterized by Microscopy and Spectroscopy. *The J. Phys. Chem. C* **2013,** *117* (26), 13403-13412.
239. Striebel, K. A.; Shim, J.; Kostecki, R.; Richardson, T. J.; Ross, P. N.; Song, X.; Zhuang, G. V., Characterization of high-power lithium-ion cells-performance and diagnostic analysis. 2003.
240. Brooker, M. H.; Bates, J. B., Raman and Infrared Spectral Studies of Anhydrous Li_2CO_3 and Na_2CO_3. *The J. Chem. Phys.* **1971,** *54* (11), 4788-4796.
241. Brooker, M. H.; Wang, J., Raman and infrared studies of lithium and cesium carbonates. *Spectrochimica Acta Part A: Molecular Spectroscopy* **1992,** *48* (7), 999-1008.
242. Martinez de la Hoz, J. M.; Balbuena, P. B., Reduction mechanisms of additives on Si anodes of Li-ion batteries. *PCCP* **2014,** *16* (32), 17091-17098.
243. Martinez de la Hoz, J. M.; Leung, K.; Balbuena, P. B., Reduction Mechanisms of Ethylene Carbonate on Si Anodes of Lithium-Ion Batteries: Effects of Degree of Lithiation and Nature of Exposed Surface. *ACS Appl. Mater. Interfaces* **2013,** *5* (24), 13457-13465.
244. Islam, M. M.; van Duin, A. C. T., Reductive Decomposition Reactions of Ethylene Carbonate by Explicit Electron Transfer from Lithium: An eReaxFF Molecular Dynamics Study. *The J. Phys. Chem. C* **2016,** *120* (48), 27128-27134.
245. Yang, Y.; Wang, Z.; Zhou, R.; Guo, H.; Li, X., Effects of lithium fluoride coating on the performance of nano-silicon as anode material for lithium-ion batteries. *Mater. Lett.* **2016,** *184*, 65-68.
246. Zhao, J.; Lu, Z.; Wang, H.; Liu, W.; Lee, H.-W.; Yan, K.; Zhuo, D.; Lin, D.; Liu, N.; Cui, Y., Artificial Solid Electrolyte Interphase-Protected Li_xSi Nanoparticles: An Efficient and Stable Prelithiation Reagent for Lithium-Ion Batteries. *J. Am. Chem. Soc.* **2015,** *137* (26), 8372-8375.
247. Hong, S.; Choo, M.-H.; Kwon, Y. H.; Kim, J. Y.; Song, S.-W., Interfacial Chemistry Control for Performance Enhancement of Micron Tin-Nickel/Graphite Battery Anode. *J. Electrochem. Soc.* **2014,** *161* (12), A1851-A1859.
248. Chen, X.; Li, X.; Mei, D.; Feng, J.; Hu, M. Y.; Hu, J.; Engelhard, M.; Zheng, J.; Xu, W.; Xiao, J.; Liu, J.; Zhang, J.-G., Reduction Mechanism of Fluoroethylene Carbonate for Stable Solid–Electrolyte Interphase Film on Silicon Anode. *ChemSusChem* **2014,** *7* (2), 549-554.
249. Mallouk, T.; Bartlett, N., Reversible intercalation of graphite by fluorine: a new bifluoride, $C_{12}HF_2$, and graphite fluorides, CF_x ($5 > x > 2$). *J. Chem. Soc., Chem. Commun.* **1983,** (3), 103-105.
250. Wang, Y.; Lee, W. C.; Manga, K. K.; Ang, P. K.; Lu, J.; Liu, Y. P.; Lim, C. T.; Loh, K. P., Fluorinated Graphene for Promoting Neuro-Induction of Stem Cells. *Adv. Mater.* **2012,** *24* (31), 4285-4290.
251. Wang, X.; Dai, Y.; Gao, J.; Huang, J.; Li, B.; Fan, C.; Yang, J.; Liu, X., High-Yield Production of Highly Fluorinated Graphene by Direct Heating Fluorination of Graphene-oxide. *ACS Appl. Mater. Interfaces* **2013,** *5* (17), 8294-8299.

Chapter 4: Germanium Nanowire Battery Electrodes with Engineered Surface-Binder Interactions Exhibit Improved Cycle Life and High-Energy-Density Without Fluorinated Additives

4.1 Overview: Nanostructured Group-IV materials hold great promise as high-capacity conversion electrodes for electrochemical energy storage. In the previous chapter it was concluded that in order to stabilize their cycling performance, the intentional incorporation of fluorinated electrolyte additives, such as fluoroethylene carbonate (FEC), has been deemed necessary to mitigate the recurrence of irreversible reactions that form the solid-electrolyte interphase (SEI) layer between the electrode and the electrolyte. This highlights the critical importance of interfacial chemistry for robust electrochemical systems. Yet, the surface chemistry of the active material is often neglected prior to electrode fabrication. Here we investigate the electrochemical cycling of germanium nanowire composite conversion electrodes with controlled surface chemistry, formulated with an array of polymeric binders, operating in the presence and in the absence of fluorinated electrolyte additives. We demonstrate that controlled electrode surface modification, when paired with certain binders, significantly improves the capacity retention and longevity of germanium nanowire-based electrodes in the complete *absence* of fluorinated compounds. Moreover, for certain surface chemistry/binder pairings, the inclusion of fluorinated additives was actually observed to *degrade* electrode performance while non-fluorinated additives (such as vinylene carbonate, VC) resulted in optimal device performance. These observations highlight that the active material surface chemistry can influence the components of the SEI layer that affect cycle life in addition to the reductive decomposition of electrolyte solvents and additives. In addition, we systematically investigate the often-overlooked impact of different electrode slurry preparation techniques on the performance of germanium nanowire composite electrodes fabricated with different polymeric binders.

4.2 Introduction:

Group-IV materials, such as silicon and germanium, continue to garner increasing interest as prospective replacements for graphite as negative electrode materials in lithium ion (Li-ion) batteries due to their order of magnitude higher gravimetric lithium storage capacities of 3579 mAh/g and 1384 mAh/g, respectively.[252] Both silicon and germanium undergo large volume changes (~300%) upon lithiation,[37] which can cause capacity loss through electrode fracture, deleterious irreversible reactions that trap lithium ions, and electrode delamination from the current collector. Strain and electrode fracture associated with these volume changes can be reduced by nanostructuring the active electrode material,[31, 37, 160, 253-259] particularly for nanowires.[37, 91, 260-261] Nanowires produced via colloidal, solution-based methods have been integrated as active materials in devices as freestanding fabrics[262] and as components within a composite electrode.[263-266] Composite electrodes are most commonly obtained by preparing a slurry of active material, conductive carbon, and polymeric binder in some optimized ratio.

Ongoing strategies to improve the cycle life of conversion electrode materials in composite architectures often hinge on controlling the solid-electrolyte interphase (SEI) layer[167, 238, 248, 267-270] composition and stability, an example of which is described in chapter 3 of this dissertation. The SEI layer is a heterogeneous coating of inorganic and organic compounds that forms as electrolyte solvents undergo electrochemical redox processes to form decomposition products at the electrode-electrolyte interface. Both the active material and composite electrode components at the electrode-electrolyte interface can influence the composition and stability of the SEI layer during electrochemical cycling.[270] The continued growth of the SEI layer throughout cycling can lead to the trapping of mobile ions within the layer as well as increased ionic resistance, leading to increasing electrochemical impedance.[173] Additionally, the redox byproducts of electrolyte solvents may be soluble in the electrolyte itself, forming a soluble (rather than solid) electrolyte interface.[56, 233, 271-272] Thus, a robust SEI layer is necessary for stable cycling, but the continued growth of the SEI layer, which can occur if fresh electrode surface is exposed, can result in poor capacity retention.

Electrolyte solvents and additives have been shown to strongly influence the cycle life of silicon- and germanium-based electrodes by altering the SEI layer composition, thickness, and ionic conductivity.[60, 167, 172, 238, 264] Additional strategies have focused on modifying the mechanical and conductive properties of the polymeric binder to enhance its ability to accommodate large volume changes and maintain adhesion to the current collector as well as enhance charge transport, respectively.[53, 273-278] Polymeric binders can also influence the composition of the SEI layer by undergoing different degrees of swelling with the electrolyte solvent, either facilitating or inhibiting reactions at the interface between the binder and the active material.[277, 279-280]

The relative reduction potentials of electrolyte solvents and additives largely govern which electrochemical decomposition products are formed first, establishing the innermost portion of the SEI layer, closest to the active material surface.[281-282] The subsequent composition and morphology of the SEI ultimately affects capacity retention.[55, 283-286] In particular, incorporating the FEC additive has consistently been demonstrated to be advantageous – and often considered necessary – in numerous alloying conversion electrode systems, including silicon, germanium, and antimony-based electrodes; however, these studies are often performed using materials that likely have surface oxides present due to how the materials are produced and handled.[264, 287-288] Without surface functionalization or active coating processes, a native oxide layer forms on Group IV active materials after brief air exposure upon removal from their growth chamber. This native oxide is particularly important, as it has been proposed to affect the electrochemistry of the SEI layer.[289-291] Moreover, for germanium nanowire-based composite electrodes using nanowires with oxide-terminated surfaces, FEC has appeared to be a critical electrolyte additive for retaining cell capacity and cycle life.[264] Alternatively, alkanethiol functionalized germanium nanowire-based electrodes were recently

demonstrated to have excellent capacity retention over extended cycling using a conventional electrolyte without FEC.[263] Thus, despite the clear importance of interfacial surface chemistry for conversion electrodes, investigations of nanowire conversion electrodes with careful, well-defined surface chemistry are somewhat limited, likely due to the added difficulty and expense of etching and tailoring nanowire surface chemistry after air exposure.[292] Likewise, the role of various electrolyte additives has yet to be explored on oxide-free germanium nanowire electrode surfaces. By comparing electrolyte additives that are structurally similar and undergo similar reductive decomposition pathways, we reveal how the electrochemical performance of oxide-free, surface-functionalized germanium nanowires correlates with electrolyte compositions.

Here, we use supercritical fluid-liquid-solid (SFLS)-grown germanium nanowires as a model material system to understand the effects of surface chemistry on conversion-type electrode materials. The SFLS process enables *in situ* surface-functionalization, eliminating potentially expensive and unwieldy acid etching steps and interface oxidation from air exposure. Moreover, since the entire synthesis is carried out in an easily evaporated, volatile organic solvent (toluene in this case), functionalized nanowire surfaces have intrinsically well-defined surface chemistries, without the need for intensive processing steps to purify samples and remove oily high-boiling-point solvents. We capitalize on the controlled thermal hydrogermylation of the native germanium nanowire surfaces *in situ*,[293] and subsequently incorporate these functionalized nanowires into composite electrodes with different polymeric binders and electrolyte additives to explore how engineering the interfacial chemistry of functionalized nanowires influences cycle life for composite conversion electrodes. We observe both an electrolyte and fabrication-dependent capacity retention manifests by de-lithiation from amorphous and crystalline domains of Ge nanomaterial.

4.3 Results and Discussion:

Figure 1a shows TEM images of germanium nanowires prior to integration into composite electrodes. The high resolution TEM image in Figure 1a and the corresponding FFT (inset) indicate that the SFLS-grown Au-seeded germanium nanowires are single-crystalline prior to lithiation, as expected. Germanium nanowire composite electrodes fabricated using PAA as a binder (Figure 1b) along with a range of electrolyte additives, demonstrate ~1100 mAh/g gravimetric capacities after 50 cycles, which is close to the theoretical specific capacity of germanium, confirming the high quality of these composite electrodes. Although the presence of a large specific capacity is a significant metric for the evaluation of device performance, we also use capacity retention (Figure 1d) as a metric to normalize and compare the extent of degradation between electrodes that may have slight variations in absolute capacity.

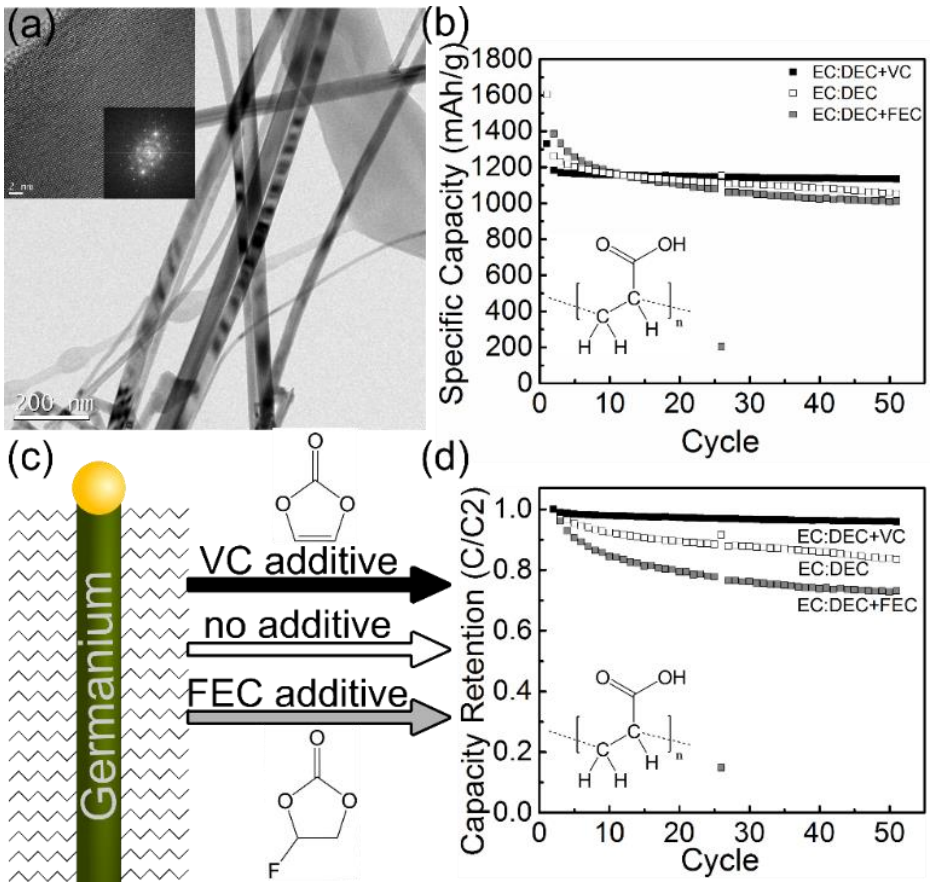

Figure 1. (a) TEM images of gold-seeded 1-octene hydrogermylated germanium nanowires and (inset) FFT of a high-resolution TEM image. (b) Specific gravimetric capacity of germanium nanowire electrode composites fabricated via manual mixing, using PAA as a binder, and 1 M $LiPF_6$ in 1:1 w/w EC:DEC with different additives: white (no additive), gray (FEC), and black (VC), cycled at a rate of C/10. (c) Depiction of a 1-octene hydrogermylated germanium nanowire with different electrolyte additives and (d) the capacity retention of germanium nanowire composite electrodes fabricated with PAA and cycled at a rate of C/10 with different electrolyte additives: white (no additive), gray (FEC), and black (VC) squares. Structural formulas of PAA, FEC, and VC are included for reference.

Interestingly, for the hydrogermylated nanowires implemented in this study, including FEC as an electrolyte additive *adversely* affected the capacity retention and cycle life (Figure 1d) of the electrode, consistently resulting in the poorest performing devices that employ this particular surface chemistry/binder pairing. Quantitatively, our devices using neat electrolyte solvents without additives (1:1 EC:DEC + 1M $LiPF_6$) consistently exhibit greater capacity retention after fifty cycles (83%) than devices that *included* the FEC additive (73%). While this performance is comparable to the performance of devices containing alkanethiolate-passivated nanowires cycled in the absence of FEC that used PVDF as a binder,[263] our results are in stark contrast to previous studies on surface-oxidized Ge nanowires,[264] which showed that FEC was critical for robust cycling and capacity retention.

There has been much discussion in the literature related to the decomposition of fluorinated additives leading to the formation of LiF in the SEI layer, with numerous sources detailing an enhanced accumulation of LiF that could be advantageous with respect to mitigating or etching potential surface oxide,[294-296] but for unoxidized functionalized electrode surfaces, including fluorinated additives yields no apparent benefit. In fact, using non-fluorinated VC as an electrolyte additive results in the greatest overall capacity retention for our hydrogermylated germanium nanowire devices (96%). Devices that included VC as an electrolyte additive showed high coulombic efficiencies reaching 99.5% (Figure C2). Importantly, it has been shown that both additives investigated here, VC and FEC, undergo similar reductive decomposition pathways.[174-175, 297] The reductive decomposition mechanism of FEC has been postulated to result in the generation of both VC and lithium fluoride (LiF),[175, 298-299] whereupon VC has been described to continue electrochemical reduction to form unique polymeric structures that form at the electrode surface.[172] These decomposition products are then ultimately integrated into the SEI layer, the composition of which plays a key role in the sustained performance of high capacity conversion electrodes.

To further elucidate the impact of fluorinated compounds on the capacity retention of alkane-functionalized germanium nanowire composite electrodes with controlled surface chemistry, additional electrodes were cycled in the complete absence of all possible source of fluorine. The standard electrolyte salt, $LiPF_6$, was replaced with $LiClO_4$, and the fluorine-free PAA binder was employed once again – as opposed to the widely used, fluorine-containing PVDF binder system. Although fluorine-free cells formulated without electrolyte additives exhibited continuous capacity decay (Figure 2, white squares) with a capacity retention of 83% after 50 cycles, when the fluorine-free additive, VC, was included as an electrolyte additive (black squares), capacity retention improved to 98%, consistently resulting in our best overall device performance with absolutely no fluorine present anywhere in the electrochemical system. These observations strongly suggest that the polymeric network created by the reductive decomposition of VC is much more important for generating a robust SEI layer than forming LiF for electrodes made using germanium nanowires with unoxidized alkane-functionalized surfaces. Previous data on bare Ge nanowires cycled with a VC electrolyte additive in the absence of binder[300] reveal a lower capacity retention (~75%) within the first 15 cycles than what was observed in this study, suggesting that alkane functionalization and/or the inclusion of PAA binder imparts greater cycling stability to the active material.

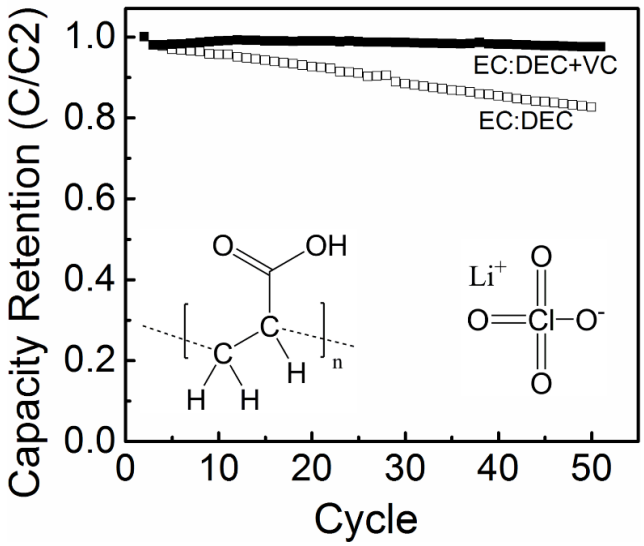

Figure 2. Capacity retention of fluorine-free germanium nanowire-based composite electrodes fabricated via manual mixing with PAA as a binder, using lithium perchlorate as an electrolyte salt without electrolyte additives (white squares) and with VC (black squares). Structural formulas of the lithium perchlorate electrolyte salt and PAA binder are included for reference.

In an effort to better distinguish the different mechanisms of capacity retention that occur during cycling, differential capacity plots (Figure 3) from the devices shown in Figure 1 were analyzed to see how the electrochemical events in each composite changed over the course of 50 cycles for each electrolyte formulation. Negative values along the ordinate in these plots correspond to lithiation, sweeping the voltage from 1 to 0.01 V, while positive values along the ordinate correspond to delithiation as the potential is swept from 0.01 to 1 V. For all electrolyte formulations, there is a sharp peak during the first cycle, corresponding to a two-phase transition at 0.37 V associated with lithiation of crystalline germanium,[301-302] but this peak does not appear in subsequent cycles. As such, this initial feature is ascribed to the lithiation-induced amorphization of crystalline germanium. In all subsequent cycles, the lithiation of amorphous germanium (a-Ge) proceeds via three broad peaks at 0.55 V, 0.4 V, and 0.2 V, which are characteristic of amorphous Li_xGe_y. Delithiation of lithiated germanium exhibits a distinctive peak at ~0.5 V, which corresponds to the delithiation of crystalline $Li_{15}Ge_4$. In past work,[264] capacity retention in germanium nanowire electrodes has been primarily associated with preserved delithiation peak intensities at ~0.5 V as cycling proceeds. Indeed, less efficient capacity retention was observed for devices that showed a decrease in this sharp delithiation peak following extended cycling. In addition, a broad delithiation shoulder centered near 0.4 V (*e.g.* Figure 3a) evolves over an increasing number of cycles for certain electrolyte compositions. Although this broad shoulder has not specifically been assigned previously for germanium alloying electrodes, by making an analogy to studies of silicon lithiation and delithiation,[303] we suggest that this feature corresponds to delithiation from amorphous domains of the active material ($a\text{-}Li_xGe_y$).

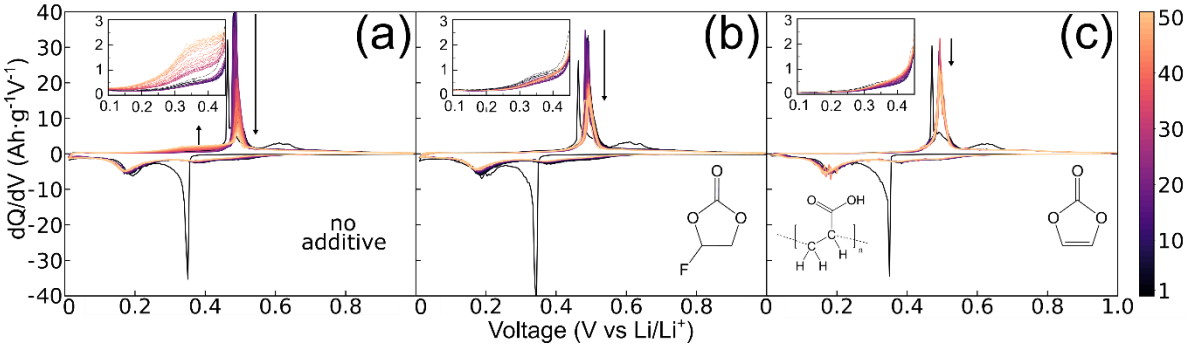

Figure 3. Total differential capacity plots of 1-octene hydrogermylated germanium nanowire composite electrodes that employ PAA as a binder, EC/DEC + 1M $LiPF_6$ as an electrolyte with (a) no electrolyte additive, (b) FEC additive included, and (c) VC additive included. The color scale at the rightmost side represents the evolution of the differential capacity profile over 50 cycles among all electrolyte/binder combinations.

As can be seen from the plots in Figure 3, a comparison between the performance of germanium nanowire composite electrodes with different electrolyte additives demonstrates that the major lithiation and delithiation features of the total differential capacity plots are similar over the course of the first twenty cycles. However, the device without electrolyte additive (Figure 3a) shows a substantial decrease in the intensity of the sharp $Li_{15}Ge_4$ delithiation peak at ~ 0.5 V over extended cycling, along with the concomitant formation of the broad delithiation shoulder at ~ 0.4 V, corresponding to delithiation from a-Li_xGe_y as discussed above. Interestingly, these additive-free devices maintain better capacity retention than devices that include the FEC additive (Figure 1d), despite the decrease in peak intensity at 0.5 V, likely due to the emergence of a-Li_xGe_y as an additional source of delithiation capacity to compensate for the loss of Faradaic activity from the crystalline $Li_{15}Ge_4$ phase.

Including electrolyte additives (Figure 3b and Figure 3c, corresponding to FEC and VC) suppresses the ability to delithiate from a-Li_xGe_y domains, as evidenced by the absence of the broad shoulder at ~0.4V over 50 cycles. Although the inclusion of FEC is often observed to result in improved capacity retention, it does not appear to be necessary for improving capacity retention in our hydrogermylated germanium nanowire-based devices (Figure 1d). Additionally, the three features associated with the lithiation of a-Ge for the additive-free and FEC-containing devices (Figure 3a and Figure 3b) shifted to slightly lower potentials, while including VC as an additive (Figure 3c) maintained the position of the original three a-Ge lithiation peaks; this behavior is consistent with results of fluorine-free devices as well (Figure B3a). Moreover, when VC was used as an additive (Figure 3c, Figure B3b), there was little change in the position or intensity of any peaks over the course of 50 cycles. Furthermore, when VC was included, the crystalline $Li_{15}Ge_4$ delithiation peak at 0.5 V decreased the least out of the three device architectures (Figure 3c).

Although including VC resulted in the best performing devices, it is clear from the differences between the additive-free and FEC-containing devices (Figure 3a and 3b), in context with their capacity retention (Figure 1d), that overall capacity retention cannot be attributed to a single morphological habit (i.e. crystalline or amorphous domains of the active material). The device without any electrolyte additive (Figure 3a) leads us to believe that functionalizing the active material interface produces an SEI that minimizes the loss of capacity retention by comparison to unfunctionalized surfaces cited in this manuscript.

Importantly, the mechanical characteristics of binders can also affect composite electrode stability. Although this study focused on the use of PAA as a binder material, the highly fluorinated PVDF binder system is one of the most widely used polymeric binders for conversion electrode materials, including germanium nanowire composites.[263-264] Nonetheless, PAA has recently been implemented for silicon-based composite electrodes, with high capacity retention upon extended cycling.[304-306] The impressive performance of PAA composites has been attributed to the large elastic modulus of PAA,[307] hydrogen bonding of the carboxylate groups with native surface oxide present on silicon electrode materials,[277, 308] decreased swelling due to decreased electrolyte uptake,[309] and higher adhesion strength with the copper current collector.[310] However, because the germanium nanowire surfaces employed in this study have been functionalized *in situ* with an alkane monolayer to prevent surface oxidation, the observed benefits of using PAA as a binder largely appear to be due to its superior mechanical characteristics, such as the ability to withstand high strain from volume expansion of the active material and improved adhesion to the current collector, as opposed to the hydrogen bonding of the PAA carboxylate groups with an oxidized electrode surface.

Since polymeric binders are known to influence the mechanical stability and the SEI layer composition of composite electrodes,[53, 276-278, 307] we performed a direct comparison between the performance of PAA- (Figure 4b) and PVDF-based (Figure 4c) germanium nanowire composite electrodes. Importantly, we observed that the electrode processing technique chosen to prepare the electrode slurry (Figure 4a) drastically affects the performance of the device depending on the binder that is being used. As such, we investigated the implementation of two commonly used processing techniques for each polymeric binder: (i) manual mixing with a mortar and pestle and (ii) magnetic stirring in a glass vial. To our knowledge, there has not been a comparison of electrode preparation techniques for these types of highly anisotropic, conversion negative electrode materials. We demonstrate that choice of electrode processing technique is particularly critical for devices formulated using PVDF as a binder, and that magnetic stirring is overall a better choice for germanium nanowire-based composite electrode devices fabricated using either binder system. These results show that optimization of nanowire-based composite electrodes is highly dependent

on slurry preparation, composite architecture, and careful selection of a polymeric binder. This highlights the importance of optimizing electrode processing methods for composite electrode systems.

For PAA-based devices (Figure 4b), high capacity retention was achieved (>70%), irrespective of the electrode slurry preparation that was chosen, although magnetic stirring gave rise to composites that exhibited much better overall capacity retention. This effect is exacerbated significantly when PVDF is used as a binder, with PVDF-based devices exhibiting extremely poor capacity retention (~40%) when manual mixing is used to process the nanowire composite electrodes. Despite the apparent superiority of magnetic stirring over manual mixing, it is important to note that it is much easier to create devices with identical mass loadings using manual mixing for PAA-based electrodes (Figure B4), likely due to the heterogeneity of the magnetically stirred PAA/NMP dispersion, immediately prior to doctor-blading onto the current collector. Nonetheless, all devices prepared using PAA exhibited robust specific capacities and capacity retention, irrespective of variations in the specific active material loading in cells punched from different regions of the current collector. The observed variations are likely due to differences in electrode slurry viscosity with the different binders, and likely warrants further optimization of electrode slurry processing for highly anisotropic structures that are prone to flocculation in low viscosity solutions.[280, 311-312]

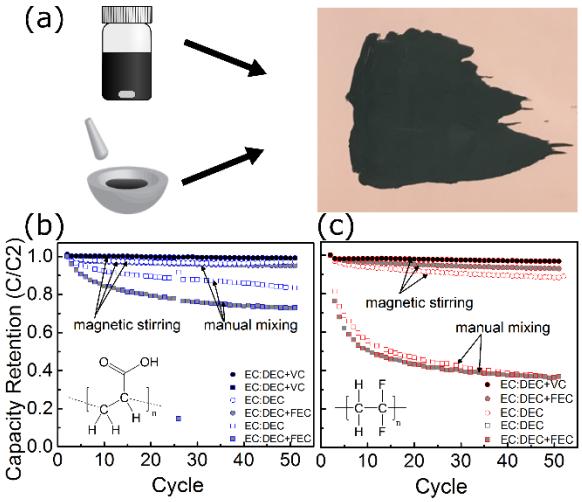

Figure 4. (a) Characteristic image of a germanium nanowire composite slurry (prepared via either magnetic stirring or manual mixing) doctor-bladed onto a copper foil. (b,c) Capacity retention of germanium nanowire-based electrodes using either (b) PAA or (c) PVDF as a binder, EC/DEC as the electrolyte, $LiPF_6$ as the electrolyte salt, and different electrolyte additives for the two different electrode processing techniques. Circles represent magnetically stirred electrode slurries, while squares represent manually

mixed electrode slurries. Unfilled symbols correspond to no electrolyte additive, gray fill corresponds to the use of FEC as an additive, and black fill indicates the use of VC additive.

Despite the inclusion of FEC, (Figure 4c, red outlined-gray squares), there was little improvement in capacity retention (36% vs. 37% capacity retention after 50 cycles) for PVDF-based devices prepared using manual mixing, which is somewhat surprising, given that fluorinated electrolyte additives have been shown to drastically improve capacity retention in both silicon and germanium nanomaterial-based composite electrodes.[167, 174, 257, 313-314] However, previous investigations that have integrated these materials into composite electrodes have typically employed magnetically stirred electrode slurries,[263-264] and indeed, we found that when using PVDF as a binder, magnetically stirring the electrode slurry drastically improved the capacity retention of our devices (Figure 4c, red outlined circles), which is in agreement with previously published results.[263-264] Nonetheless, in our hydrogermylated germanium nanowire composite electrodes prepared via magnetic stirring with PVDF (Figure 4c), we did not see the same improvement upon addition of FEC that had been previously reported in other studies of analogously processed, unfunctionalized germanium nanowire composite electrodes.[264] This observation builds on a growing body of evidence that actively functionalizing the surface of electrode materials could reduce the need for fluorinated additives to achieve high capacity retention, especially in conversion electrode systems.[263, 292] Moreover, when VC was used as an electrolyte additive for PVDF-based composites, we observed comparable performance to PAA-based devices that also employ VC. This strongly suggests that the formation of a robust SEI layer, in the absence of native oxides at the electrode surface, is strongly enhanced mainly due to the polymeric reductive decomposition products of VC.

For completeness, we also extend the total differential capacity analysis to devices prepared via magnetic stirring in the presence and absence of electrolyte additives for both polymeric binder systems in Figure 5. All devices show similar electrochemical features, but the three broad peaks associated with the lithiation of a-Ge again shift to slightly lower potentials for the additive-free devices (Figure 5a,d) and devices with FEC additive (Figure 5b,e), which is similar to the observed shifts in manually mixed PAA devices (Figure 3a,b). The devices with VC (Figure 5c,e) maintain the same peak potentials for the lithiation of a-Ge throughout cycling, as before.

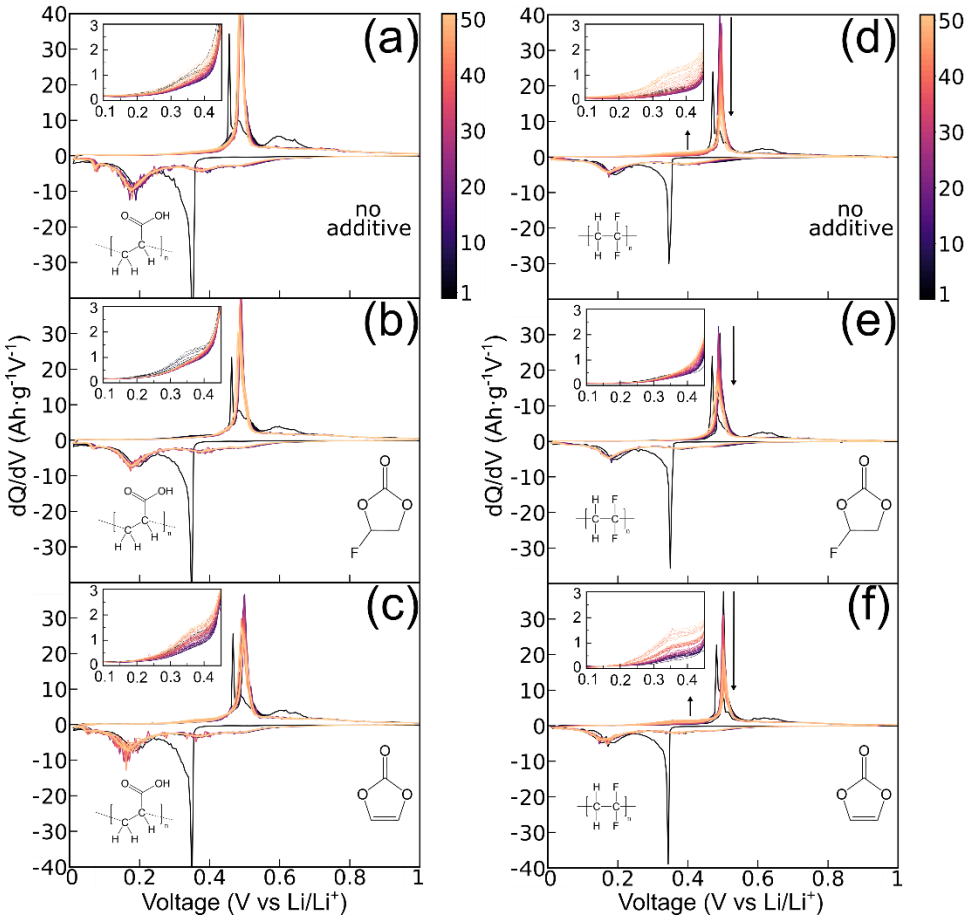

Figure 5. Total differential capacity plots of magnetically-stirred germanium nanowire composite electrode devices fabricated with EC/DEC electrolyte, $LiPF_6$ as the electrolyte salt, (a-c) PAA or (d-f) PVDF as the binder, and a range of electrolyte additives (a, d) no additive (b, e) FEC additive and (c, f) VC additive. Total differential capacity plots of magnetically-stirred germanium nanowire composite electrode devices fabricated with EC/DEC electrolyte, $LiPF_6$ as the electrolyte salt, (a-c) PAA or (d-f) PVDF as the binder, and a range of electrolyte additives (a, d) no additive (b, e) FEC additive and (c, f) VC additive.

Notably, all germanium nanowire-based PVDF devices that were prepared by magnetically stirring (Figure 5d–f) showed a decrease in the magnitude of the c-$Li_{15}Ge_4$ delithiation feature at 0.5 V, with Figure 5e displaying a slight shift of this peak to lower potentials as the electrode is cycled. In addition, PVDF-based devices with VC and without additive (Figure 5d,f) show the gradual appearance of the broad shoulder at 0.4 V discussed previously, indicative of delithiation from a-Li_xGe_y. This suggests that including VC as an electrolyte additive mitigates overpotential and, for PVDF devices, enables access to the delithiation of a-Li_xGe_y as an additional source of capacity. Including VC in this composite architecture does not completely suppress the evolution of the broad shoulder at 0.4 V, even though the crystalline delithiation peak at 0.5 V does not decrease as dramatically as it does when electrolyte additives are absent. This indicates that formulations which enable the amorphous delithiation transition (0.4 V), while also maintaining the

crystalline delithiation peak (0.5 V) could help to improve the cycle life of these high-capacity composite conversion electrodes.

4.4 Conclusion:

We demonstrate that high-capacity composite conversion electrodes formulated with unoxidized, 1-octene hydrogermylated germanium nanowires do not require commonly used fluorinated additives, such as FEC, in order to maintain robust capacity retention. Devices with controlled surface chemistry fabricated in the complete absence of fluorinated compounds consistently demonstrated among the best capacity retention and overall performance, while the inclusion of FEC often led to decreased capacity retention. In contrast, reductive decomposition of the nonfluorinated VC additive led to consistently superior device characteristics. Total differential capacity plots showed delithiation from a-Li_xGe_y as an additional source of capacity for some cell architectures, with the beneficial characteristics of the PAA binder being attributed to its intrinsic mechanical properties, rather than its ability to hydrogen bond with native surface oxides. In addition, we demonstrate that although both PAA and PVDF can be used as binders for germanium nanowire-based composite electrodes, the resultant device characteristics are highly dependent on the electrode processing technique that is chosen, particularly for PVDF-based devices. Most importantly, we demonstrate that FEC is not necessary to achieve robust capacity retention in high-capacity conversion electrodes, as long as the active material surface chemistry is carefully controlled. These results suggest that actively controlling chemical functionalization of the electrode surface of the active material in nanostructured electrode composites may be a general tool for controlling the active material/bind interactions that influence cycle life in next-generation high capacity conversion electrodes. Additionally, our results suggest that standardizing composite preparation methods may be critical for directly comparing the merits of new nanostructured composite formulations.

4.5 Appendix B:

Experimental details and supporting information

4.6 Acknowledgments:

This material is based in part upon work supported by the University of Washington Molecular Engineering Institute, and by the State of Washington through the University of Washington Clean Energy Institute and via funding from the Washington Research Foundation. Part of this work was conducted at the Research Training Testbed at the University of Washington, which is supported in part by funds from the Clean Energy Institute and the Washington Research Foundation, and at the Molecular Analysis Facility, a National Nanotechnology Coordinated Infrastructure site at the University of Washington which is

supported in part by the National Science Foundation (grant ECC-1542101), the University of Washington, the Molecular Engineering & Sciences Institute, and the Clean Energy Institute.

4.7 References:

31. Graetz, J.; Ahn, C. C.; Yazami, R.; Fultz, B., Nanocrystalline and Thin Film Germanium Electrodes with High Lithium Capacity and High Rate Capabilities. *J. Electrochem. Soc.* **2004,** *151* (5), A698-A702.
37. Liu, X. H.; Liu, Y.; Kushima, A.; Zhang, S.; Zhu, T.; Li, J.; Huang, J. Y., In Situ TEM Experiments of Electrochemical Lithiation and Delithiation of Individual Nanostructures. *Adv. Energy Mater.* **2012,** *2* (7), 722-741.
53. Erk, C.; Brezesinski, T.; Sommer, H.; Schneider, R.; Janek, J., Toward Silicon Anodes for Next-Generation Lithium Ion Batteries: A Comparative Performance Study of Various Polymer Binders and Silicon Nanopowders. *ACS Appl. Mater. Interfaces* **2013,** *5* (15), 7299-7307.
55. Michan, A. L.; Divitini, G.; Pell, A. J.; Leskes, M.; Ducati, C.; Grey, C. P., Solid Electrolyte Interphase Growth and Capacity Loss in Silicon Electrodes. *J. Am. Chem. Soc.* **2016,** *138* (25), 7918-7931.
56. Shi, F.; Zhao, H.; Liu, G.; Ross, P. N.; Somorjai, G. A.; Komvopoulos, K., Identification of Diethyl 2,5-Dioxahexane Dicarboxylate and Polyethylene Carbonate as Decomposition Products of Ethylene Carbonate Based Electrolytes by Fourier Transform Infrared Spectroscopy. *The J. Phys. Chem. C* **2014,** *118* (27), 14732-14738.
60. Lin, Y.-M.; Klavetter, K. C.; Abel, P. R.; Davy, N. C.; Snider, J. L.; Heller, A.; Mullins, C. B., High performance silicon nanoparticle anode in fluoroethylene carbonate-based electrolyte for Li-ion batteries. *Chem. Commun.* **2012,** *48* (58), 7268-7270.
91. Loaiza, L. C.; Louvain, N.; Fraisse, B.; Boulaoued, A.; Iadecola, A.; Johansson, P.; Stievano, L.; Seznec, V.; Monconduit, L., Electrochemical Lithiation of Ge: New Insights by Operando Spectroscopy and Diffraction. *The J. Phys. Chem. C* **2018,** *122* (7), 3709-3718.
160. Chan, C. K.; Peng, H.; Liu, G.; McIlwrath, K.; Zhang, X. F.; Huggins, R. A.; Cui, Y., High-performance lithium battery anodes using silicon nanowires. *Nat Nano* **2008,** *3* (1), 31-35.
167. Schroder, K.; Alvarado, J.; Yersak, T. A.; Li, J.; Dudney, N.; Webb, L. J.; Meng, Y. S.; Stevenson, K. J., The Effect of Fluoroethylene Carbonate as an Additive on the Solid Electrolyte Interphase on Silicon Lithium-Ion Electrodes. *Chem. Mater.* **2015,** *27* (16), 5531-5542.
172. Etacheri, V.; Haik, O.; Goffer, Y.; Roberts, G. A.; Stefan, I. C.; Fasching, R.; Aurbach, D., Effect of Fluoroethylene Carbonate (FEC) on the Performance and Surface Chemistry of Si-Nanowire Li-Ion Battery Anodes. *Langmuir* **2012,** *28* (1), 965-976.
173. Sloop, S. E.; Kerr, J. B.; Kinoshita, K., The role of Li-ion battery electrolyte reactivity in performance decline and self-discharge. *J. Power Sources* **2003,** *119*, 330-337.
174. Jung, R.; Metzger, M.; Haering, D.; Solchenbach, S.; Marino, C.; Tsiouvaras, N.; Stinner, C.; Gasteiger, H. A., Consumption of Fluoroethylene Carbonate (FEC) on Si-C Composite Electrodes for Li-Ion Batteries. *J. Electrochem. Soc.* **2016,** *163* (8), A1705-A1716.
175. Michan, A. L.; Parimalam, B. S.; Leskes, M.; Kerber, R. N.; Yoon, T.; Grey, C. P.; Lucht, B. L., Fluoroethylene Carbonate and Vinylene Carbonate Reduction: Understanding Lithium-Ion Battery Electrolyte Additives and Solid Electrolyte Interphase Formation. *Chem. Mater.* **2016**, *28* (22) 8149-8159
233. Shi, F.; Ross, P. N.; Zhao, H.; Liu, G.; Somorjai, G. A.; Komvopoulos, K., A Catalytic Path for Electrolyte Reduction in Lithium-Ion Cells Revealed by in Situ Attenuated Total Reflection-Fourier Transform Infrared Spectroscopy. *J. Am. Chem. Soc.* **2015,** *137* (9), 3181-3184.

238. Nie, M.; Abraham, D. P.; Chen, Y.; Bose, A.; Lucht, B. L., Silicon Solid Electrolyte Interphase (SEI) of Lithium Ion Battery Characterized by Microscopy and Spectroscopy. *The J. Phys. Chem. C* **2013,** *117* (26), 13403-13412.
248. Chen, X.; Li, X.; Mei, D.; Feng, J.; Hu, M. Y.; Hu, J.; Engelhard, M.; Zheng, J.; Xu, W.; Xiao, J.; Liu, J.; Zhang, J.-G., Reduction Mechanism of Fluoroethylene Carbonate for Stable Solid–Electrolyte Interphase Film on Silicon Anode. *ChemSusChem* **2014,** *7* (2), 549-554.
252. Tian, H.; Xin, F.; Wang, X.; He, W.; Han, W., High capacity group-IV elements (Si, Ge, Sn) based anodes for lithium-ion batteries. *Journal of Materiomics* **2015,** *1* (3), 153-169.
253. Graetz, J.; Ahn, C. C.; Yazami, R.; Fultz, B., Highly Reversible Lithium Storage in Nanostructured Silicon. *Electrochem. Solid-State Lett.* **2003,** *6* (9), A194-A197.
254. Rudawski, N. G.; Darby, B. L.; Yates, B. R.; Jones, K. S.; Elliman, R. G.; Volinsky, A. A., Nanostructured ion beam-modified Ge films for high capacity Li ion battery anodes. *Appl. Phys. Lett.* **2012,** *100* (8), 083111.
255. Seng, K. H.; Park, M.-H.; Guo, Z. P.; Liu, H. K.; Cho, J., Self-Assembled Germanium/Carbon Nanostructures as High-Power Anode Material for the Lithium-Ion Battery. *Angew. Chem.* **2012,** *124* (23), 5755-5759.
256. Li, W.; Yang, Z.; Cheng, J.; Zhong, X.; Gu, L.; Yu, Y., Germanium nanoparticles encapsulated in flexible carbon nanofibers as self-supported electrodes for high performance lithium-ion batteries. *Nanoscale* **2014,** *6* (9), 4532-4537.
257. Klavetter, K. C.; Wood, S. M.; Lin, Y.-M.; Snider, J. L.; Davy, N. C.; Chockla, A. M.; Romanovicz, D. K.; Korgel, B. A.; Lee, J.-W.; Heller, A.; Mullins, C. B., A high-rate germanium-particle slurry cast Li-ion anode with high Coulombic efficiency and long cycle life. *J. Power Sources* **2013,** *238*, 123-136.
258. Park, M. H.; Cho, Y.; Kim, K.; Kim, J.; Liu, M.; Cho, J., Germanium Nanotubes Prepared by Using the Kirkendall Effect as Anodes for High-Rate Lithium Batteries. *Angew. Chem. Int. Ed.* **2011,** *50* (41), 9647-9650.
259. Liu, N.; Lu, Z.; Zhao, J.; McDowell, M. T.; Lee, H.-W.; Zhao, W.; Cui, Y., A pomegranate-inspired nanoscale design for large-volume-change lithium battery anodes. *Nat. Nanotechnol.* **2014,** *9* (3), 187-192.
260. Liu, X. H.; Huang, S.; Picraux, S. T.; Li, J.; Zhu, T.; Huang, J. Y., Reversible Nanopore Formation in Ge Nanowires during Lithiation–Delithiation Cycling: An In Situ Transmission Electron Microscopy Study. *Nano Lett.* **2011,** *11* (9), 3991-3997.
261. Kennedy, T.; Mullane, E.; Geaney, H.; Osiak, M.; O'Dwyer, C.; Ryan, K. M., High-Performance Germanium Nanowire-Based Lithium-Ion Battery Anodes Extending over 1000 Cycles Through in Situ Formation of a Continuous Porous Network. *Nano Lett.* **2014,** *14* (2), 716-723.
262. Chockla, A. M.; Harris, J. T.; Akhavan, V. A.; Bogart, T. D.; Holmberg, V. C.; Steinhagen, C.; Mullins, C. B.; Stevenson, K. J.; Korgel, B. A., Silicon Nanowire Fabric as a Lithium Ion Battery Electrode Material. *J. Am. Chem. Soc.* **2011,** *133* (51), 20914-20921.
263. Yuan, F.-W.; Yang, H.-J.; Tuan, H.-Y., Alkanethiol-Passivated Ge Nanowires as High-Performance Anode Materials for Lithium-Ion Batteries: The Role of Chemical Surface Functionalization. *ACS Nano* **2012,** *6* (11), 9932-9942.
264. Chockla, A. M.; Klavetter, K. C.; Mullins, C. B.; Korgel, B. A., Solution-Grown Germanium Nanowire Anodes for Lithium-Ion Batteries. *ACS Appl. Mater. Interfaces* **2012,** *4* (9), 4658-4664.
265. Chockla, A. M.; Klavetter, K. C.; Mullins, C. B.; Korgel, B. A., Tin-Seeded Silicon Nanowires for High Capacity Li-Ion Batteries. *Chem. Mater.* **2012,** *24* (19), 3738-3745.
266. Bogart, T. D.; Chockla, A. M.; Korgel, B. A., High capacity lithium ion battery anodes of silicon and germanium. *Current Opinion in Chemical Engineering* **2013,** *2* (3), 286-293.
267. Chan, C. K.; Ruffo, R.; Hong, S. S.; Cui, Y., Surface chemistry and morphology of the solid electrolyte interphase on silicon nanowire lithium-ion battery anodes. *J. Power Sources* **2009,** *189* (2), 1132-1140.

268. Nakai, H.; Kubota, T.; Kita, A.; Kawashima, A., Investigation of the Solid Electrolyte Interphase Formed by Fluoroethylene Carbonate on Si Electrodes. *J. Electrochem. Soc.* **2011,** *158* (7), A798-A801.
269. Schroder, K. W.; Dylla, A. G.; Harris, S. J.; Webb, L. J.; Stevenson, K. J., Role of Surface Oxides in the Formation of Solid–Electrolyte Interphases at Silicon Electrodes for Lithium-Ion Batteries. *ACS Appl. Mater. Interfaces* **2014,** *6* (23), 21510-21524.
270. Verma, P.; Maire, P.; Novák, P., A review of the features and analyses of the solid electrolyte interphase in Li-ion batteries. *Electrochim. Acta* **2010,** *55* (22), 6332-6341.
271. Burkhardt, S. E., Impact of Chemical Follow-up Reactions for Lithium Ion Electrolytes: Generation of Nucleophilic Species, Solid Electrolyte Interphase, and Gas Formation. *J. Electrochem. Soc.* **2017,** *164* (4), A684-A690.
272. Olson, J. Z.; Johansson, P. K.; Castner, D. G.; Schlenker, C. W., Operando Sum-Frequency Generation Detection of Electrolyte Redox Products at Active Si Nanoparticle Li-Ion Battery Interfaces. *Chem. Mater.* **2018,** *30* (4), 1239-1248.
273. Liu, G.; Xun, S.; Vukmirovic, N.; Song, X.; Olalde-Velasco, P.; Zheng, H.; Battaglia, V. S.; Wang, L.; Yang, W., Polymers with Tailored Electronic Structure for High Capacity Lithium Battery Electrodes. *Adv. Mater.* **2011,** *23* (40), 4679-4683.
274. Wu, H.; Yu, G.; Pan, L.; Liu, N.; McDowell, M. T.; Bao, Z.; Cui, Y., Stable Li-ion battery anodes by *in-situ* polymerization of conducting hydrogel to conformally coat silicon nanoparticles. *Nat. Commun.* **2013,** *4*, 1943.
275. Assresahegn, B. D.; Bélanger, D., Synthesis of binder-like molecules covalently linked to silicon nanoparticles and application as anode material for lithium-ion batteries without the use of electrolyte additives. *J. Power Sources* **2017,** *345* (Supplement C), 190-201.
276. Chockla, A. M.; Bogart, T. D.; Hessel, C. M.; Klavetter, K. C.; Mullins, C. B.; Korgel, B. A., Influences of Gold, Binder and Electrolyte on Silicon Nanowire Performance in Li-Ion Batteries. *The J. Phys. Chem. C* **2012,** *116* (34), 18079-18086.
277. Koo, B.; Kim, H.; Cho, Y.; Lee, K. T.; Choi, N.-S.; Cho, J., A Highly Cross-Linked Polymeric Binder for High-Performance Silicon Negative Electrodes in Lithium Ion Batteries. *Angew. Chem. Int. Ed.* **2012,** *51* (35), 8762-8767.
278. Komaba, S.; Yabuuchi, N.; Ozeki, T.; Han, Z.-J.; Shimomura, K.; Yui, H.; Katayama, Y.; Miura, T., Comparative Study of Sodium Polyacrylate and Poly(vinylidene fluoride) as Binders for High Capacity Si–Graphite Composite Negative Electrodes in Li-Ion Batteries. *The J. Phys. Chem. C* **2012,** *116* (1), 1380-1389.
279. Favors, Z.; Bay, H. H.; Mutlu, Z.; Ahmed, K.; Ionescu, R.; Ye, R.; Ozkan, M.; Ozkan, C. S., Towards Scalable Binderless Electrodes: Carbon Coated Silicon Nanofiber Paper via Mg Reduction of Electrospun SiO_2 Nanofibers. *Sci. Rep.* **2015,** *5*, 8246.
280. Kovalenko, I.; Zdyrko, B.; Magasinski, A.; Hertzberg, B.; Milicev, Z.; Burtovyy, R.; Luzinov, I.; Yushin, G., A Major Constituent of Brown Algae for Use in High-Capacity Li-Ion Batteries. *Science* **2011,** *334* (6052), 75-79.
281. Zhang, X.; Kostecki, R.; Richardson, T. J.; Pugh, J. K.; Ross, P. N., Electrochemical and Infrared Studies of the Reduction of Organic Carbonates. *J. Electrochem. Soc.* **2001,** *148* (12), A1341-A1345.
282. Rustomji, C. S.; Yang, Y.; Kim, T. K.; Mac, J.; Kim, Y. J.; Caldwell, E.; Chung, H.; Meng, Y. S., Liquefied gas electrolytes for electrochemical energy storage devices. *Science* **2017,** *356* (6345).
283. Mishra, K., *The Effect of Solvent on the Capacity Retention in a Germanium Anode for Lithium Ion Batteries*. 2018; Vol. 15.
284. Nadimpalli, S.; A. Sethuraman, V.; Dalavi, S.; Lucht, B.; Chon, M.; B. Shenoy, V.; Guduru, P., *Quantifying Capacity Loss due to Solid-Electrolyte-Interphase Layer Formation on Silicon Negative Electrodes in Lithium-ion Batteries*. 2012; Vol. 215.

285. Fan, X.; Ji, X.; Han, F.; Yue, J.; Chen, J.; Chen, L.; Deng, T.; Jiang, J.; Wang, C., Fluorinated solid electrolyte interphase enables highly reversible solid-state Li metal battery. *Science Advances* **2018,** *4* (12), eaau9245.
286. Wu, B.; Wang, S.; Lochala, J.; Desrochers, D.; Liu, B.; Zhang, W.; Yang, J.; Xiao, J., The role of the solid electrolyte interphase layer in preventing Li dendrite growth in solid-state batteries. *Energy Environ. Sci.* **2018,** *11* (7), 1803-1810.
287. Dalavi, S.; Guduru, P.; Lucht, B. L., Performance Enhancing Electrolyte Additives for Lithium Ion Batteries with Silicon Anodes. *J. Electrochem. Soc.* **2012,** *159* (5), A642-A646.
288. Ji, L.; Gu, M.; Shao, Y.; Li, X.; Engelhard, M. H.; Arey, B. W.; Wang, W.; Nie, Z.; Xiao, J.; Wang, C.; Zhang, J.-G.; Liu, J., Controlling SEI Formation on SnSb-Porous Carbon Nanofibers for Improved Na Ion Storage. *Adv. Mater.* **2014,** *26* (18), 2901-2908.
289. Xun, S.; Song, X.; Wang, L.; Grass, M. E.; Liu, Z.; Battaglia, V. S.; Liu, G., The Effects of Native Oxide Surface Layer on the Electrochemical Performance of Si Nanoparticle-Based Electrodes. *J. Electrochem. Soc.* **2011,** *158* (12), A1260.
290. He, Y.; Piper, D. M.; Gu, M.; Travis, J. J.; George, S. M.; Lee, S.-H.; Genc, A.; Pullan, L.; Liu, J.; Mao, S. X.; Zhang, J.-G.; Ban, C.; Wang, C., In Situ Transmission Electron Microscopy Probing of Native Oxide and Artificial Layers on Silicon Nanoparticles for Lithium Ion Batteries. *ACS Nano* **2014,** *8* (11), 11816-11823.
291. Schroder, K. W.; Celio, H.; Webb, L. J.; Stevenson, K. J., Examining Solid Electrolyte Interphase Formation on Crystalline Silicon Electrodes: Influence of Electrochemical Preparation and Ambient Exposure Conditions. *The J. Phys. Chem. C* **2012,** *116* (37), 19737-19747.
292. Xu, W.; Vegunta, S. S. S.; Flake, J. C., Surface-modified silicon nanowire anodes for lithium-ion batteries. *J. Power Sources* **2011,** *196* (20), 8583-8589.
293. Holmberg, V. C.; Korgel, B. A., Corrosion Resistance of Thiol- and Alkene-Passivated Germanium Nanowires. *Chem. Mater.* **2010,** *22* (12), 3698-3703.
294. Sina, M.; Alvarado, J.; Shobukawa, H.; Alexander, C.; Manichev, V.; Feldman, L.; Gustafsson, T.; Stevenson, K. J.; Meng, Y. S., Direct Visualization of the Solid Electrolyte Interphase and Its Effects on Silicon Electrochemical Performance. *Adv. Mater. Interfaces* **2016,** *3* (20).
295. Philippe, B.; Dedryvère, R.; Allouche, J.; Lindgren, F.; Gorgoi, M.; Rensmo, H.; Gonbeau, D.; Edström, K., Nanosilicon Electrodes for Lithium-Ion Batteries: Interfacial Mechanisms Studied by Hard and Soft X-ray Photoelectron Spectroscopy. *Chem. Mater.* **2012,** *24* (6), 1107-1115.
296. Radvanyi, E.; De Vito, E.; Porcher, W.; Jouanneau Si Larbi, S., An XPS/AES comparative study of the surface behaviour of nano-silicon anodes for Li-ion batteries. *J. Anal. At. Spectrom.* **2014,** *29* (6), 1120-1131.
297. Profatilova, I. A.; Stock, C.; Schmitz, A.; Passerini, S.; Winter, M., Enhanced thermal stability of a lithiated nano-silicon electrode by fluoroethylene carbonate and vinylene carbonate. *J. Power Sources* **2013,** *222* (Supplement C), 140-149.
298. Shkrob, I. A.; Wishart, J. F.; Abraham, D. P., What Makes Fluoroethylene Carbonate Different? *The J. Phys. Chem. C* **2015,** *119* (27), 14954-14964.
299. Zhao, X.; Zhuang, Q. C.; Xu, S. D.; Xu, Y. X.; Shi, Y. L.; Zhang, X. X., A New Insight into the Content Effect of Fluoroethylene Carbonate as a Film Forming Additive for Lithium-Ion Batteries. *International Journal of Electrochemical Science.* **2015.** 10 (*3*) p 2515-2534.
300. Aghazadeh Meshgi, M.; Biswas, S.; McNulty, D.; O'Dwyer, C.; Alessio Verni, G.; O'Connell, J.; Davitt, F.; Letofsky-Papst, I.; Poelt, P.; Holmes, J. D.; Marschner, C., Rapid, Low-Temperature Synthesis of Germanium Nanowires from Oligosilylgermane Precursors. *Chem. Mater.* **2017,** *29* (10), 4351-4360.
301. Lim, L. Y.; Liu, N.; Cui, Y.; Toney, M. F., Understanding Phase Transformation in Crystalline Ge Anodes for Li-Ion Batteries. *Chem. Mater.* **2014,** *26* (12), 3739-3746.
302. Lim, L. Y.; Fan, S.; Hng, H. H.; Toney, M. F., Storage Capacity and Cycling Stability in Ge Anodes: Relationship of Anode Structure and Cycling Rate. *Adv. Energy Mater.* **2015,** *5* (15).

303. Misra, S.; Liu, N.; Nelson, J.; Hong, S. S.; Cui, Y.; Toney, M. F., In Situ X-ray Diffraction Studies of (De)lithiation Mechanism in Silicon Nanowire Anodes. *ACS Nano* **2012,** *6* (6), 5465-5473.
304. Hu, B.; Shkrob, I. A.; Zhang, S.; Zhang, L.; Zhang, J.; Li, Y.; Liao, C.; Zhang, Z.; Lu, W.; Zhang, L., The existence of optimal molecular weight for poly(acrylic acid) binders in silicon/graphite composite anode for lithium-ion batteries. *J. Power Sources* **2018,** *378*, 671-676.
305. Huang, H., The Effect of Commercialized Binders on Silicon Oxide Anode Material for High Capacity Lithium ion Batteries. *International Journal of Electrochemical Science.* **2016.** 11 (*10*), 8697-8708.
306. Hu, B.; Jiang, S.; Zhang, J.; Zhang, Z.; Zhang, L., Lithiation Effect of the Poly(Acrylic Acid) Binders on the Silicon Anode of Lithium-Ion Batteries. *Meeting Abstracts* **2018,** *MA2018-01* (3), 461-461.
307. Magasinski, A.; Zdyrko, B.; Kovalenko, I.; Hertzberg, B.; Burtovyy, R.; Huebner, C. F.; Fuller, T. F.; Luzinov, I.; Yushin, G., Toward Efficient Binders for Li-Ion Battery Si-Based Anodes: Polyacrylic Acid. *ACS Appl. Mater. Interfaces* **2010,** *2* (11), 3004-3010.
308. Porcher, W.; Chazelle, S.; Boulineau, A.; Mariage, N.; Alper, J. P.; Van Rompaey, T.; Bridel, J. S.; Haon, C., Understanding Polyacrylic Acid and Lithium Polyacrylate Binder Behavior in Silicon Based Electrodes for Li-Ion Batteries. *J. Electrochem. Soc.* **2017,** *164* (14), A3633-A3640.
309. Urbanski, A.; Omar, A.; Guo, J.; Janke, A.; Reuter, U.; Malanin, M.; Schmidt, F.; Jehnichen, D.; Holzschuh, M.; Simon, F.; Eichhorn, K.-J.; Giebeler, L.; Uhlmann, P., An Efficient Two-Polymer Binder for High-Performance Silicon Nanoparticle-Based Lithium-Ion Batteries: A Systematic Case Study with Commercial Polyacrylic Acid and Polyvinyl Butyral Polymers. *J. Electrochem. Soc.* **2019,** *166* (3), A5275-A5286.
310. Lee, J.-H.; Paik, U.; Hackley, V. A.; Choi, Y.-M., Effect of poly(acrylic acid) on adhesion strength and electrochemical performance of natural graphite negative electrode for lithium-ion batteries. *J. Power Sources* **2006,** *161* (1), 612-616.
311. Kim, K. M.; Jeon, W. S.; Chung, I. J.; Chang, S. H., Effect of mixing sequences on the electrode characteristics of lithium-ion rechargeable batteries. *J. Power Sources* **1999,** *83* (1), 108-113.
312. Liu, T.-J.; Tiu, C.; Chen, L.-C.; Liu, D., The Influence of Slurry Rheology on Lithium-ion Electrode Processing. In *Printed Batteries*, Wiley-Blackwell: 2018; pp 63-79.
313. Yao, K.; Zheng, J. P.; Liang, R., Ethylene carbonate-free fluoroethylene carbonate-based electrolyte works better for freestanding Si-based composite paper anodes for Li-ion batteries. *J. Power Sources* **2018,** *381* (31), 164-170.
314. Jin, Y.; Kneusels, N.-J. H.; Magusin, P. C. M. M.; Kim, G.; Castillo-Martínez, E.; Marbella, L. E.; Kerber, R. N.; Howe, D. J.; Paul, S.; Liu, T.; Grey, C. P., Identifying the Structural Basis for the Increased Stability of the Solid Electrolyte Interphase Formed on Silicon with the Additive Fluoroethylene Carbonate. *J. Am. Chem. Soc.* **2017,** *139* (42), 14992-15004.

Chapter 5: Stark Tuning Rates of Organic Carbonates Used in Electrochemical Energy Storage

This chapter contains the work published originally in "Stark Tuning Rates of Organic Carbonates Used in Electrochemical Energy Storage Devices" by Olson, J. Z.; Schneider, S. H.; Johansson, P. K.; Luk, T. S.; Schlenker, C. W., in J. Phys. Chem. C 2019, 123 (18), 11484-11492 10.1021/acs.jpcc.9b01501

5.1 Overview:

Lithium ion batteries frequently employ carbonate-based electrolyte solvents to support reversible lithium ion storage in response to electric fields applied to the electrode/electrolyte junction. While these fields are critical for controlling beneficial and deleterious electrochemical reactions alike, quantifying their magnitude is a persistent challenge that inhibits our fundamental understanding of high-voltage electrochemical energy storage devices. In this study, we utilize complementary experimental techniques of vibrational Stark spectroscopy and vibrational solvatochromism in conjunction with molecular dynamics simulations to determine the vibrational sensitivity (Stark tuning rate, $\Delta\vec{\mu}$) of the carbonyl group (C=O) in response to an electric field for diethyl carbonate (DEC), ethylene carbonate (EC), and fluoroethylene carbonate (FEC). We first determine that the response of the C=O group in each solvent to an externally applied electric field exhibits a second-derivative line shape characteristic of the linear Stark effect. We find the magnitude of this response to be unique for each carbonate solvent based on a field-frequency calibration; $\Delta\vec{\mu}_{DEC}$ = 0.37 cm^{-1}/(MV/cm), $\Delta\vec{\mu}_{EC}$ = 0.31 cm^{-1}/(MV/cm), and $\Delta\vec{\mu}_{FEC}$ = 0.57 cm^{-1}/(MV/cm). We then leverage two electrostatic expressions to converge upon an angle-dependent equilibrium (open circuit) interfacial field for archetypal Li-ion battery electrode/electrolyte junctions. Based upon this convergence model, which depends explicitly on the dielectric function of the electrode interface and the projection of the field onto the dipole axis of the C=O group, we estimate local fields spanning approximately 30-50 MV/cm at $LiCoO_2$ and 84-132 MV/cm at graphite interfaces. This quantitative benchmark of $\Delta\vec{\mu}$ for some of the most commonly used electrolyte solvents lays the groundwork for proofing future electrostatic materials design strategies, for example, by controlling electrochemical reaction dynamics using extrinsic interface modifiers.

5.2 Introduction

Variations in local electric fields appear to control reactivity in chemical systems ranging from biochemistry to materials science.[131, 137, 315-318] In the context of energy conversion and storage materials, quantifying the field magnitudes at the interfaces of photoelectrodes[146, 148, 151-153] and electrocatalysts[319-320] by spectroscopic methods has provided both fundamental scientific understanding of material properties and new design principles for advanced device applications. Interface electrostatics are also known to play a major role in the viability of next-generation battery electrode materials. Examples include, among others,

suppressed dendrite formation in Li metal batteries using monovalent cations,[321-322] monitoring intercalation in metal-oxide cathodes,[323] mitigating active material dissolution in Li-S composites,[324] and interpreting capacity losses.[325] While computational predictions yield estimated field strengths at the electrode/electrolyte junction in the MV/cm range,[77, 105, 326-328] the interfacial electric fields in archetypical rechargeable battery systems have yet to be experimentally quantified.

Spectroscopically-active reference materials, calibrated against fields of known value, have been key to quantifying local electric fields at several model electrode interfaces. For example, recent work by Dawlaty et al.,[329] Lian et al.,[139] and Hildebrandt et al.[330-331] quantified local fields at model electrochemical interfaces by monitoring the vibrational frequency shift in response to applied electric field magnitudes on the order of several MV/cm for nitrile moieties tethered on gold electrode surfaces. Furthermore, the Dawlaty group has proposed a formalism to estimate the field strength at electrode interfaces that accounts for the presence of an image dipole within an electrode as a way to more accurately represent the dielectric anisotropy experienced by the molecule at the electrode/electrolyte junction.[141] It is worth noting that this treatment relies on knowing the vibrational reporter's sensitivity to electric fields under the conditions described by the Onsager model[332] (isotropic dielectric surrounding a molecule), as well as both the refractive index and dielectric of the molecule of interest. Results separately published by Grey et al.[333] and Somorjai et al.[78] reveal shifts in the vibrational frequency of the C-H stretch of carbonate electrolyte solvents at capacitor and battery electrode interfaces under an applied voltage. Such results highlight the importance of the model proposed by Dawlaty in the context of energy materials. However, the minimal sensitivity of the C-H stretching mode to an electric field tends to limit its versatility in quantifying local field strengths within the electrochemical double layer. A more sensitive vibrational reporter would be ideal to extract such values. More recently, the line shape and peak position of carbonyl (C=O) modes in linear and cyclic carbonates were observed to change near the interface of an electrode as it cycled (i.e. under the influence of local electric fields).[334] The importance of these observations is amplified by the fact that carbonate-based electrolyte formulations are consistently used as workhouse electrochemical platforms in energy storage devices since their physicochemical properties afford a wide parameter space for voltage and temperature optimization.[335-337] Considering the abovementioned changes in vibrational activity of carbonate solvents at material interfaces, here we show that the C=O group of carbonate solvents can serve as a sensitive complementary reporter to gauge interfacial electric field strengths.[132, 338] By analogy to the utility of such measurements applied to other energy material systems,[144-145] we expect these results to provide a powerful lens through which to proof design strategies aimed at exerting kinetic control over electrode/electrolyte compatibility in next-generation electrochemical energy storage systems.

5.3 Background

The interaction between an external applied field and vibrational reporter can be understood on the basis of standard perturbation theory, and is associated with the vibrational Stark effect (VSE).[130-131, 339] Using infrared spectroscopy, one can compare spectra with and without an applied electric field to monitor the VSE response of a reporter moiety by using a technique known as vibrational Stark spectroscopy (VSS).[132, 135] When the relationship between the applied field and response of the vibrational reporter follows a linear trend (as is traditionally observed in VSS for many high frequency local modes) the difference spectrum will correspond to a second derivative of the zero-field peak line shape; this response is depicted in Figures 1a-c. One can then fit the VSS data with a derivative line shape to extract a value of the vibrational mode's sensitivity to the applied field, termed the Stark tuning rate ($\Delta\vec{\mu}$, units in $cm^{-1}/(MV/cm)$).[131, 340] As the response of a vibrational reporter informs on the local field at its position in the active environment, rather than the externally applied field, it is necessary to incorporate a local field correction factor (f). The variable f has no effect on the general line shape of the difference spectrum, but affects the relative determination of $\Delta\vec{\mu}$, resulting in the expression of the tuning rate as $|\Delta\vec{\mu}|f$.[132] Thus, the VSS experiment provides an avenue to qualify the mechanism of interaction between fields and a molecular group. However, complementary experimental techniques are required to extract an unambiguous quantitative value of $\Delta\vec{\mu}$.

One approach to quantify $\Delta\vec{\mu}$ of a reporter moiety is vibrational solvatochromism, combined with molecular dynamics (MD) simulations that provides the absolute electric fields experienced by a solute in a series of solvents with varying dielectric constants.[341] In contrast to VSS, the solvatochromic shifts are measured in the absence of an externally applied field and the local field factor is thus excluded. The systematic red-shift of the vibrational reporter in solvents of increasing solvent fields provides a field-frequency calibration curve that allows one to directly map an observed peak position to a solvent field in condensed phase systems. This provides an avenue to determine electrostatic fields, for example, within the active site of an enzyme. In our case, we are particularly interested in the magnitude of electric fields established at electrode interfaces.

Herein, we provide Stark tuning rates for the C=O groups of the common battery electrolyte solvents (Figure 1d) diethyl carbonate (DEC), ethylene carbonate (EC), and fluoroethylene carbonate (FEC) using both VSS and the solvatochromic field-frequency calibration approaches. We see that under the separate influence of solvent and applied electric fields commensurate with those suggested in computational studies of electrode interfaces,[342-343] the sensitivity of the C=O stretch is unique for each carbonate and follows the linear Stark effect illustrated in Figure 1. In particular, we demonstrate that the sensitivity of the C=O mode (0.37 $cm^{-1}/(MV/cm)$) as an electrode interfacial field reporter for DEC is close to three times more sensitive than its C-H mode (<0.15 $cm^{-1}/(MV/cm)$).[78] As an example of the utility of our findings, we estimate the

magnitude of the interfacial field at an archetypal battery electrode/electrolyte junctions from literature to be in the MV/cm range at open circuit potential. Our estimates are based on electrostatic interactions with molecules described with the VSE model and the Onsager-like model/reaction field theory for the metal-dielectric interface developed by Dawlaty.[141] In effect, these results present a framework for quantifying local electric fields at interfaces relevant to energy storage materials.

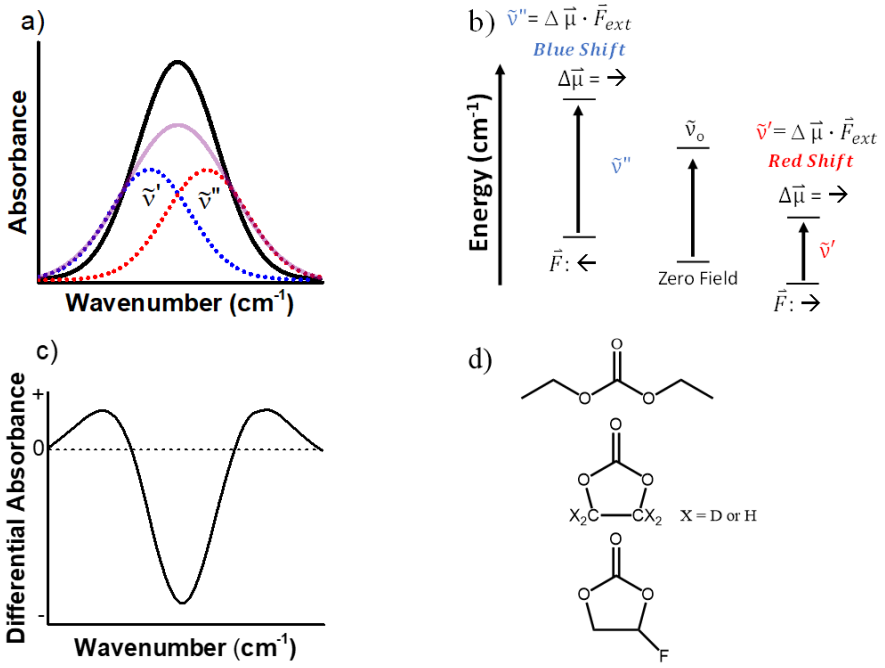

Figure 1. (a) An electric field applied to an isotropic frozen solution leads to broadening of the vibrational mode due to an equal proportion of molecules oriented parallel and antiparallel to the applied electric field vector, thereby exerting either a stabilizing or destabilizing field on the bond vector, changing the resulting vibrational frequency as depicted in Figure (b). Arrows denote the case of parallel and antiparallel orientation of the field with respect to the bond dipoles, resulting in either a red shift (parallel) or blue shift (antiparallel). The difference between the field-on and field-off spectra yields a line shape that is congruent with a second derivative of the zero-field spectrum (c). The compounds analyzed in this study: ethylene carbonate (EC), fluoroethylene carbonate (FEC) and diethyl carbonate (DEC) are shown in panel (d).

5.4 Results:

To determine whether the linear Stark effect manifests among all carbonate solvents, we first utilized vibrational Stark spectroscopy (VSS) to measure spectra of each carbonate solvent in a frozen glass and calibrated their sensitivities to an externally applied electric field. As observed in Figure 2a, the C=O stretch of DEC absorbs at ~1740 cm^{-1} in the absence of an applied external electric field. With the application of an external electric field (Figure 2b), the resulting Stark spectrum exhibits a line shape resembling the second derivative of the zero-field absorption spectrum in accord with Figure 1, suggesting that the primary mechanism of response to an electric field is via the linear Stark effect ($\Delta\vec{\mu}$). The magnitude of the VSE

scales with the product of the magnitude of the tuning rate $|\Delta\vec{\mu}_{DEC}|$ and the local field correction factor *f*, which yields a combined value of 1.06 cm^{-1}/(MV/cm).

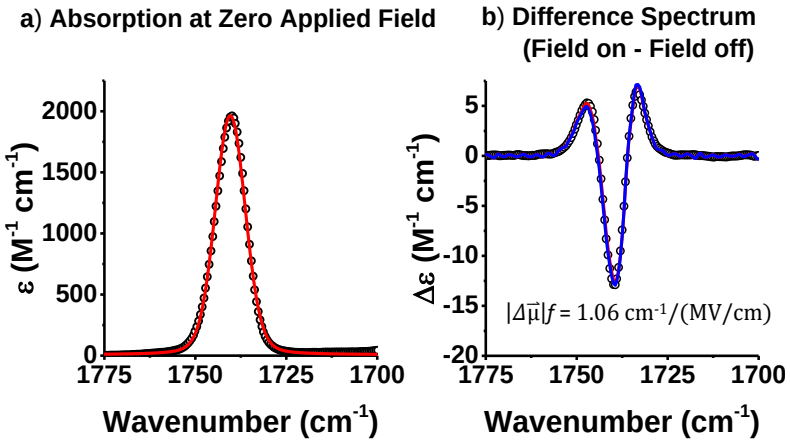

Figure 2. (a) FTIR spectra of 100 mM DEC in 2-MeTHF at 77K with fits to the carbonyl under no applied field. (b) Stark spectrum of DEC under the application of an external field, scaled to 1 MV/cm. The best fit (red trace) and 2nd derivative (blue trace), as well as the product of $\Delta\vec{\mu}$ and *f*, are included.

Because linear carbonate solvents are often combined into an electrolyte blend with cyclic carbonates, we expand this work to include field calibrations for the C=O group in FEC and EC. In the absence of an applied field, peaks and their corresponding fits to the C=O mode of FEC, EC and 98 %-deuterated EC (D_4-EC, for peak assignment) within the 2-methyltetrahydrofuran glassy matrix (Figure 3, a-c) are consistent with literature values.[344] Spectra for EC and FEC both exhibit shoulders adjacent to their fundamental C=O mode. We observe two peaks in the EC spectrum, one at 1775 and another at 1790 cm^{-1}. In FEC, two modes are observed at 1805 and 1835 cm^{-1}. Based on previous characterization of cyclic carbonate molecules and their halogenated derivatives with vibrational spectroscopy, we associate the C=O modes of EC and FEC to be at 1790 and 1825 cm^{-1}, respectively. Spectral overtone peaks from skeletal breathing modes in the 800-900 cm^{-1} range appear near the C=O modes of EC and FEC due to Fermi resonance.[345-346] Replacing 98 % of the hydrogen atoms on EC with deuterium significantly lowers the amplitude of Fermi resonance, as demonstrated by comparing Figures 3b and 3c.

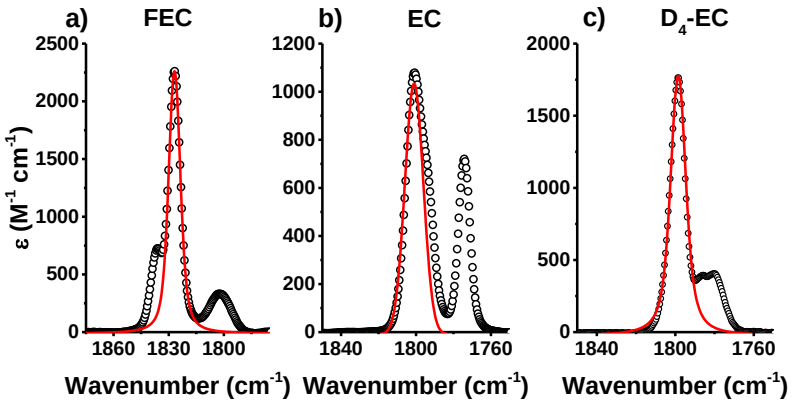

Figure 3. FTIR spectra of 100 mM FEC, EC and D_4-EC in 2-MeTHF at 77K with fits (red traces) to the carbonyl mode of EC and FEC (black dots). The Fermi resonance remains in the D_4-EC spectrum, but with considerably smaller amplitude relative to the non-deuterated EC.

We display Stark tuning rates obtained for the cyclic carbonates using VSS in Figure 4. Again, we observe that under the influence of an externally applied electric field, the resulting spectra exhibit primarily second derivative line shapes, indicative of the vibrational frequency shift arising primarily from the linear Stark effect.[130, 338] The Stark spectrum of non-deuterated EC suffers from significant interference from Fermi resonance (Figure C1), resulting in a qualitatively poor fit. Despite this, the calculated product $|\Delta\vec{\mu}_{EC}|f$ is similar between EC and D_4-EC. This is in agreement with previous observations that although overtone/Fermi resonant modes undergo changes when subjected to an applied electric field, the influence of Fermi coupling on the determined Stark tuning rates is negligible and primarily manifests in imperfect spectral fitting rather than acting upon a physical mechanism that would perturb the sensitivity to an electric field.[340]

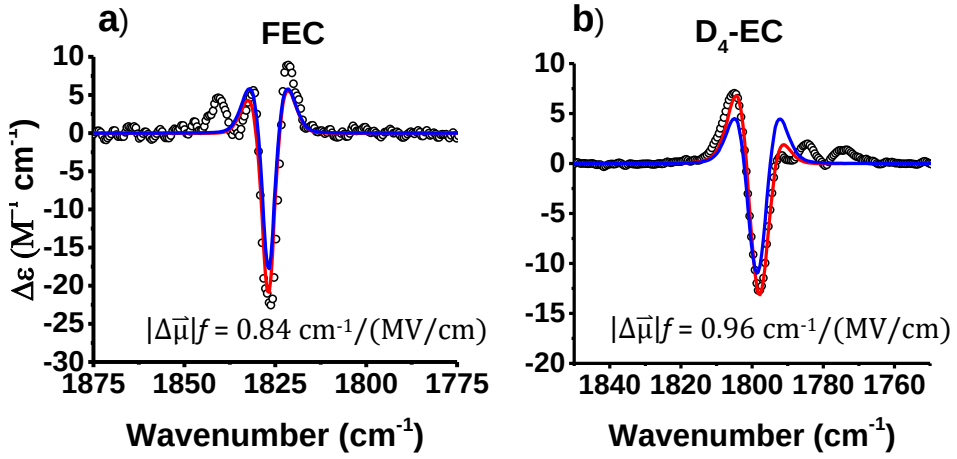

Figure 4. Results of VSS: raw data (black dots) for FEC (Figure a) and D_4-EC (Figure b), scaled to an applied field of 1 MV/cm. The line of best fit (red trace) for all VSS spectra closely matches the second

derivative line shape (blue line) of the absorbance spectra without an applied field. The Stark tuning rates are listed at the bottom of each panel as the product of $|\Delta\vec{\mu}|$ and *f*.

As an alternative approach, the Stark tuning rate ($\Delta\vec{\mu}$) can be determined by combining vibrational solvatochromism measurements with molecular dynamics (MD) simulations to calculate the electric field exerted by the solvent onto the C=O bond dipole. The resulting electric field-frequency calibration curves do not propagate the local field correction factor, *f*, since there is no externally applied field as in the results from the previous section.[347] Accordingly, we obtain precise values of the Stark tuning rates ($\Delta\vec{\mu}$) for DEC, EC, and FEC, which are lower than the apparent Stark tuning rates from the VSS experiments (i.e. $f > 1$). As anticipated, Figure 5 demonstrates that the Stark tuning rates for all carbonate solvents are lower than those obtained with VSS. The values of *f* in VSS for each carbonate molecule in the 2-MeTHF matrix are provided in Table 1 and fall within the generally observed range of values for carbonyls and nitriles.[330, 338, 348] It is noteworthy that FEC exhibits a markedly lower correction factor, which may be due to subtle differences in the solvation environment at 77K; the molecular structure of the three carbonates are likely to affect the subsequent solvent organization around the solute. As discussed above, while the Fermi resonance affects the C=O peak position and intensity, attempts to utilize a perturbation model to suppress this interference[349-352] result in corrected frequencies with a lower coefficient of determination (R^2) when fit by linear regression (Figure C2, Table C3 for absorption values). Expanding the range of solvent fields for DEC does not change the Stark tuning rate significantly (Figure C4), indicating that the number of data points in Figure 5 is sufficient to calculate reliable Stark tuning rates.

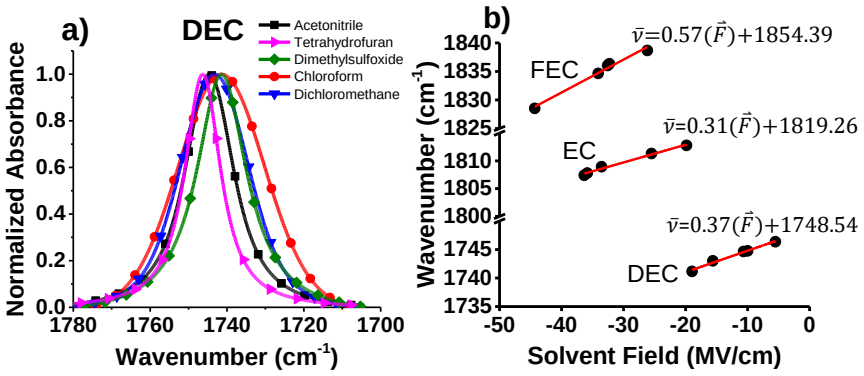

Figure 5. (a) Example of solvatochromic results from calibration of the C=O group in DEC. (b) Electric field-frequency calibration curve for FEC, EC, and DEC. A linear relationship between solvent field and peak position is observed, consistent with the linear Stark effect, and the slope corresponds to $|\Delta\vec{\mu}|$, in units of $cm^{-1}/(MV/cm)$. Frequencies and calculated electric fields are presented for all carbonates and solvents in Tables C1 and C2, respectively.

Electrolyte Solvent	$\lvert\Delta\vec{\mu}\rvert$ (cm^{-1}/(MV/cm))	f	$\lvert\Delta\vec{\mu}\rvert f$ (cm^{-1}/(MV/cm))
DEC	0.37	2.86	1.05
EC (D_4)	0.31	3.09	0.96
FEC	0.57	1.47	0.84

Table 1: Summary of Stark tuning rates ($|\Delta\vec{\mu}|$ and $|\Delta\vec{\mu}|f$), determined herein, and local field correction factors (f) among all carbonate electrolyte solvents. Local field corrections factors are determined from comparison of the Stark tuning rates measured from vibrational Stark spectroscopy ($|\Delta\vec{\mu}|f$) and the field-frequency calibration ($|\Delta\vec{\mu}|$) as shown in Figure 5b.

With the values of $\Delta\vec{\mu}$ for these electrolyte solvents in hand, we describe examples of their application to quantify fields at cathode and anode electrode interfaces relevant to electrochemical energy storage. Beginning with archetypal cathode interfaces, it has been previously determined that the C=O group in DEC at the interface of $LiCoO_2$ is red shifted to 1737 cm^{-1} at open circuit.[72] The equilibration process between these materials includes the formation of a space charge layer by solvation of Li^+ from $LiCoO_2$ by DEC,[353] establishing an electrochemical double layer at the electrode/electrolyte junction; it is the field confined at this solid/liquid junction which makes it compelling to quantify $\Delta\vec{\mu}$ for organic carbonates as possible *in situ* interfacial electric field reporters. These spectroscopic results were observed using vibrational sum frequency generation (SFG), the same interface-sensitive spectroscopic technique employed to observe the vibrational Stark shifts (and therefore electrostatic fields) at operating electrochemical interfaces of battery materials.[78] Furthermore, a redshift of the C=O has been observed within the multilayer structure extending out from the $LiCoO_2$/DEC junction at a resting potential,[354] but to a lesser magnitude, indicating the possibility of a decaying potential drop. The absorption of neat DEC solvent appears at 1746.4 cm^{-1} (Figure C5b), while the gas-phase peak appears at 1756 cm^{-1}.[355] As equilibrium with carbonate solvents at lithiated interfaces has been described to include electrostatic processes,[354, 356-358] we leverage the above values in Table 1 to the VSE model (Eq. 1) and compare with an Onsager-like interfacial model proposed by Dawlaty et al. (Eqs. 2 and 3) to calculate the magnitude of the electrostatic field. Since we have observed that the linear Stark effect manifests among all the carbonate solvents, the peak shift can be interpreted as:

$$\Delta\bar{\nu} = -f|\Delta\vec{\mu}| \cdot \vec{F}_{C=O} = -f|\Delta\vec{\mu}|\left|\vec{F}_{C=O}\right| = -f|\Delta\vec{\mu}|\left|\vec{F}_{int}\right|\cos\beta \quad \text{(Eq. 1)}$$

Where $\Delta\bar{\nu}$ is the observed shift in peak position of the C=O group between the gas-phase (representing zero field) and at the electrode interface,[72] $\Delta\vec{\mu}$ is the Stark tuning rate that could be either from the VSS or field frequency calibration; the former would propagate the local field correction factor (f) as included, while β is the angle between the electrostatic field, $\left|\vec{F}_{int}\right|$ (expected to be from the $LiCoO_2$ electrode

interface), and the field projected onto the C=O, $\vec{F}_{C=O}$, through the C=O's $\Delta\vec{\mu}$. Inspired by recent hypotheses that the tilt angle (β) of electrolyte solvents at electrode interfaces have an influence on Li^+ transport and cycling efficiency of electrode materials,[73, 199] it may be useful to connect the angle-dependent electrostatic fields sensed by the C=O group $\left|\vec{F}_{C=O}\right|$ at an electrode surface in this work to quantify this effect in future studies. The transition dipole moment and $\Delta\vec{\mu}$ are generally expected to be colinear, which has been confirmed in several cases.[338, 347] Since the transition dipole for a symmetric stretching mode lies parallel to the oscillator bond axis, $\Delta\vec{\mu}$ can be assumed to be parallel to the C=O bond. Therefore, as the local electrostatic field sensed by the C=O probe ($\left|\vec{F}_{C=O}\right|$) can be quantified from the frequency shift of -19 cm^{-1} in the VSE (as described by Eq. 1), the absolute interfacial field ($\left|\vec{F}_{int}\right|$) may be determined if the tilt angle between the C=O bond axis and the surface normal is known. As such, $\left|\vec{F}_{int}\right|\cos(\beta)$ represents the orientation-dependent electrostatic field sensed by the C=O group, at an electrode interface. The field experienced along the C=O bond of DEC can be calculated from Eq. 1 to fall within a range of values that depends on the contribution of *f*. For example, implementing the field-frequency calibrated value of $|\Delta\vec{\mu}_{DEC}|$ in Table 1 results in $\left|\vec{F}_{int}\right|\cos(\beta)$ = 51.6 MV/cm registered by the C=O group, or more generally $\left|\vec{F}_{int}\right|\cos(\beta)=\frac{51.6}{f}$ MV/cm, which yields an interfacial field of 18 MV/cm when propagating the Stark tuning rate from VSS (Table 1).

A separate estimate of electrostatic fields at an electrode interface can be calculated by an interfacial Onsager model,[141] which more formally describes the electrostatic field within an electrochemical double layer at the electrode/electrolyte junction. In contrast to Eq. 1, the interfacial Onsager model incorporates the field projection specifically from an electrode surface, confined over a finite length. For dipoles oriented perpendicular to an electrode interface (β = 0°), values of $\left|\vec{F}_{int}\right|$ with this model are calculated by the following equation:

$$\left|\vec{F}_{int}\right|(\varepsilon) = \frac{2\vec{\mu}}{\pi\epsilon_0 l^3}\left[\frac{(n^2+2)(1+\zeta(\varepsilon))}{3n^2+9-(n^2-1)\zeta(\varepsilon)}\right] \qquad \text{(Eq. 2)}$$

Where $\vec{\mu}$ represents the dipole moment of DEC (1.07D),[359] $\zeta(\varepsilon)$ an infinite sum representing the potential profile induced by the dielectric (ε = 2.83),[360] n the refractive index of DEC (n= 1.68, obtained via $\sqrt{\varepsilon}$), and l is the cavity length.[361-362] Under the assumption that the electrostatic field drop is over a length $l = 2a$, where a is the C=O bond length (1.22 Å), Eq. 2 yields $\left|\vec{F}_{int}\right|$ = 83 MV/cm. As the solutions to calculate $\left|\vec{F}_{int}\right|$ between Eq. 1 (18-51.6 MV/cm) and 2 (83 MV/cm) do not converge, we quantitatively assess possible reasons below.

As previously mentioned, a concept distinguishing Eq. 2 from Eq. 1 is the incorporation of a field projected by an electrode interface over a finite distance. Thus, the possibility of a different cavity length would change the overall magnitude of $\left|\vec{F}_{int}\right|$ calculated in Eq. 2. Additionally, it has been consistently observed that carbonate solvents at electrode interfaces adopt preferential orientations.[72-73, 197] To account for these effects, a more general version of Eq. 2 has been derived[141] for arbitrary dipole orientations:

$$\left|\vec{F}_{int}(\varepsilon)\right| = \frac{2\vec{\mu}}{\pi\epsilon_0 l^3}\left[\frac{(n^2+2)(1+0.577\zeta(\varepsilon)+(1+1.4226\zeta(\varepsilon))\cos^2\beta))}{7n^2+17-(n^2-1)(0.577\zeta(\varepsilon)+(1+1.4226\zeta(\varepsilon))\cos^2\beta)}\right] \quad \text{(Eq. 3)}$$

Where all parameters are defined as in Eq. 2, with the addition of β representing the dipole tilt angle relative the surface normal. Figure 6 shows the dependence of Eq. 1 on the tilt angle (red line and pink region) and $\left|\vec{F}_{int}(\varepsilon)\right|$ for Eq. 3 (blue). The pink region further expresses how Eq. 1 shifts for a range of *f* values. A lower limit for *f* is 1, while the correction factor for DEC based on comparison of VSS and field-frequency calibration (Table 1, *f* = 2.86) represents the upper boundary. As previously measured values of $\Delta\vec{\mu}$ appear to suffer from a local field factor *f*,[141, 363] we implement a simple estimate[131] of *f* (*f* = (ε + 2)/3 = 1.61) within the illustrated range of values in Fig. 6 to estimate an intermediate between the boundaries of *f*=1 and *f*=2.86 and highlight it with a red line. The blue curves show Eq. 3 with three different cavity lengths, $l = 2a$, with a being 1.22 Å, 1.51 Å, and 2.05 Å. The latter represents the maximum cavity length, beyond which the two methods do not converge for any tilt angle. For shorter cavity lengths, Eq. 3 converges with Eq. 1 and Figure 6 highlights two such cases with dashed lines, under the assumption that *f* = 1.61. When a = 1.22 Å, the extracted values for the electrostatic field and β are 52 MV/cm and 52°, while a = 1.51 Å yields 37 MV/cm and 31°. Although the absolute orientation of DEC on the $LiCoO_2$ surface is not known, dimethyl carbonate (DMC) has been observed to orient preferentially on $LiCoO_2$ and the tilt angle on carbon surfaces have been measured as approximately 34°.[72, 197] Considering these observations for DMC, a tilt angle within 31° to 52° is reasonable for DEC on $LiCoO_2$. Further refinements of the cavity length and *f* values may yield additional precision in estimating the local electrostatic field and tilt angle (β). While the overall magnitudes of the fields will be affected by the choice of *f*, when comparing *among* a given carbonate solvent, these changes will at least be self-consistent and can be easily propagated into the uncertainty of the local field factor if desired. The values of optical constants ε and *n* (obtained from ellipsometry, see Figure C5) may be used to calculate different values of *f* and more precisely validate the orientation of DEC on electrode surfaces with mathematical treatments used for interface-sensitive spectroscopy.[364]

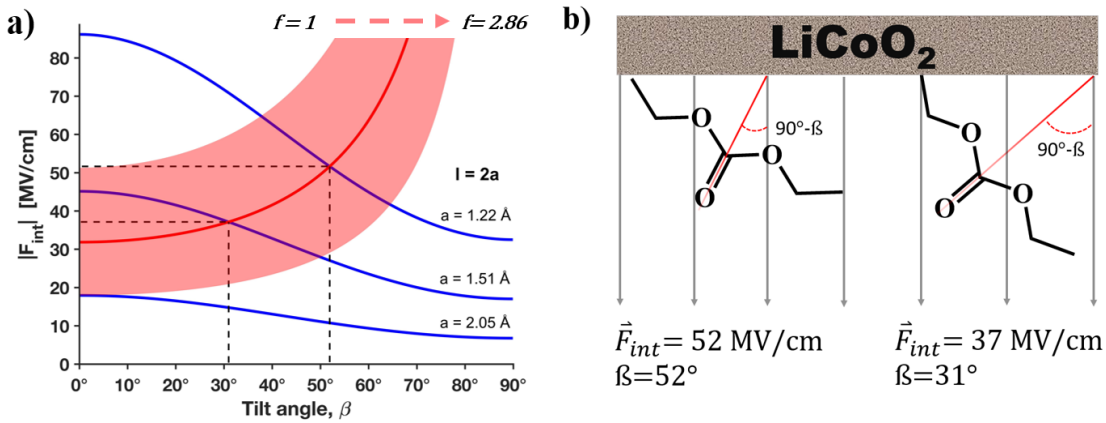

Figure 6. (a) The distribution of interfacial electrostatic field values between Eq. 1 (red trace) and Eq. 3 (blue trace) converge at 37-52 MV/cm with tilt angles (ß) between 31°-52° from surface normal (as seen in Figure b). An estimate of f = 1.61 determined by previous reports[131] as (ε+2)/3, produces the solid line in the range of fields produced by boundaries in Equation 1. Increasing the cavity length l in Eq. 3 to 2.44 Å corresponds to $\left|\vec{F}_{int}(\varepsilon)\right|$ = 52 MV/cm as a convergence point with Eq. 1; raising it to 3.02 Å corresponds to $\left|\vec{F}_{int}(\varepsilon)\right|$= 31 MV/cm. A value of 4.10 Å is the largest cavity length that would converge with the maximum f (2.86) incorporated into Eq. 1.

The EC molecule has also been experimentally observed to shift in absorption energy on graphite interfaces, where the equilibration mechanism was suggested to be an effect of electrostatic fields.[365] Previous analysis of chemical phenomena within the double layer of the graphite electrode/electrolyte junction suggested the electrostatic potential comprises a majority of the interfacial forces in operating batteries.[366] Extending our protocol above to calculate interface fields of a common anode material at open circuit, Figure S6 shows that interfacial fields between ~84-130 MV/cm are present at a tilt angle between approximately 40°-60°. While there does not appear to be any reference of the orientation of EC on graphite, a structurally similar cyclic carbonate (vinylene carbonate, distinguished from EC by a double bond between adjacent carbons) orients at approximately 53° on graphite surfaces.[197] Under non-equilibrium conditions (i.e. charging/discharging of the battery), the intercalation of Li^+ into graphite has been estimated to require an electrostatic field of 360 MV/cm at the interface.[79]

A few assumptions are inherent in the calculations above, for instance that the carbonates exhibit one preferred orientation. In cases where the molecules exhibit a bimodal distribution (which has indeed been demonstrated for a few carbonate systems),[197] Eq. 3 has to be expanded to include the contributions from each orientation. The total interfacial field must further be consistent with the parameters in Eq. 2 for each orientation-dependent peak position observed experimentally. The preceding narrative also assumes that electrostatic forces are the only contributions to electrolyte dynamics on cathode and anode electrode surfaces, however, chemisorption and physisorption processes are also known to occur at the electrode/electrolyte junction.[354, 356, 358, 367] Such forces may modulate the overall magnitude of the

electrostatic contributions quantified above, requiring evaluation on a case by case basis. Nevertheless, spectroscopic evidence demonstrates that electrostatic fields appear present at interfaces relevant to electrochemical energy storage.[78] This report provides the Stark tuning rates for more sensitive reporters of the local fields under operating conditions, when compared to the previously used C-H stretching vibrations. Additionally, the combination of several experimental methods and the convergence with electrostatic models provide an interval over which the interfacial electric field in the MV/cm range appear to be physically meaningful. Quantifying chemisorption and physisorption phenomena will lend further accuracy to the field and tilt angle estimates that this method can provide. We anticipate that these results will yield a quantitative benchmark for understanding the dynamic response of new and existing electrode/electrolyte junctions, for example, in using *operando* vibrational spectroscopy to monitor the evolution of interfacial electric fields in electrochemical cells. For such investigations based on vibrational sum-frequency generation spectroscopy, it is important to note that the fields measured in this work are of the same order of magnitude as the ratio between $\chi^{(2)}$ and $\chi^{(3)}$ (i.e. 10^9 to 10^{10}).[227] This means that 3rd-order effects may contribute significantly to the signal, which can affect the data interpretation. For example, mixing of $\chi^{(2)}$ and $\chi^{(3)}$ can have severe effects on the signal strength and line shape, depending on their relative phases, which are related to the SFG coherence length and the Debye screening length.[368]

5.5 Conclusion

We have demonstrated that the IR absorption of carbonyls in carbonate-based electrolyte solvents can be sensitive electric field reporters at electrochemical interfaces relevant for energy storage devices. Our approach combines the complementary techniques of vibrational Stark spectroscopy (VSS) and vibrational solvatochromism. Mapping vibrational frequencies from vibrational solvatochromism to electric fields calculated using MD simulations, we have obtained a direct field-frequency calibration to quantify the absolute electric fields that are sensed by these solvent molecules at the electrode/electrolyte junction. Using these approaches, the C=O group's response to an electric field is observed to be consistent with the linear Stark effect for diethyl carbonate, ethylene carbonate, and fluoroethylene carbonate. Applying the Stark tuning rates of DEC and EC to vibrational characterization of model Li-ion battery junctions, local fields on the order of 10-10^2 MV/cm are estimated from a convergence between two separate models for solving electrostatic fields.

These findings lend a tractable metric to quantify the electrostatic forces at electrode interfaces under dynamic[78, 333] or resting[197, 369] potentials. From a technological standpoint, a thorough understanding of the field at the electrode/electrolyte junction may ultimately lead to new design principles for energy storage materials in a manner similar to that proposed recently by Leung et al. to widen the electrochemical stability

window for archetypal lithium-ion battery electrolyte solvents by controlling the electrostatics at the liquid/solid junction using dipole-modified interfaces.[328] The concept of modulating the electric fields across the electrode/electrolyte junction has been adopted in other electrochemical systems,[149, 370] however, transferring such a platform to electrochemical energy storage materials would require an intimate understanding of how an extrinsic interfacial chemical modifier controls the local electric field within the operating device. Such strategies would likely provide new avenues for controlling the faradaic efficiency of batteries; improving the ratio of charge extracted to charge injected in active electrode materials to help mitigate deleterious interfacial side reactions.[270, 371]

Most recently, compelling next-generation electrode chemistries have exhibited shifts in the overpotential of redox reactions.[372-373] These results provide further evidence that extrinsic control of interfacial electrostatic interactions can provide a strategic design space for controlling redox activity. While the research groups cited were able to successfully demonstrate the relevance of this concept, they acknowledge the value of the interfacial field is unknown. Therefore, we anticipate that the Stark tuning rates and field-frequency calibration curves of the workhorse battery electrolyte solvents that we have reported here will provide a platform for experimentally characterizing these interface fields and possibly lead to controlling their magnitude in active electrochemical devices.

5.6 Appendix C:

Experimental methods and supporting information for chapter 5

5.7 Acknowledgements:

This work was performed, in part, at the Center for Integrated Nanotechnologies, an Office of Science User Facility operated for the U.S. Department of Energy (DOE) Office of Science. Sandia National Laboratories is a multi-mission laboratory managed and operated by National Technology and Engineering Solutions of Sandia, LLC., a wholly owned subsidiary of Honeywell International, Inc., for the U.S. DOE's National Nuclear Security Administration under contract DE-NA-0003525. The views expressed in the article do not necessarily represent the views of the U.S. DOE or the United States Government.

5.8 References:

72. Yu, L.; Liu, H.; Wang, Y.; Kuwata, N.; Osawa, M.; Kawamura, J.; Ye, S., Preferential Adsorption of Solvents on the Cathode Surface of Lithium Ion Batteries. *Angew. Chem. Int. Ed.* **2013,** *52* (22), 5753-5756.
73. Horowitz, Y.; Han, H.-L.; Soto, F. A.; Ralston, W.; Balbuena, P. B.; Somorjai, G. A., Fluoroethylene Carbonate as a Directing Agent in Amorphous Silicon Anodes - Electrolyte

Interface Structure Probed by Sum Frequency Vibrational Spectroscopy and Ab-initio Molecular Dynamics. *Nano Lett.* **2018**. *18* (2), 1145-1151.
77. Kumar, N.; Siegel, D. J., Interface-Induced Renormalization of Electrolyte Energy Levels in Magnesium Batteries. *J Phys Chem Lett* **2016,** *7* (5), 874-81.
78. Horowitz, Y.; Han, H.-L.; Somorjai, G. A., Identifying the Decomposition of Diethyl Carbonate in Binary Electrolyte Solution in Contact with Silicon Anodes - A Sum Frequency Generation Vibrational Spectroscopy Study. *Industrial & Engineering Chemistry Research* **2018**, *57* (5) 1480-1486
79. Márquez, A.; Balbuena, P. B., Molecular Dynamics Study of Graphite/Electrolyte Interfaces. *J. Electrochem. Soc.* **2001,** *148* (6), A624-A635.
105. Luck, J.; Latz, A., Theory of reactions at electrified interfaces. *PCCP* **2016,** *18* (27), 17799-17804.
130. Boxer, S. G., Stark Realities. *The J. Phys. Chem. B* **2009,** *113* (10), 2972-2983.
131. Boxer, S. G.; Bublitz, G. U., Stark spectroscopy: Applications in Chemistry, Biology, and Materials Science. *Annu. Rev. Phys. Chem.* **1997,** *48*, 213–242.
132. Fried, S. D.; Boxer, S. G., Measuring electric fields and noncovalent interactions using the vibrational stark effect. *Acc. Chem. Res.* **2015,** *48* (4), 998-1006.
135. Andrews, S. S.; Boxer, S. G., A liquid nitrogen immersion cryostat for optical measurements. *Rev. Sci. Instrum.* **2000,** *71* (9), 3567.
137. Fried, S. D.; Bagchi, S.; Boxer, S. G., Extreme electric fields power catalysis in the active site of ketosteroid isomerase. *Science* **2014,** *346* (6216), 1510.
139. Ge, A.; Videla, P.; Lee, G. L.; Rudshteyn, B.; Song, J.; Kubiak, C. P.; Batista, V. S.; Lian, T., Interfacial Structure and Electric Field Probed by in situ Electrochemical Vibrational Stark Effect Spectroscopy and Computational Modeling. *The J. Phys. Chem. C* **2017**.
141. Sorenson, S. A.; Patrow, J. G.; Dawlaty, J. M., Solvation Reaction Field at the Interface Measured by Vibrational Sum Frequency Generation Spectroscopy. *J. Am. Chem. Soc.* **2017,** *139* (6), 2369-2378.
144. O'Donnell, R. M.; Ardo, S.; Meyer, G. J., Charge-Screening Kinetics at Sensitized TiO_2 Interfaces. *The J. Phys. Chem. Lett.* **2013,** *4* (17), 2817-2821.
145. O'Donnell, R. M.; Sampaio, R. N.; Barr, T. J.; Meyer, G. J., Electric Fields and Charge Screening in Dye Sensitized Mesoporous Nanocrystalline TiO_2 Thin Films. *The J. Phys. Chem. C* **2014,** *118* (30), 16976-16986.
146. Sampaio, R. N.; O'Donnell, R. M.; Barr, T. J.; Meyer, G. J., Electric Fields Control $TiO_2(e–) + I_3^–$ → Charge Recombination in Dye-Sensitized Solar Cells. *The J. Phys. Chem. Lett.* **2014,** *5* (18), 3265-3268.
148. Cappel, U. B.; Feldt, S. M.; Schöneboom, J.; Hagfeldt, A.; Boschloo, G., The Influence of Local Electric Fields on Photoinduced Absorption in Dye-Sensitized Solar Cells. *J. Am. Chem. Soc.* **2010,** *132* (26), 9096-9101.
149. Yang, W.; Pazoki, M.; Eriksson, A. I. K.; Hao, Y.; Boschloo, G., A key discovery at the TiO_2/dye/electrolyte interface: slow local charge compensation and a reversible electric field. *PCCP* **2015,** *17* (26), 16744-16751.
151. Yang, W.; Hao, Y.; Vlachopoulos, N.; Eriksson, A. I. K.; Boschloo, G., Studies on the Interfacial Electric Field and Stark Effect at the TiO_2/Dye/Electrolyte Interface. *The J. Phys. Chem. C* **2016,** *120* (39), 22215-22224.
152. Yang, W.; Vlachopoulos, N.; Boschloo, G., Impact of Local Electric Fields on Charge-Transfer Processes at the TiO_2/Dye/Electrolyte Interface. *ACS Energy Letters* **2017,** *2* (1), 161-167.
153. Pazoki, M.; Jacobsson, T. J.; Kullgren, J.; Johansson, E. M. J.; Hagfeldt, A.; Boschloo, G.; Edvinsson, T., Photoinduced Stark Effects and Mechanism of Ion Displacement in Perovskite Solar Cell Materials. *ACS Nano* **2017,** *11* (3), 2823-2834.

197. Peng, Q.; Liu, H.; Ye, S., Adsorption of organic carbonate solvents on a carbon surface probed by sum frequency generation (SFG) vibrational spectroscopy. *J. Electroanal. Chem.* **2016**, 800, 134-143.
199. Horowitz, Y.; Han, H.-L.; Ralston, W. T.; de Araujo, J. R.; Kreidler, E.; Brooks, C.; Somorjai, G. A., Fluorinated End-Groups in Electrolytes Induce Ordered Electrolyte/Anode Interface Even at Open-Circuit Potential as Revealed by Sum Frequency Generation Vibrational Spectroscopy. *Adv. Energy Mater.* **2017**, 1602060.
227. Koelsch, P.; Muglali, M. I.; Rohwerder, M.; Erbe, A., Third-order effects in resonant sum-frequency-generation signals at electrified metal/liquid interfaces. *J. Opt. Soc. Am. B* **2013,** *30* (1), 219-223.
270. Verma, P.; Maire, P.; Novák, P., A review of the features and analyses of the solid electrolyte interphase in Li-ion batteries. *Electrochim. Acta* **2010,** *55* (22), 6332-6341.
315. Fried, S. D.; Boxer, S. G., Electric Fields and Enzyme Catalysis. *Annu. Rev. Biochem* **2017,** *86* (1), 387-415.
316. Flatté, M. E.; Kornyshev, A. A.; Urbakh, M., Giant Stark effect in quantum dots at liquid/liquid interfaces: A new option for tunable optical filters. *Proceedings of the National Academy of Sciences* **2008,** *105* (47), 18212.
317. Sim, S.; Lee, D.; Noh, M.; Cha, S.; Soh, C. H.; Sung, J. H.; Jo, M.-H.; Choi, H., Selectively tunable optical Stark effect of anisotropic excitons in atomically thin ReS_2. *Nat. Comm.* **2016,** *7*, 13569.
318. Liu, Y.; Qiu, Z.; Carvalho, A.; Bao, Y.; Xu, H.; Tan, S. J. R.; Liu, W.; Castro Neto, A. H.; Loh, K. P.; Lu, J., Gate-Tunable Giant Stark Effect in Few-Layer Black Phosphorus. *Nano Lett.* **2017,** *17* (3), 1970-1977.
319. Sorte, E. G.; Chen, D.-J.; Tong, Y. J., Dual-Electrode In Situ Infrared Spectroscopy for Fuel Cells. *J. Electrochem. Soc.* **2016,** *163* (4), H3038-H3042.
320. Bo, A.; Sanicharane, S.; Sompalli, B.; Fan, Q.; Gurau, B.; Liu, R.; Smotkin, E. S., In Situ Stark Effects with Inverted Bipolar Peaks for Adsorbed CO on Pt Electrodes in 50 °C Direct Methanol Fuel Cells. *The J. Phys. Chem. B* **2000,** *104* (31), 7377-7381.
321. Ding, F.; Xu, W.; Graff, G. L.; Zhang, J.; Sushko, M. L.; Chen, X.; Shao, Y.; Engelhard, M. H.; Nie, Z.; Xiao, J.; Liu, X.; Sushko, P. V.; Liu, J.; Zhang, J.-G., Dendrite-Free Lithium Deposition via Self-Healing Electrostatic Shield Mechanism. *J. Am. Chem. Soc.* **2013,** *135* (11), 4450-4456.
322. Yoo, D.-J.; Kim, K. J.; Choi, J. W., The Synergistic Effect of Cation and Anion of an Ionic Liquid Additive for Lithium Metal Anodes. *Adv. Energy Mater.* **2018,** *8* (11) 1702744.
323. Li, L.; Steiner, U.; Mahajan, S., Single Nanoparticle SERS Probes of Ion Intercalation in Metal-Oxide Electrodes. *Nano Lett.* **2014,** *14* (2), 495-498.
324. Zhang, L.; Ling, M.; Feng, J.; Liu, G.; Guo, J., Effective electrostatic confinement of polysulfides in lithium/sulfur batteries by a functional binder. *Nano Energy* **2017,** *40*, 559-565.
325. Rangarajan, J., Corona Yank in Edged Cathode Particles for Li-Ion Batteries. *Langmuir* **2016,** *32* (10), 2518-2523.
326. Wang, H.; Varghese, J.; Pilon, L., Simulation of electric double layer capacitors with mesoporous electrodes: Effects of morphology and electrolyte permittivity. *Electrochim. Acta* **2011,** *56* (17), 6189-6197.
327. Wang, Y.; Shan, X.; Wang, S.; Tao, N.; Blanchard, P.-Y.; Hu, K.; Mirkin, M. V., Imaging Local Electric Field Distribution by Plasmonic Impedance Microscopy. *Anal. Chem.* **2016,** *88* (3), 1547-1552.
328. Leung, K.; Leenheer, A., How Voltage Drops Are Manifested by Lithium Ion Configurations at Interfaces and in Thin Films on Battery Electrodes. *The J. Phys. Chem. C* **2015,** *119* (19), 10234-10246.

329. Patrow, J. G.; Sorenson, S. A.; Dawlaty, J. M., Direct Spectroscopic Measurement of Interfacial Electric Fields Near an Electrode Under Polarizing or Current-Carrying Conditions. *The J. Phys. Chem. C* **2017**, *12* (121) 11585-11592.
330. Staffa, J. K.; Lorenz, L.; Stolarski, M.; Murgida, D. H.; Zebger, I.; Utesch, T.; Kozuch, J.; Hildebrandt, P., Determination of the Local Electric Field at Au/SAM Interfaces Using the Vibrational Stark Effect. *The J. Phys. Chem. C* **2017,** *121* (40), 22274-22285.
331. Schkolnik, G.; Salewski, J.; Millo, D.; Zebger, I.; Franzen, S.; Hildebrandt, P., Vibrational stark effect of the electric-field reporter 4-mercaptobenzonitrile as a tool for investigating electrostatics at electrode/SAM/solution interfaces. *Int J Mol Sci* **2012,** *13* (6), 7466-82.
332. Onsager, L., Electric Moments of Molecules in Liquids. *J. Am. Chem. Soc.* **1936,** *58* (8), 1486-1493.
333. Humphreys, E. K.; Casford, M. T. L.; Allan, P. K.; Grey, C. P.; Clarke, S. M., SFG Study of the Potential Dependent Adsorption of the P-Toluenesulfonate Anion at an Activated Carbon/Propylene Carbonate Interface. *The J. Phys. Chem. C* **2017**.
334. Marino, C.; Boulaoued, A.; Fullenwarth, J.; Maurin, D.; Louvain, N.; Bantignies, J.-L.; Stievano, L.; Monconduit, L., Solvation and Dynamics of Lithium Ions in Carbonate-Based Electrolytes during Cycling Followed by Operando Infrared Spectroscopy: The Example of $NiSb_2$, a Typical Negative Conversion-Type Electrode Material for Lithium Batteries. *The J. Phys. Chem. C* **2017,** *121* (48), 26598-26606.
335. Veith, G. M.; Doucet, M.; Sacci, R. L.; Vacaliuc, B.; Baldwin, J. K.; Browning, J. F., Determination of the Solid Electrolyte Interphase Structure Grown on a Silicon Electrode Using a Fluoroethylene Carbonate Additive. *Sci. Rep.* **2017,** *7* (1), 6326.
336. Shi, F.; Song, Z.; Ross, P. N.; Somorjai, G. A.; Ritchie, R. O.; Komvopoulos, K., Failure mechanisms of single-crystal silicon electrodes in lithium-ion batteries. *Nat. Commun.* **2016,** *7*, 11886.
337. Zhang, X.-Q.; Cheng, X.-B.; Chen, X.; Yan, C.; Zhang, Q., Fluoroethylene Carbonate Additives to Render Uniform Li Deposits in Lithium Metal Batteries. *Adv. Funct. Mater.* **2017,** *27* (10), 1605989.
338. Schneider, S. H.; Boxer, S. G., Vibrational Stark Effects of Carbonyl Probes Applied to Reinterpret IR and Raman Data for Enzyme Inhibitors in Terms of Electric Fields at the Active Site. *The J. Phys. Chem. B* **2016,** *120* (36), 9672-9684.
339. Atkins, P. W.; Friedman, R. S., *Molecular Quantum Mechanics*. 3 ed.; Oxford University Press: New York, 1997; p 533.
340. Andrews, S., Boxer, S. G., Vibrational Stark Effects of Nitriles I. Methods and Experimental Results. *J. Phys. Chem. A* **2000**, *104* (51), 11853-11863
341. Fried, S. D.; Wang, L.-P.; Boxer, S. G.; Ren, P.; Pande, V. S., Calculations of the Electric Fields in Liquid Solutions. *The J. Phys. Chem. B* **2013,** *117* (50), 16236-16248.
342. Urban, A.; Seo, D.-H.; Ceder, G., Computational understanding of Li-ion batteries. *NPJ Comp. Materials* **2016,** *2*, 16002.
343. Zhan, C.; Lian, C.; Zhang, Y.; Thompson, M. W.; Xie, Y.; Wu, J.; Kent, P. R. C.; Cummings, P. T.; Jiang, D.-e.; Wesolowski, D. J., Computational Insights into Materials and Interfaces for Capacitive Energy Storage. *Advanced Science* **2017,** *4* (7), 1700059.
344. Linstrom, P. J.; Mallard, W. G., NIST Chemistry WebBook. NIST Standard Reference Database: National Institute of Standards and Technology, Vol. 69.
345. Fortunato, B.; Mirone, P.; Fini, G., Infrared and Raman spectra and vibrational assignment of ethylene carbonate. *Spectrochimica Acta Part A: Molecular Spectroscopy* **1971,** *27* (9), 1917-1927.
346. Pethrick, R. A.; Wilson, A. D., Infrared and Raman spectroscopic studies of cyclic carbonates. *Spectrochimica Acta Part A: Molecular Spectroscopy* **1974,** *30* (5), 1073-1080.

347. Fried, S. D.; Bagchi, S.; Boxer, S. G., Measuring Electrostatic Fields in Both Hydrogen-Bonding and Non-Hydrogen-Bonding Environments Using Carbonyl Vibrational Probes. *J. Am. Chem. Soc.* **2013,** *135* (30), 11181-11192.
348. Deb, P.; Haldar, T.; Kashid, S. M.; Banerjee, S.; Chakrabarty, S.; Bagchi, S., Correlating Nitrile IR Frequencies to Local Electrostatics Quantifies Noncovalent Interactions of Peptides and Proteins. *The J. Phys. Chem. B* **2016,** *120* (17), 4034-4046.
349. Nyquist, R. A.; Settineri, S. E., Infrared Study of Ethylene Carbonate in Various Solvents and Solvent Systems. *Appl. Spectrosc.* **1991,** *45* (7), 1075-1084.
350. Langseth, A.; Lord, R. C., The Fine Structure of the Totally Symmetrical Raman Lines in Benzene and Benzene-d6. *The J. Chem. Phys.* **1938,** *6* (4), 203-204.
351. Bertran, J. F.; Ballester, L.; Dobrihalova, L.; Sánchez, N.; Arrieta, R., Study of Fermi resonance by the method of solvent variation. *Spectrochimica Acta Part A: Molecular Spectroscopy* **1968,** *24* (11), 1765-1776.
352. Brooksby, P. A.; Fawcett, W. R., The mid-infrared (attenuated total reflection) spectroscopy of ethylene carbonate in water. *Spectrochimica Acta Part A: Molecular and Biomolecular Spectroscopy* **2001,** *57* (6), 1207-1221.
353. Hausbrand, R.; Fingerle, M.; Späth, T.; Guhl, C., Energy level offsets and space charge layer formation at electrode-electrolyte interfaces: X-ray photoelectron spectroscopy analysis of Li-ion model electrodes. *Thin Solid Films* **2017,** *643*, 43-52.
354. Späth, T.; Becker, D.; Schulz, N.; Hausbrand, R.; Jaegermann, W., Understanding the SEI Formation at Pristine Li-Ion Cathodes: Chemisorption and Reaction of DEC on $LiCoO_2$ Surfaces Studied by a Combined SXPS/HREELS Approach. *Adv. Mater. Interfaces* **2017,** *4* (23), 1700567.
355. Kar, B. P.; Ramanathan, N.; Sundararajan, K.; Viswanathan, K. S., Matrix isolation and DFT study of the conformations of diethylcarbonate. *J. Mol. Struct.* **2014,** *1072*, 61-68.
356. Becker, D.; Cherkashinin, G.; Hausbrand, R.; Jaegermann, W., Adsorption of Diethyl Carbonate on $LiCoO_2$ Thin Films: Formation of the Electrochemical Interface. *The J. Phys. Chem. C* **2014,** *118* (2), 962-967.
357. Smith, G. D.; Borodin, O.; Russo, S. P.; Rees, R. J.; Hollenkamp, A. F., A molecular dynamics simulation study of $LiFePO_4$/electrolyte interfaces: structure and Li^+ transport in carbonate and ionic liquid electrolytes. *PCCP* **2009,** *11* (42), 9884-9897.
358. Becker, D.; Cherkashinin, G.; Hausbrand, R.; Jaegermann, W., XPS study of diethyl carbonate adsorption on $LiCoO_2$ thin films. *Solid State Ionics* **2013,** *230*, 83-85.
359. Labrenz, D.; Schröer, W., Conformational analysis of symmetric carbonic acid esters by quantum chemical calculations and dielectric measurements. *J. Mol. Struct.* **1991,** *249* (2), 327-341.
360. Wohlfarth, C., Static dielectric constant of diethyl carbonate. In *Static Dielectric Constants of Pure Liquids and Binary Liquid Mixtures: Supplement to Volume IV/17*, Wohlfarth, C.; Lechner, M. D., Eds. Springer Berlin Heidelberg: Berlin, Heidelberg, 2015; pp 96-96.
361. Das, A. K.; Rajasekhar, B. N.; Krishnakumar, S., Spectroscopy of diethyl carbonate, a green solvent: An experimental and theoretical study. *J. Quant. Spectrosc. Radiat. Transfer* **2018,** *217*, 53-62.
362. Wang, J.; Wu, Y.; Xuan, X.; Wang, H., Ion–molecule interactions in solutions of lithium perchlorate in propylene carbonate+diethyl carbonate mixtures: an IR and molecular orbital study. *Spectrochimica Acta Part A: Molecular and Biomolecular Spectroscopy* **2002,** *58* (10), 2097-2104.
363. Patrow, J. G.; Wang, Y.; Dawlaty, J. M., Interfacial Lewis Acid-Base Adduct Formation Probed by Vibrational Spectroscopy. *The J. Phys. Chem. Lett.* **2018**.
364. Wang, H. F.; Velarde, L.; Gan, W.; Fu, L., Quantitative sum-frequency generation vibrational spectroscopy of molecular surfaces and interfaces: lineshape, polarization, and orientation. *Annu. Rev. Phys. Chem.* **2015,** *66*, 189-216.

365. Bozorgchenani, M.; Buchner, F.; Forster-Tonigold, K.; Kim, J.; Groß, A.; Behm, R. J., Adsorption of Ultrathin Ethylene Carbonate Films on Pristine and Lithiated Graphite and Their Interaction with Li. *Langmuir* **2018**.
366. Vatamanu, J.; Borodin, O.; Smith, G. D., Molecular Dynamics Simulation Studies of the Structure of a Mixed Carbonate/$LiPF_6$ Electrolyte near Graphite Surface as a Function of Electrode Potential. *The J. Phys. Chem. C* **2012,** *116* (1), 1114-1121.
367. Takamatsu, D.; Koyama, Y.; Orikasa, Y.; Mori, S.; Nakatsutsumi, T.; Hirano, T.; Tanida, H.; Arai, H.; Uchimoto, Y.; Ogumi, Z., First In Situ Observation of the $LiCoO_2$ Electrode/Electrolyte Interface by Total-Reflection X-ray Absorption Spectroscopy. *Angew. Chem. Int. Ed.* **2012,** *51* (46), 11597-11601.
368. Ohno, P. E.; Wang, H.-f.; Geiger, F. M., Second-order spectral lineshapes from charged interfaces. *Nat. Commun.* **2017,** *8* (1), 1032.
369. Olson, J. Z.; Johansson, P. K.; Castner, D. G.; Schlenker, C. W., Operando SFG Detection of Electrolyte Redox Products at active Si Nanoparticle Li-ion Battery Interfaces. *Chem. Mater.* **2018**.
370. Boschloo, G.; Fitzmaurice, D., Electron Accumulation in Nanostructured TiO_2 (Anatase) Electrodes. *The J. Phys. Chem. B* **1999,** *103* (37), 7860-7868.
371. Aurbach, D., Review of selected electrode–solution interactions which determine the performance of Li and Li ion batteries. *J. Power Sources* **2000,** *89* (2), 206-218.
372. Vogel, Y. B.; Zhang, L.; Darwish, N.; Gonçales, V. R.; Le Brun, A.; Gooding, J. J.; Molina, A.; Wallace, G. G.; Coote, M. L.; Gonzalez, J.; Ciampi, S., Reproducible flaws unveil electrostatic aspects of semiconductor electrochemistry. *Nat. Commun.* **2017,** *8* (1), 2066.
373. Feng, Z. A.; Balaji Gopal, C.; Ye, X.; Guan, Z.; Jeong, B.; Crumlin, E.; Chueh, W. C., Origin of Overpotential-Dependent Surface Dipole at CeO_{2-x}/Gas Interface During Electrochemical Oxygen Insertion Reactions. *Chem. Mater.* **2016,** *28* (17), 6233-6242.

Appendix A

Experimental Methods

Silicon nanoparticles (50 nm, Alfa Aesar) were used for both device characterization and *operando* studies. For SFG measurements, the electrolyte solution consisted of 2M $LiClO_4$ (Alfa Aesar) dissolved in pure FEC (Aldrich, Solvay) and EC (BASF); these solutions were also tested in devices. Composite electrodes consisted of a 60:20:20 ratio of active material, conductive carbon (Targray), and polyacrylic acid binder (Aldrich). For *operando* studies, a CaF_2 prism (ISP Optics) was coated with a 6 nm layer of Ni, followed by 30 nm Si, both via electron-beam evaporation. Depth profiling by XPS confirmed that the working electrode surface contained no Ni within the XPS instrument resolution (Figure A1). Silicon nanoparticles were then deposited by spin-casting onto the Si/Ni-coated face of the prism at 1000 rpm from a suspension in isopropyl alcohol. The *operando* cell, assembled entirely inside of an argon-filled glove box (<0.1 ppm O_2 & H_2O), consisted of a Kel-F sample holder with a 316-stainless-steel screw bored through the bottom. Li metal was pressed onto the screw head to serve as the counter/reference electrode. The electrolyte was housed in a 200 μm-deep well. The periphery of the reservoir contained a butyl rubber gasket to maintain an airtight seal. The Si np/Ni-coated CaF_2 prism was pressed and secured into the pre-cut well after pipetting the electrolyte into it. A strip of nichrome ribbon was placed on the edge of the well before securing the prism. Pressure from an overhead cap was maintained with a set of four screws (see schematic in Figure 1 for the fully assembled cell) to ensure an airtight seal from the ambient environment. Voltammetric measurements were performed with an Autolab PGSTAT 302N at a scan rate of 3mV/s from the open circuit potential (OCP) using lithium metal as a counter/reference electrode. To obtain voltage-dependent compositional information of the SEI, voltammetric experiments were repeated with potentiostatic scanning at 3mV/s from OCP to potentials of 1.2 and 0.5 V, then held for 20 minutes; the final scan to 10mV was held for 10 minutes. This protocol will be referred to as 'potential scan/hold' throughout the results and discussion section. After each potential scan/hold, the voltage was swept back to OCP. Devices were cycled using a MACCOR 4000 galvanostat at a rate of C/20 for SEI formation, followed by C/10. All potentials are referenced to the Li/Li^+ redox couple.

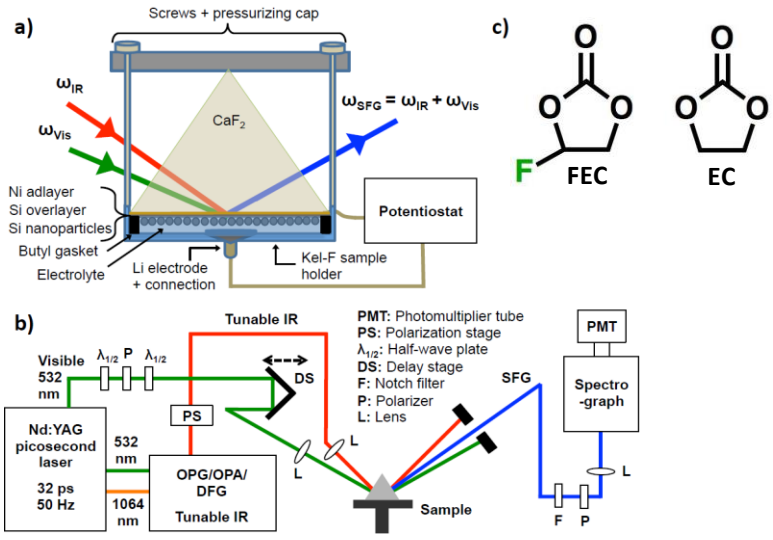

Figure A.1. a) Cross-sectional depiction of in-situ spectroelectrochemical sum frequency generation (SFG) cell, b) SFG spectral acquisition setup. c) Molecular structures of fluoroethylene carbonate (FEC) and ethylene carbonate (EC).

The SFG spectrometer was based on an EKSPLA picosecond system. The 532 nm visible beam was generated by frequency doubling of a short-pulsed Nd:YAG laser (32 ps pulse width and 50 Hz repetition rate), which also functioned as the pump for an OPG/OPA/DFG system that generated a tunable IR beam. With incidence angles of 62° (visible) and 60° (IR) relative the surface normal, the beams were overlapped with a spot size of ~1 mm^2 on the sample, where the energies per pulse were 20 μJ for the visible and 40-80 μJ for the IR (depending on the wavenumber). All the SFG spectra were recorded in the *ppp* polarization combination (SFG, visible, and IR all *p*-polarized), using a spectrograph with a photomultiplier tube detector collecting 700-900 acquisitions per step with an IR step size of 2 cm^{-1}. We overcame the issue of IR beam attenuation and sample degradation by analyzing the electrode interface in internal reflection mode (Figure 2), using defocused IR and Visible laser pulses with lower pulse power densities to minimize sample degradation.

In our spectral analyses of the SFG results, we used the relations below to fit the data:[122]

$$I_{SFG} = \left|\chi^{(2)} \cdot E_{\omega Vis} \cdot E_{\omega IR}\right|^2 \qquad \text{Eq. A.1.1}$$

where $E_{\omega_{Vis}}$ and $E_{\omega_{IR}}$ are the visible and IR electric fields, and $\chi^{(2)}$is the second-order susceptibility for SFG of the material, which can be described by

$$\chi^{(2)} = \chi_{NR}^{(2)} + \sum_k \frac{A_k}{\omega_k - \omega_{IR} - i\Gamma_k} \qquad \text{Eq. A.1.2}$$

where $\chi_{NR}^{(2)}$ is a nonresonant contribution, and ω_{IR} is the IR wavenumber. A_k is the amplitude for the k_{th} resonant mode, while the corresponding peak wavenumber and half width are given by ω_k and Γ_k,

respectively. The ability to obtain vibrational SFG depends on both the molecular hyperpolarizability of the probed species and the overall sample symmetry. For a vibration to be both IR and Raman active (thus having a nonzero hyperpolarizability), it is required that the individual molecule is non-centrosymmetric. Expanding this concept to an ensemble of molecules (for example, those molecules within an SEI), it is furthermore necessary that those molecules exhibit a non-centrosymmetric, non-isotropic arrangement in the sample. Key to understanding this selection rule is the fact that the SFG process is even-ordered and coherent; a more thorough description of these principles is summarized elsewhere.[122] For isotropic samples with a random orientation of molecules, the phase-relations between the SFG fields from the probed vibrations will thus be such that they cancel each other out. Therefore, the probed molecule needs to be ordered (i.e. have a preferred orientation and not be isotropically arranged) to be detectable with SFG. This is a ubiquitous requirement for SFG, regardless of whether the centrosymmetry is broken by an interface or not. This is also the origin for the surface sensitivity of SFG, as molecules in the bulk of a liquid normally are isotropically arranged, while surface interactions at interfaces often lead to a preferential molecular orientation. For conclusions based on the relative signal strengths and spectral features in various polarization combinations, it is essential to include the nanoparticle geometry in the analysis.[374-376] This is not crucial in our case, since we look at the evolution of specific peaks in a single polarization combination (*ppp*) and the spectral analysis can thus be performed as for flat interfaces.[376]

XPS analysis was performed using a Kratos Axis Ultra DLD photoelectron spectrometer, with a take-off angle (defined as the angle between the surface normal of the sample and the axis of the analyzer lens) of 0° and a monochromatized AlKα X-ray source operated at 15 mA and 15 kV. Spectra were acquired without charge neutralization. The lens mode was set to hybrid and the aperture to slot for all spectra. The surface composition was measured by survey spectra (1.0 eV step size) supplemented with detailed spectra for lower intensity peaks (0.3 eV step size), with an analyzer pass energy of 80 eV. For high resolution spectra (0.1 eV step size) the spectrometer pass energy was 20 eV. Data analysis was performed using CasaXPS software version 2.3.15. For depth profiling, the ion beam dose is 0.125 μA for 200 seconds over a 3x3 millimeter area. The sputter rate was calibrated from a known thickness of anodized tantalum oxide (60 nm).

The sample for XPS analysis of the SEI consisted of the same interface used in SFG measurements, with the substitution of a glass slide for the CaF_2 prism as the electrode substrate. The electrode was subjected to the same series of potential scan/hold measurements in a beaker containing the 2M $LiClO_4$ solution and a lithium ribbon counter electrode inside of an argon-filled glove box. After completion of the electrochemistry, the electrode was rinsed with diethyl carbonate, removed from the glove box, then immediately placed into the Kratos Axis antechamber.

Supplementary Information

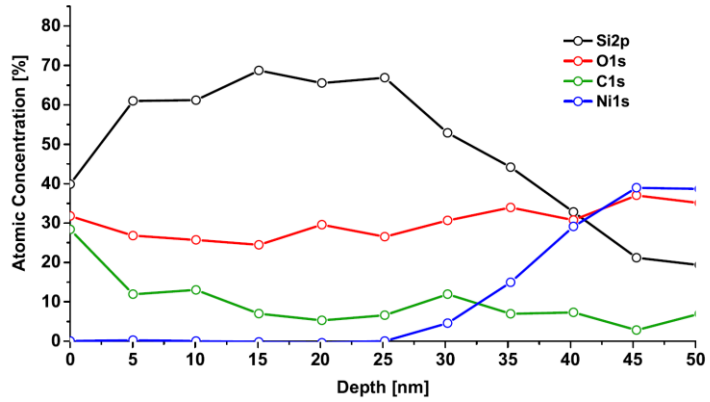

A.2: X-ray photoelectron spectroscopy depth profile of evaporated Si overlayer with Ni underlayer (substrate: glass). Details on the sample preparation and data acquisition are provided in the *Materials and Methods* section of the manuscript. The sputter time was converted to depth using a sputter rate determined from a 60 nm thick film of anodized tantalum oxide.

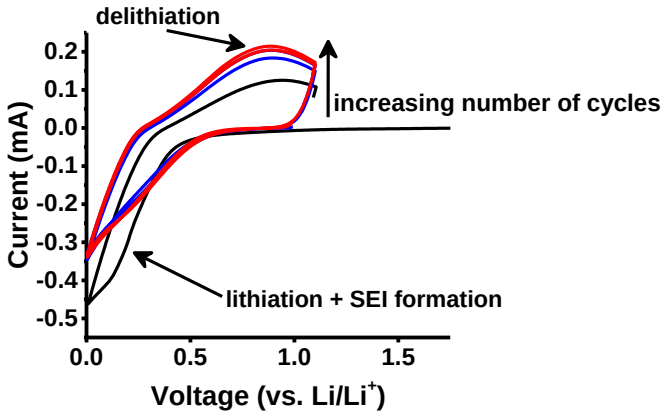

A.3: Voltammagram of EC + 2M $LiClO_4$ at 3mV/s

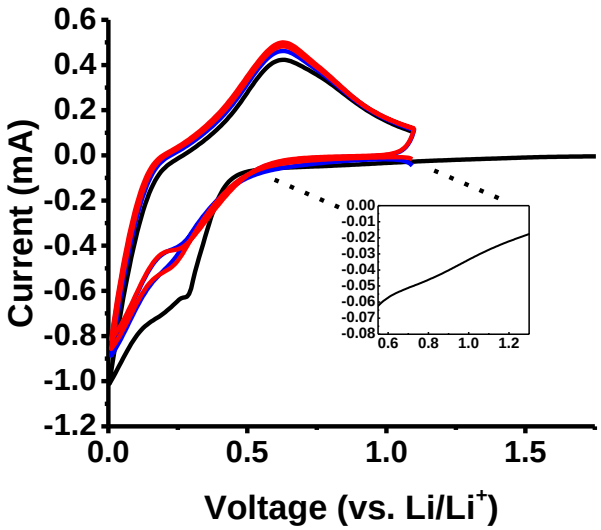

A.4: Voltammagram of FEC + 2M $LiClO_4$ at 3mV/s. The inset indicates greater Faradaic activity beginning at 1.2V than in the case of EC

References

122. Vidal, F.; Tadjeddine, A., Sum-frequency generation spectroscopy of interfaces. *Rep. Prog. Phys.* **2005,** *68* (5), 1095-1127.

374. Roke, S.; Kleyn, A. W.; Bonn, M., Femtosecond sum frequency generation at the metal–liquid interface. *Surf. Sci.* **2005,** *593* (1-3), 79-88.

375. Roke, S.; Roeterdink, W. G.; Wijnhoven, J. E. G. J.; Petukhov, A. V.; Kleyn, A. W.; Bonn, M., Vibrational Sum Frequency Scattering from a Submicron Suspension. *Phys. Rev. Lett.* **2003,** *91* (25), 258302.

376. Bratlie, K. M.; Komvopoulos, K.; Somorjai, G. A., Sum Frequency Generation Vibrational Spectroscopy of Pyridine Hydrogenation on Platinum Nanoparticles. *The J. Phys. Chem. C* **2008,** *112* (31), 11865-11868.

Appendix B

Experimental Details

Materials. All materials were used as received without further purification. 1-dodecanethiol (≥98%), fluoroethylene carbonate (99%), hydrogen tetrachloroaurate (III) trihydrate (≥99.99% trace metals basis), lithium metal ribbon (99.9% trace metals basis, 0.75-mm thickness), lithium hexafluorophosphate (99%), *N*-methyl-2-pyrrolidone (anhydrous, 99.5%), 1-octene (98%), poly(acrylic acid) (average M_W: 1800), sodium borohydride (99.99%), toluene (anhydrous, 99.8%), and vinylene carbonate (≤ 2% BHT as stabilizer, 97%) were purchased from Sigma Aldrich. Chloroform (HPLC grade, 99.9%), toluene (Certified ACS, 99.8%), and Whatman glass fiber separators (19-mm diameter discs, grade gf/f) were purchased from Fisher. Diphenylgermane (>95%) was purchased from Gelest. Ethanol (200 proof) was purchased from Decon Laboratories. Copper foil (9-μm thickness) and poly(vinylidene difluoride) (≥99.5%, average M_W: 600,000) were purchased from MTI. Conductive carbon (Vulcan® XC72R) was obtained from Cabot corporation. Lithium perchlorate (anhydrous, ≥99%) was purchased from Alfa Aesar. Diethyl carbonate (≥99%) and ethylene carbonate (99%) were purchased from BASF. CR2032 type coin cell components were purchased from Pred Materials International.

Germanium Nanowire Synthesis and Passivation. Dodecanethiol-passivated gold (Au) nanocrystals were prepared in a mixture of deionized water and toluene via the Brust method.[377] Germanium nanowires were synthesized via SFLS-based growth, and surface functionalized *in situ* via thermally initiated hydrogermylation with 1-octene.[293] In a typical reaction, a cylindrical 10-mL titanium reaction vessel was transferred into a nitrogen atmosphere glovebox, sealed, and placed in a heating block at 380°C. Keeping the exit valve closed, the reactor was pressurized to 900 psig using anhydrous toluene. A precursor mixture containing 1.7×10^{-2} mg/mL Au nanocrystals and 3.3×10^{-2} M diphenylgermane was prepared in anhydrous toluene (385:1 Au:Ge molar ratio). The mixture was loaded into a sealed stainless-steel piston and subsequently injected into the pre-pressurized and pre-heated reactor (900 psig, 380°C) at a rate of 0.5 mL/min for forty minutes. After nanowire growth, the temperature was then decreased to 220°C for surface hydrogermylation. Nanowire surface functionalization was carried out by injecting 12 mL of 2.1 M 1-octene in anhydrous toluene into the reactor at a rate of 0.5 mL/min for twenty minutes. The reactor temperature was then sealed and held at 220°C for 2 hours, followed by isochoric cooling to room temperature. Nanowires were collected with toluene. All germanium nanowires used in this study were hydrogermylated with 1-octene. Nanowires were washed three times in glass vials with a 2:2:1 ratio of toluene:chloroform:ethanol, and centrifuged at 2355 RCF for ten minutes. The resulting high-aspect-ratio,

single-crystalline germanium nanowires produced via this method have diameters ranging from 10 to 100 nm and lengths ranging from micrometers to millimeters.

Materials Characterization. Transmission electron microscopy (TEM) images were acquired with a FEI Technai G2 F20 Supertwin TEM, operating at 200 kV. Digital Micrograph software was used to generate Fast Fourier Transforms (FFTs) of high-resolution TEM images. Galvanostatic measurements were performed with a MACCOR 4200 galvanostat programmed to cycle between 0.01 and 1 V vs. Li/Li^+. The reported specific capacities are based on mass loading of active material, reported rates are based on the theoretical capacity of germanium (1384 $mA \cdot h \cdot g^{-1}$), and the reported capacity retention is relative to the second cycle. All electrodes were tested in duplicate.

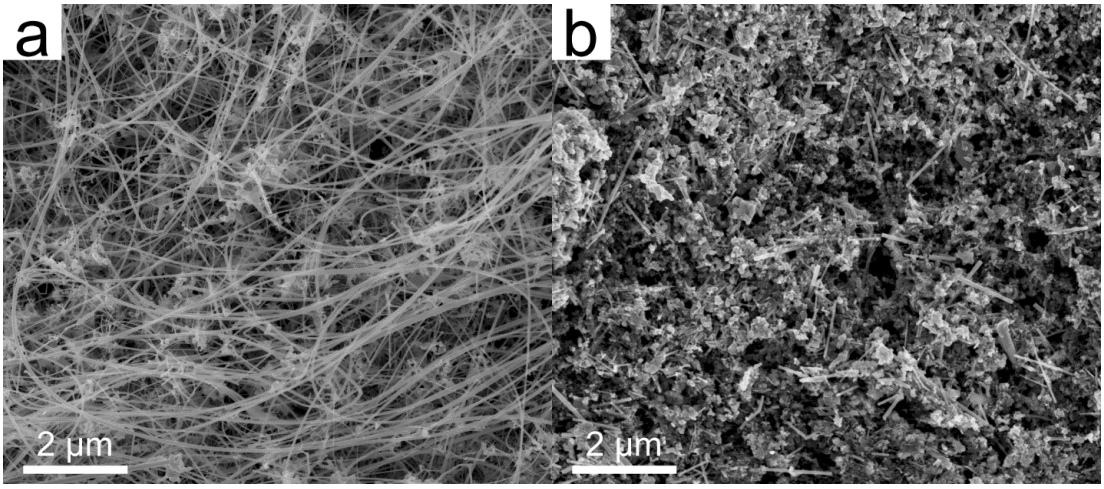

Figure B.1. SEM images of (a) 1-octene hydrogermylated Ge nanowires before incorporation into a composite electrode and (b) a composite electrode (70:10:20 mass ratio of Ge NWs:conductive carbon:PAA) fabricated via manual mixing with a mortar and pestle.

Germanium Nanowire Electrode Preparation and Coin Cell Assembly. Germanium nanowire synthesis and surface functionalization is included in the Supporting Information. Germanium nanowire electrodes were prepared through two different methods (manual mixing with a mortar and pestle or magnetic stirring in a glass vial), but all composite electrodes were fabricated with a mass ratio of 70% germanium nanowires, 10% conductive carbon, and 20% polymeric binder – either poly(acrylic acid) (PAA) or poly(vinylidene difluoride) (PVDF). In a typical "manual mixing" electrode preparation, 50 mg of germanium nanowires and 7 mg of conductive carbon additive were combined with 1.5 mL of 9.5 mg/mL polymeric binder (PVDF or PAA) in *N*-methyl-2-pyrrolidone (NMP) and mixed for ten minutes with a mortar and pestle (manual mixing). The wet slurry was then deposited onto a copper substrate and doctor bladed (25.4-µm thickness).

The wet composite electrode on the copper current collector was then placed on a hot plate preheated to 80°C to evaporate the NMP solvent. Figure B1 compares the nanowires before and after integration into a composite matrix via manual mixing.

In a typical "magnetic stirring" electrode preparation, germanium nanowires, conductive carbon, and polymeric binder (PVDF or PAA) were combined with 1.5 mL of NMP in a 3 mL scintillation vial and magnetically stirred at 1900 RPM for at least 16 hours. A glass Pasteur pipette was used to transfer the slurry to the copper current collector, which was then doctor bladed to a 25.4-µm thickness and placed onto a hot plate at 80°C until the solvent evaporated.

A 15-mm diameter C.S. Osborne hole punch was used to punch out electrodes, which were then dried overnight in a vacuum oven at 100°C that was held at a pressure below 50 mbar. Electrodes were weighed and transferred into an argon-filled MBraun glove box for further assembly into coin cells. Briefly, the electrode on the current collector, the glass fiber separator, and the plastic spacer were placed in the stainless-steel cup, consecutively. Then 100 µL of the electrolyte solution [1 M $LiPF_6$ in 1:1 w/w EC:DEC (ethylene carbonate: diethyl carbonate), with or without 5% w/w additive (FEC and VC)] was added dropwise onto the glass fiber separator to saturate it. The lithium foil, stainless-steel spacer, stainless-steel spring, and stainless-steel cap were then added to complete the half-cell assembly. A crimper (MTI Corporation) was used to seal the half-cell, whereupon it was transferred to a MACCOR testing unit for cycling.

Supplementary Information

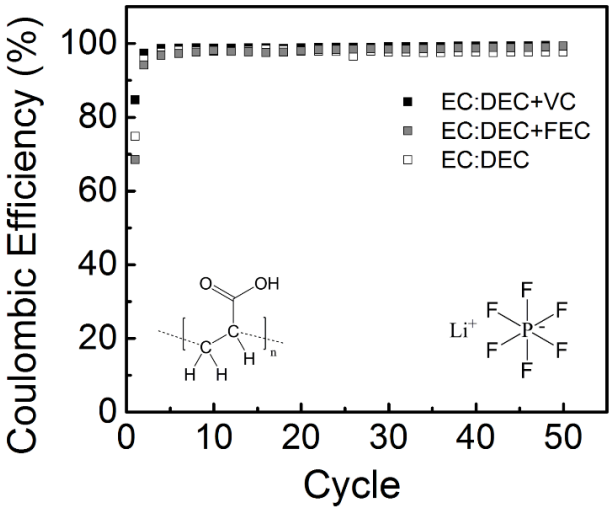

Figure B.2. Coulombic efficiencies of germanium nanowire composite electrodes fabricated via manual mixing, using PAA as a binder, and 1 M $LiPF_6$ in 1:1 w/w EC:DEC with different additives: white (no additive), gray (FEC), and black (VC), cycled at a rate of C/10.

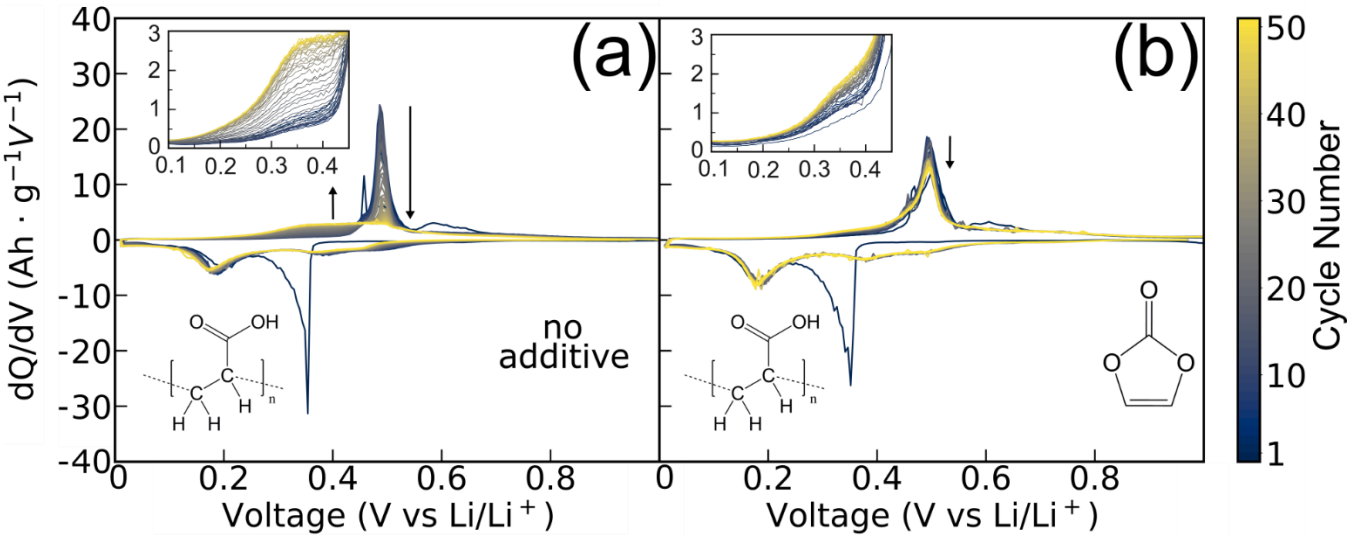

Figure B.3. Total differential capacity plots of 1-octene hydrogermylated germanium nanowire composite electrodes that employ PAA as a binder, and EC/DEC + 1M $LiClO_4$ as an electrolyte with (a) no electrolyte additive and (b) VC additive included. The color scale at the rightmost side delineates the evolution of the differential capacity profile over the first 50 cycles for each device.

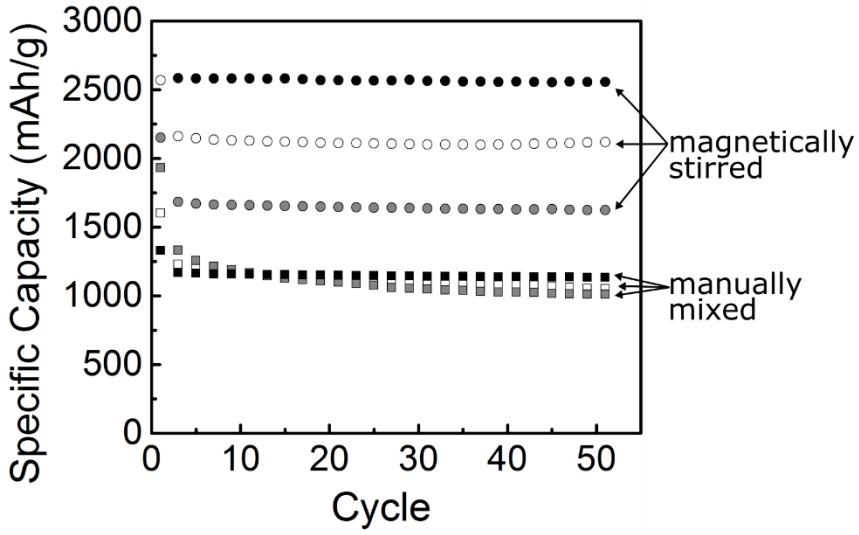

Figure B.4. Variations in the *apparent* specific capacity of electrodes doctor-bladed from manually mixed (squares) or magnetically mixed (circles) PAA slurries, due to spatial inhomogeneities in active material loading for devices punched from different regions of the copper foil. White, gray, and black symbols correspond to devices without additive, with FEC, and with VC, respectively.

Supplementary References

293. Holmberg, V. C.; Korgel, B. A., Corrosion Resistance of Thiol- and Alkene-Passivated Germanium Nanowires. *Chem. Mater.* **2010,** *22* (12), 3698-3703.

377. Brust, M.; Walker, M.; Bethell, D., Schiffrin, D.J., Whyman, R., Synthesis of thiol-derivatised gold nanoparticles in a two-phase Liquid–Liquid system. *J. Chem. Soc., Chem. Commun.* **1994**, 801-802.

Appendix C

Experimental details

The apparatus and methodology for VSS is described in detail elsewhere.[135] EC was obtained from BASF, deuterated ethylene carbonate (D_4-EC, 98% purity) from Cambridge Isotope Laboratories, FEC from Solvay, and DEC from BASF. For sample preparation, each electrolyte solvent was dissolved in 2-methyltetrahydrofuran (ACROS Organics) to a concentration of 100 mM. Each solution was pipetted between two Ni-coated (4.5 nm) CaF_2 windows (1 mm thickness, 12.7 mm diameter, FOCteck Photonics), with a spacer of approximately 27 μm between the electrodes. The capacitor path length was determined using interferometry. After the electrolyte solvents were pipetted between the electrode plates, the cell was immediately immersed in liquid nitrogen housed within the cryostat described previously.[135] Spectra were collected by averaging 64 scans each in the absence and presence of an externally applied field, and Stark tuning rates were determined from the contribution to the Stark spectrum of numerical fits of the zeroth, first, and second derivative contributions of the best-fit Voigt profile of the experimental absorbance spectrum.[131, 133, 340]

For solvatochromic analysis, 1 M solutions of the carbonates (excluding D_4-EC) were prepared in chloroform ($CHCl_3$, sigma), dichloromethane (DCM, Fisher Scientific), dimethylsulfoxide (DMSO, EMD), tetrahydrofuran (THF, sigma), 1,3-dioxolane, (DOL, Sigma), toluene (Tol, Alfa Aesar) and acetonitrile (ACN, sigma) and subsequently analyzed using ATR-FTIR spectroscopy. All spectra were collected on a Nicolet 8700 FTIR spectrometer using a liquid nitrogen-cooled MCT detector, averaged over 32 scans with 1 cm^{-1} resolution. The peak value and line shape for all C=O vibrations were determined with Voigt fits. Parameterization of electrolyte solvents molecules, MD equilibration and production, and determination of solvent electric fields from MD simulations were performed as previously described.[338] Fixed charge force field parameters for organic solvents were taken from Caleman *et al*.[378] (Table C2) summarizes the calculated solvent fields exerted onto the C=O.

Optical constants were obtained using an infrared variable angle ellipsometer housed in the Center for Integrated Nanotechnologies at Sandia National Laboratories. Spectra were collected at the CaF_2 prism/liquid interface under anhydrous conditions at room temperature with 4 cm^{-1} resolution in reflection mode at a fixed angle of 60°. Spectra were averaged over 100 scans. The refractive index *n* of the liquid was extracted by fitting experimental data (ellipsometric ψ and Δ angles) to a series of generalized causal oscillators using an iterative Marquardt-Levenberg algorithm. Values from these

measurements were then used for calculating interfacial field magnitudes using equations described in the discussion section.

Supplementary Information

Table C1. Average peak position of C=O modes for all carbonate solvents.

Carbonate Solute (Solvent)	Average Peak Position (cm^{-1})
DEC (THF)	1746.36
DEC (dibutyl ether)	1749.05
DEC (acetonitrile)	1744.64
DEC (chloroform)	1741.16
DEC (dichloromethane)	1743.01
DEC (diglyme)	1749.49
DEC (1,3-dioxolane)	1744.75
DEC (toluene)	1745.70
DEC (hexane)	1748.78
EC (THF)	1811.31
EC (chloroform)	1807.40
EC (dichloromethane)	1807.81
EC (toluene)	1812.78
EC (1,3-dioxolane)	1808.95
FEC (THF)	1838.61
FEC (chloroform)	1836.02
FEC (dichloromethane)	1834.64
FEC (dimethylsulfoxide)	1828.52
FEC (1,3-dioxolane)	1836.35

Table C2. Solvent field values used for field frequency calibration

	DEC		EC		FEC	
Solvent	Average	Std. Dev.	Average	Std. Dev.	Average	Std. Dev.
1,3-dioxolane	-9.97	10.44	-33.54	10.56	-32.28	10.51
acetonitrile	-10.64	10.99				
chloroform	-18.95	15.57	-36.32	13.02	-32.55	13.18
dibutyl ether	-1.67	5.24				
dichloromethane	-15.59	13.19	-35.84	16.17	-34.08	11.90
dimethylsulfoxide					-44.30	12.19
hexane	-0.08	0.74				
tetrahydrofuran	-5.50	7.30	-25.48	8.00	-26.16	8.01
toluene	-4.86	6.27	-19.83	7.14		
diglyme	-8.94	9.19				

As shown in Table 1, the Stark tuning rate of FEC is nearly twice as large as that of EC based on the slope of the field-frequency calibration (Figure 5b), though they differ by only a single atom distant from the carbonyl probe. Comparison of identical solvent calculations as shown in Table S2 indicates that the

average electric field for EC and FEC are nearly identical, consistent with the similarity in overall structure, but the experimental frequency shifts are nearly twice as large across the solvent span for FEC per (MV/cm) in Figure 5b. Whether this is due to discrepancies between the parameterization of the carbonate solvents in MD simulations (i.e. requiring higher level calculations to determine the atomic charges), or a suggestion that the overall bond displacement is more sensitive in the case of FEC, remains to be determined. As may be expected for a local high frequency mode such as a carbonyl, the C and O atom of EC and FEC exhibit nearly identical atomic charges consistent with their overall structures. The simple 1-dimensional model for describing the linear Stark effect and the Stark tuning rate as presented in reference 37 is $|\Delta\mu|=q*\Delta d$, where q is the bond's charge and Δd is the change in bond length between the vibration's first-excited state and ground state. In this model, either the overall charge of the bond or bond displacement will lead to a significant change in $|\Delta\mu|$. As previously mentioned, the overall charge at the O and C atoms of the C=O are nearly identical for EC and FEC at the level of theory used herein, suggesting that this difference then arises from the bond displacement. This could in principle be modeled using the anharmonic shift as determined from 2D-IR, though this is beyond the scope of this manuscript.

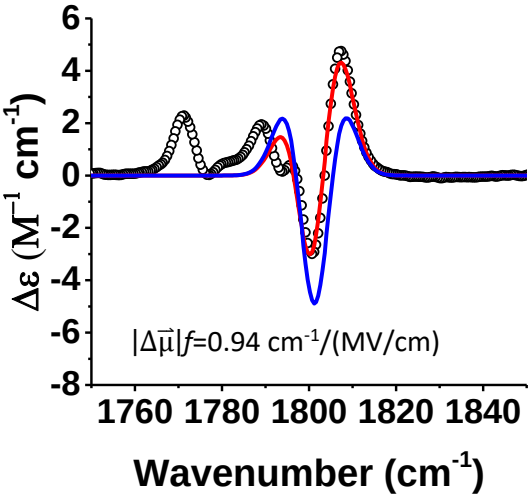

Figure C.1. Stark spectrum of EC in 2-MeTHF scaled to 1 MV/cm. Raw data is shown as black dots, The line of best fit (red trace) is qualitatively similar to the 2nd-derivative of the absorbance spectrum. The Stark tuning rate is listed in the bottom right in units of $cm^{-1}/(MV/cm)$.

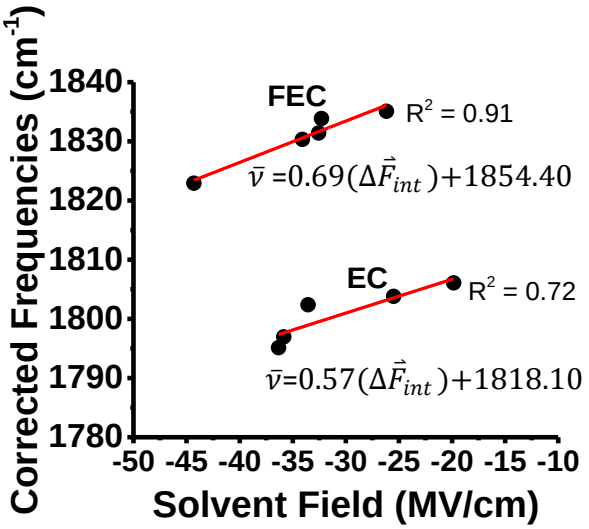

Figure C.2. Corrected C=O frequencies with use of a perturbation model.

Carbonate Solute (Solvent)	Average C=O peak position corrected for fermi resonance (cm^{-1})
EC (toluene)	1806.06
EC (chloroform)	1797.31
EC (dichloromethane)	1798.83
EC (dioxolane)	1802.37
EC (THF)	1803.35
FEC (dioxolane)	1833.85
FEC (chloroform)	1831.38
FEC (dichloromethane)	1830.33
FEC (dimethylsulfoxide)	1822.93
FEC (THF)	1835.06

Table C3. frequencies corresponding to corrected C=O modes, using a perturbation model referenced in sources[351-352, 379]

An example of the effect different solvents have on changes to both the position and amplitudes of the C=O stretch and F_R mode is plotted below. For clarity, only two spectra are plotted in Figure 2 for EC (1M EC dissolved in THF and ACN) ; spectral data for all solvents is recorded in table C3. Briefly described, the perturbation model has been used to extract an unperturbed C=O frequency (δ_0) through the coupling constant (W), calculated by the difference (δ) between the observed vibrational frequencies of the F_R (ν_+) and C=O (ν_-) modes and their intensity ratio (R). As an example of this concept, consider the following plot with intensity and absorption (I and $\nu_{+/-}$) variables labeled:

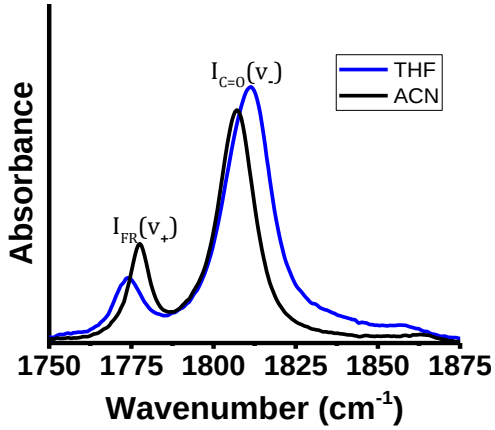

Figure C.3. The intensities of the carbonyl ($I_{C=O}$) and Fermi resonant (I_{FR}) modes, for EC change when solvated by acetonitrile and tetrahydrofuran (ACN and THF, respectively). The absorption values also shift.

$R = \frac{I_{C=O}}{I_{FR}}$

$\delta = \nu_+ - \nu_-$

$W = \frac{\delta}{R+1}\sqrt{R}$

$\delta_0 = [\delta^2 - 4W^2]^{1/2}$

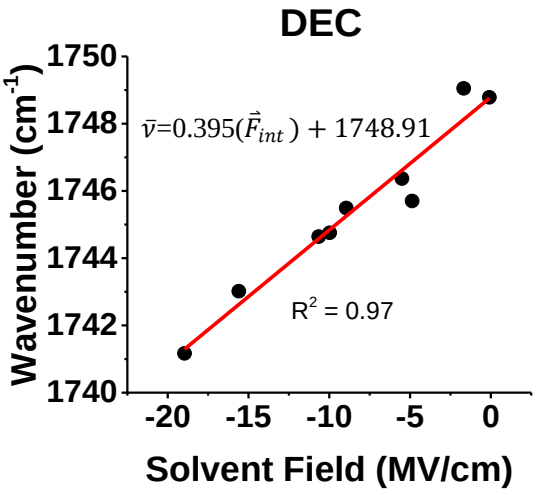

Figure C.4. Expanding the range of solvent fields for DEC, used as an example because it exhibits no F_R interference, changes its tuning rate by ~5% and exhibits a lower coefficient of determination (R^2).

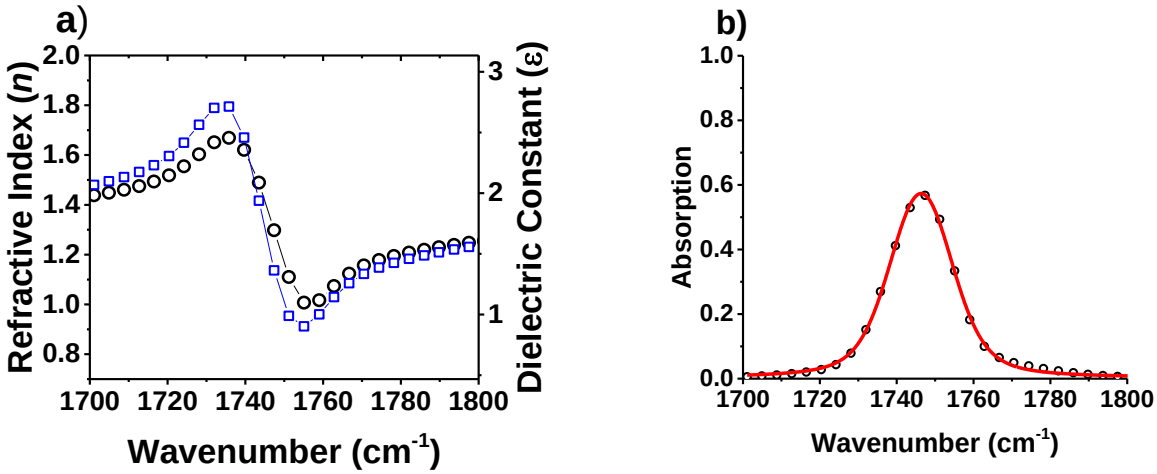

Figure C.5. (a) Infrared ellipsometry of DEC, exhibiting the refractive index (n, open circles) and dielectric constant (ε, open squares) as a function of wavenumber. (b) Absorption spectrum of DEC, from which optical constants were obtained.

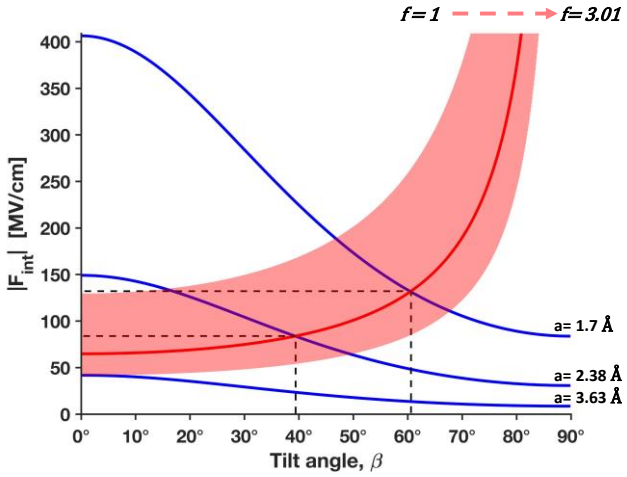

Figure C.6. The C=O mode of EC red shifts by 40 cm^{-1} (from 1868 cm^{-1} in the gas phase[345] to 1820 cm^{-1} on the surface of graphite[365]). Using optical constants of the electrolyte solvent ε = 89.6,[380] refractive index n = 1.419,[381] dipole moment μ = 4.81D[382] and C=O bond length of 1.15 Å,[383] the application of Eq. 1-3 resolves fields between 83.9-132.1 MV/cm between angles of 39.4-60.6°, respectively. The value representing the red line is when *f*=2.

Supplementary References

131. Boxer, S. G.; Bublitz, G. U., Stark spectroscopy: Applications in Chemistry, Biology, and Materials Science. *Annu. Rev. Phys. Chem.* **1997,** *48*, 213–242.

133. Andrews, S. S.; Boxer, S. G., Vibrational Stark Effects of Nitriles II. Physical Origins of Stark Effects from Experiment and Perturbation Models. *The J. Phys. Chem. A* **2002,** *106* (3), 469-477.

135. Andrews, S. S.; Boxer, S. G., A liquid nitrogen immersion cryostat for optical measurements. *Rev. Sci. Instrum.* **2000,** *71* (9), 3567.

338. Schneider, S. H.; Boxer, S. G., Vibrational Stark Effects of Carbonyl Probes Applied to Reinterpret IR and Raman Data for Enzyme Inhibitors in Terms of Electric Fields at the Active Site. *The J. Phys. Chem. B* **2016,** *120* (36), 9672-9684.
340. Andrews, S., Boxer, S. G., Vibrational Stark Effects of Nitriles I. Methods and Experimental Results. *J. Phys. Chem. A* **2000,** *104* (51), 11853-11863.
345. Fortunato, B.; Mirone, P.; Fini, G., Infrared and Raman spectra and vibrational assignment of ethylene carbonate. *Spectrochimica Acta Part A: Molecular Spectroscopy* **1971,** *27* (9), 1917-1927.
351. Bertran, J. F.; Ballester, L.; Dobrihalova, L.; Sánchez, N.; Arrieta, R., Study of Fermi resonance by the method of solvent variation. *Spectrochimica Acta Part A: Molecular Spectroscopy* **1968,** *24* (11), 1765-1776.
352. Brooksby, P. A.; Fawcett, W. R., The mid-infrared (attenuated total reflection) spectroscopy of ethylene carbonate in water. *Spectrochimica Acta Part A: Molecular and Biomolecular Spectroscopy* **2001,** *57* (6), 1207-1221.
365. Bozorgchenani, M.; Buchner, F.; Forster-Tonigold, K.; Kim, J.; Groß, A.; Behm, R. J., Adsorption of Ultrathin Ethylene Carbonate Films on Pristine and Lithiated Graphite and Their Interaction with Li. *Langmuir* **2018,** *34* (29), 8451-8463
378. Caleman, C.; van Maaren, P. J.; Hong, M.; Hub, J. S.; Costa, L. T.; van der Spoel, D., Force Field Benchmark of Organic Liquids: Density, Enthalpy of Vaporization, Heat Capacities, Surface Tension, Isothermal Compressibility, Volumetric Expansion Coefficient, and Dielectric Constant. *Journal of Chemical Theory and Computation* **2012,** *8* (1), 61-74.
379. Lee, Y.-T., Hydrogen bond effect on the Raman spectrum of liquid ethylene carbonate. *Journal of Raman Spectroscopy* **1997,** *28* (11), 833-838.
380. Johnson, P. H. *Properties of ethylene carbonate and its use in electrochemical applications: a literature review*; Lawrence Berkeley Lab., CA (USA): 1985.
381. Chernyak, Y., Dielectric Constant, Dipole Moment, and Solubility Parameters of Some Cyclic Acid Esters. *Journal of Chemical & Engineering Data* **2006,** *51* (2), 416-418.
382. Kempa, R.; Lee, W. H., 392. The dipole moments of some cyclic carbonates. *Journal of the Chemical Society (Resumed)* **1958,** (0), 1936-1938.
383. Shakourian-Fard, M.; Kamath, G.; Sankaranarayanan, S. K. R. S., Evaluating the Free Energies of Solvation and Electronic Structures of Lithium-Ion Battery Electrolytes. *ChemPhysChem* **2016,** *17* (18), 2916-2930.